Bronkhorst®
HIGH-TECH

UNIVERSITY OF TWENTE.
**Faculty of Engineering Technology,
Engineering Fluid Dynamics**

Characterisation of Low Flow Valves for Gases

R.H.J. Hebbink, s1485490
M.Sc. Internship
28-08-2017 to 22-12-2017

Preface

This report is written for my internship at Bronkhorst High-Tech B.V. in Ruurlo. The internship is part of the master programme Mechanical Engineering at the University of Twente and aims at teaching the student to function independently in a real life situation at graduate level. During four months I performed a study on the characterisation of low-flow valves. In this report the outcomes of the study are described, as well as how they were obtained.

During my internship, I was supervised by Jan van de Geest and Sander Klein Hesselink. I would like to thank them for their help.

Rutger Hebbink

Ruurlo, 22-12-2017

Summary

Bronkhorst High-Tech develops and assembles mass flow meters and controllers for low flows. In order to serve requests to control increasingly lower flows, the Piezo valve has been developed. However, it appeared that the valve capacity could not be characterized by the K_v-model as used for the common magnetic valves. Rather than the orifice diameter, as for the magnetic valves, the throughflow height is restrictive for the flow capacity of the Piezo valve. Various correction methods to the K_v-model were tested in earlier studies, but found to be inappropriate.

In this study, a new, theoretical, model to predict the gaseous mass flow through the Piezo valve was derived from the Navier-Stokes equations with a slip condition at the boundary. The geometry was simplified to an axisymmetric disk, the flow was assumed steady and isothermal and the gases were assumed to be ideal. By non-dimensionalising the equations, the less important terms were identified and neglected. The resulting equations could be solved algebraically. After that, flow choking was implemented in the model as a critical situation, and two fudge factors were implemented to allow empirical corrections for effects that were not taken into account.

The model was tested by conducting measurements on a test Piezo valve. It was found that a height-based correction and a gas-specific correction, that has to be determined in a calibration measurement, were required to correctly approximate the mass flow with the model. With these corrections, the model was capable of predicting the mass flow for valves with a shim height up to and including 25 μm to a relatively high accuracy in non-choking flows, and to an acceptable accuracy for more critical flows. Deviations between the model and the measurement data existed due to the influence of choking, especially in the transition zone. The flow through the valve with a shim height of 50 μm was found to be characterised by a different relation between pressure drop and mass flow, and hence the model was not valid for this height.

By introducing safety factors to the model, it was guaranteed that the desired flow can always be reached by a shim height that is selected with the model. This allows BHT to use the model in practice. The safety margin was relatively large for certain situations due to (the transition to) choked flow.

Further research is required to explain the empirically determined correction factors, to further validate the model and to expand the validity of the model to (and to optimise it on) choked flow and flows through valves with larger shim heights.

Contents

Nomenclature

Abbreviations and Definitions

BHT	Bronkhorst High-Tech.
Choked flow	Situation where the mass flow through the valve does not increase upon a decrease in outlet pressure. It is caused by reaching the speed of sound in a constriction.
Critical	Condition where the flow is choked.
NC	Normally Closed.
NO	Normally Open.
Normal conditions	Conditions at which the normal volumes and densities are calculated. Following the European standard, these are given by $T = 0\ ^\circ$C and $P = 1.013 \cdot 10^5$ Pa.
Orifice	Restrictive opening through which the fluid exits the valve.
Piezo valve	Microfluidic valve of BHT that uses Piezo elements to regulate the flow.
Reversed flow	Flow in the Piezo valve directed in the positive radial direction (outward).
Shim	Ring in the Piezo valve that creates distance between the orifice and the membrane.
Valve capacity	Maximum flow that can pass through the valve under certain operating conditions.

Symbols

C_1	Slip coefficient (in this study: $C_1 = 1$)	[-]
c	Speed of sound	$[\frac{\text{m}}{\text{s}}]$
d, d'	Orifice diameter	[m], [mm]
h	Shim height, also used as channel height	[m]
F_1	Fudge factor scaling the velocity	[-]
F_2	Fudge factor scaling the choking velocity	[-]
K_v	Normalised valve capacity, indicating the water flow at $\Delta P = 1$ bar	$[\frac{\text{m}^3}{\text{h}}]$
Kn	Knudsen number	[-]
L	Radius of the disk-shaped channel of the Piezo valve	[m]
$\dot{m}$	Mass flow	$[\frac{\text{kg}}{\text{s}}]$
Ma	Mach number	[-]
T	Temperature	[K]
P	Pressure	[Pa]
R	Specific gas constant	$[\frac{\text{J}}{\text{kg}\cdot\text{K}}]$
r	Radial coordinate	[m]
Re	Reynolds number	[-]
S_1	Constant safety factor ($= 0.9$)	[-]
S_2	Pressure dependent safety factor ($= \sqrt[4]{\frac{P_{in}-P_{out,c}}{P_{in}}}$)	[-]
u	Velocity	[m/s]
z	Lateral coordinate	[m]
γ	Ratio of specific heats, $\frac{c_P}{c_v}$	[-]
ε	Ratio of height and radius of the channel	[-]
λ	Mean free path	[m]
μ	Viscosity	[Pa·s]
ρ	Density	$[\frac{\text{kg}}{\text{m}^3}]$
ϕ_v	Liquid volume flow	$[\frac{\text{m}^3}{\text{h}}]$
ϕ_{vn}	Gas normal volume flow	$[\frac{\text{m}_\text{n}^3}{\text{h}}]$

Subscripts

c	Critical
i, in	Inlet
n	Normal conditions
o, out	Outlet

---

1 Introduction

Bronkhorst High-Tech B.V. (BHT) develops and assembles mass flow meters and controllers for low flows. They are offered for both gaseous and liquid flows for applications in laboratory, industrial and hazardous areas [1]. Two different principles for measuring the flow are used: the thermal principle (used in most meters) and the Coriolis principle (used in the CORI-FLOW meters). For the thermal principle, (a part of) the fluid is heated by two heating elements [2]. At both elements, the temperature is measured, giving a temperature difference which is directly proportional to the mass flow through the sensor [2]. The CORI-FLOW meters contains a tube that is part of an oscillating system [3]. When a fluid flows through the tubes, Coriolis forces cause a variable phase shift between the loops [3]. This phase shift is detected by sensors and is a measure for the mass flow [3]. One of the advantages of this principle, compared to the thermal principle, is that gaseous and liquid flows can be measured with the same sensor [3].

In order to control the flow, a magnetic valve is added to the sensor. In figure 1.1, it can clearly be seen that a controller is indeed a meter with a (magnetic) valve added to it. Two types of valves exist, directly and indirectly controlled valves, where the first type is faster and most commonly used [4]. These types can be subdivided into normally closed (NC) and normally open (NO) valves [4]. The BHT valves are electrically controllable [4]. For the NC valves, the valve opens at the openings voltage (higher than 0 V), until it is fully opened at a power that is some Volts higher (so lower than the maximum voltage) [4]. The difference between the two voltages is the control region. The NO valves work exactly the opposite way.
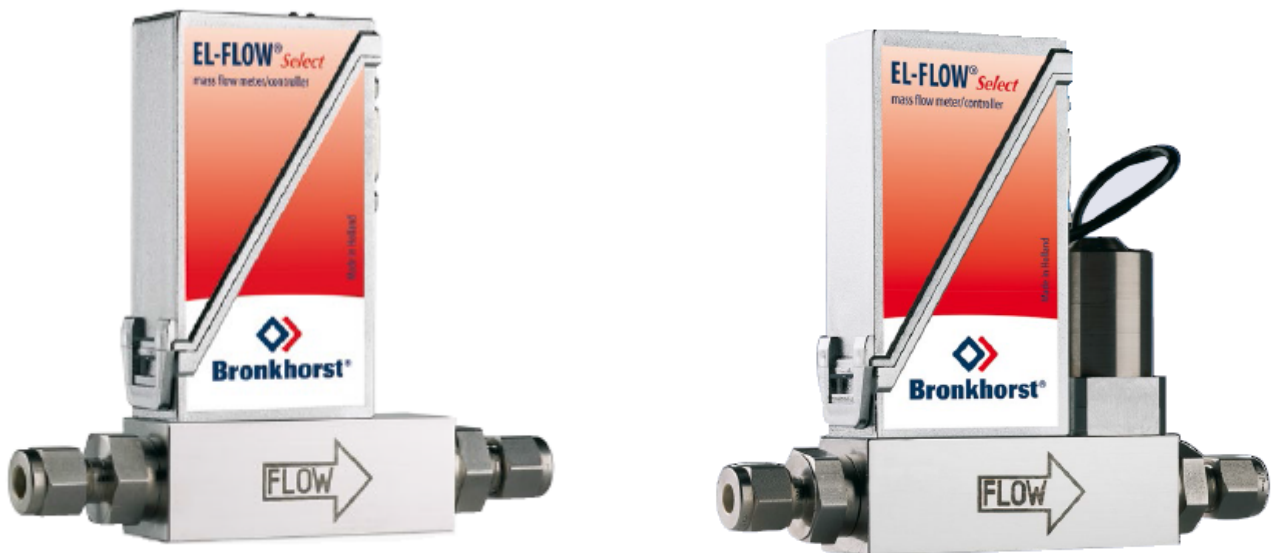
| (a) Mass flow Meter. | (b) Mass flow controller. |

Figure 1.1: Thermal mass flow meter (a) and controller (for gases)

The capacity of the valves is characterized with the K_v-value. This is a normalized value of the mass flow that can pass through the valve. A customer will ask BHT to regulate a medium at specified conditions, from which the desired K_v-value can be determined. This value is then used to determine the most important valve dimensions and select an appropriate valve. The valve's K_v-value will always be higher than the desired K_v-value, in order to ensure that the desired flow can be reached by the valve.

The tendency of recent years is that customers ask BHT to regulate increasingly lower flows. However, controlling mass flows in the order of 1 gr/h or less required a different valve design compared to the existing designs [5]. Therefore, the Piezo valve, named after the Piezo elements that are used to regulate the flow, was developed. It is capable of adequately regulating the desired low flows, such that a flow controller with small internal volume and fast control characteristics can be built [5].

It appeared, however, that the characterization with the K_v-values as they are commonly used within BHT does not provide sensible results [5–7]. Therefore, the goal of this study is to develop a model to determine the capacity of a microfluidic valve (like the Piezo valve) for given operating conditions. In an earlier study, a model

(although with limited validity) was developed for liquids [6]. Hence, this study will aim on developing a model for gases.

The structure of this report is as follows. First of all, the problem will be analysed in detail in order to correctly define the problem, and main and subquestions will be posed. Secondly, the K_v-value is analysed in more detail in order to study the reason that it does not work for the Piezo valve and to investigate the possibilities of additional corrections to the current K_v-calculations. Next, a theoretical model is derived for the (simplified) geometry of the Piezo valve. After that, the measurement method that is used to validate the model is described, followed by the empirical improvement of the model. Then the influence of reversing the flow direction is described, after which it is described how the model can be used (safely) in practice by BHT. Finally, the conclusions and the recommendations of the study are given.

2 Definition of the Problem

In order to correctly formulate the main question of this study, the problem is further analysed. First, the K_v-value will be introduced, and it is described how it is used. After that, the Piezo valve is introduced, and it is shown how the K_v-model does not provide the desired results when being applied to this valve. Lastly, the main and subquestions of this study are posed.

2.1 K_v-value

The capacity of the valve (the maximum flow that can pass through the valve) is one of the most important characteristics, as it determines in which processes it is applicable and in which not. Valves are often characterised by a K_v-value [8], which is a normalised value that indicates the flow capacity of the valve. It specifies the water flow in m^3/h through the valve at a pressure drop of 1 bar [9]. The value is used as follows. A customer will ask BHT to deliver a valve that is capable of regulating (or measuring) a certain flow. In order to serve this request, the following input is desired from the customer:

- Flow to be controlled or measured

- Medium that will be used

- Desired inlet pressure

- Desired outlet pressure

- Temperature of the medium

From these operating conditions, BHT selects the most appropriate valve. Here the K_v-value comes in use. For liquids, it is calculated by (2.1) [4]. In this equation, ϕ_v is the liquid volume flow in m^3/h, ρ is the density in kg/m^3 and ΔP is the pressure difference between inlet and outlet in bar. Corrections to this formula for liquids with high viscosity are available. For gases, the K_v-value is calculated using (2.2) [4]. Here, ϕ_{vn} is the volume flow at normal conditions in m$_n^3$/h, P_{in} and P_{out} are respectively the inlet and outlet pressure in bar, ΔP is the difference between these pressures (in bar), T is the temperature in K and ρ_n is the density at normal conditions in kg/m$_n^3$. These normal conditions are, following the European standard, given by a temperature of 0 °C and a pressure of 1.013 bar [10]. It should be noted that, due to the constant density at which the volume flow is determined, it is in fact a scaled mass flow and not the actual volume flow. The equation for gases is split in two regions: a subcritical ($\Delta P \leq 0.5P_{in}$) and a supercritical region. At $\Delta P = 0.5P_{in}$, the speed of sound is reached and the flow chokes [8]. After this, the mass flow is only increased by an increase in inlet pressure, and not by a decrease in outlet pressure, as can be seen in the equation.

$$K_{v,l} = \phi_v \sqrt{\frac{\rho}{\Delta P \cdot 1000}} \tag{2.1}$$

$$K_{v,g} = \begin{cases} \dfrac{\phi_{vn}}{514} \sqrt{\dfrac{\rho_n T}{\Delta P \cdot P_{out}}}, & \Delta P \leq 0.5P_{in} \\[3mm] \dfrac{\phi_{vn}}{257P_{in}} \sqrt{\rho_n T}, & \Delta P > 0.5P_{in} \end{cases} \tag{2.2}$$

From the required K_v-value, the required orifice diameter of the valve is calculated. The orifice is the hole through which the fluid exits the valve, and is the restriction to the flow. Within BHT, the required orifice diameter in mm is, for both gases and liquids, calculated from the K_v-value using (2.3) [4].

$$d' = 7.6\sqrt{K_v} \tag{2.3}$$

When testing the model, the opposite is being done: an orifice diameter is selected, such that the valve's K_v-value can be calculated from (2.3). For specified operating conditions and medium, the expected flow rate is then calculated from (2.1) or (2.2). This is compared to measurement data to validate the model. In figure 2.1, the calculated and measured flows are shown for a magnetic valve with an orifice diameter of 0.14 mm. It

---

is seen that the shapes of both graphs are similar, but the values are not. In figure 2.2, it is seen that replacing the factor 7.6 in (2.3) by 5.5 results in an almost exact model. The reason that a factor of 7.6 is used is to include an error margin in the determination of the orifice diameter from the K_v-value [7]. With this margin, it is guaranteed that the valve can always reach the maximum specified flow. In this way, the flow that is required by the customer can always be delivered with the selected valve.
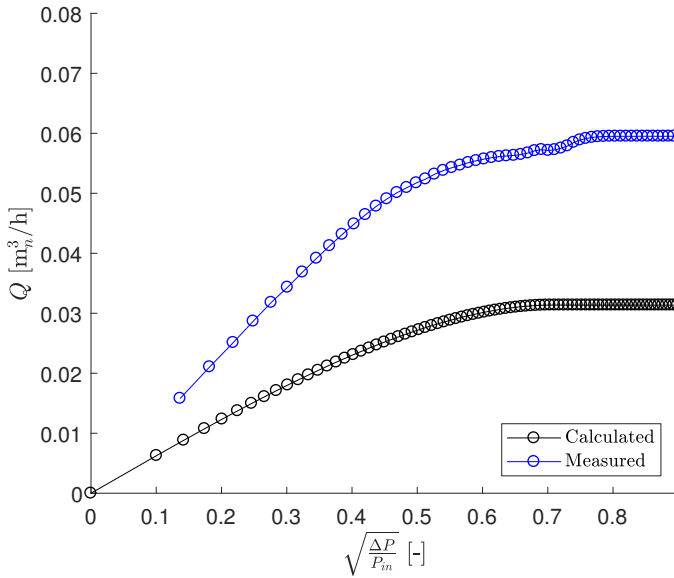
Figure 2.1: Calculated and measured air flow for a magnetic valve with an orifice diameter of 0.14 mm and inlet pressure $P_{in} = 7$ bar (measurement data from [7]).
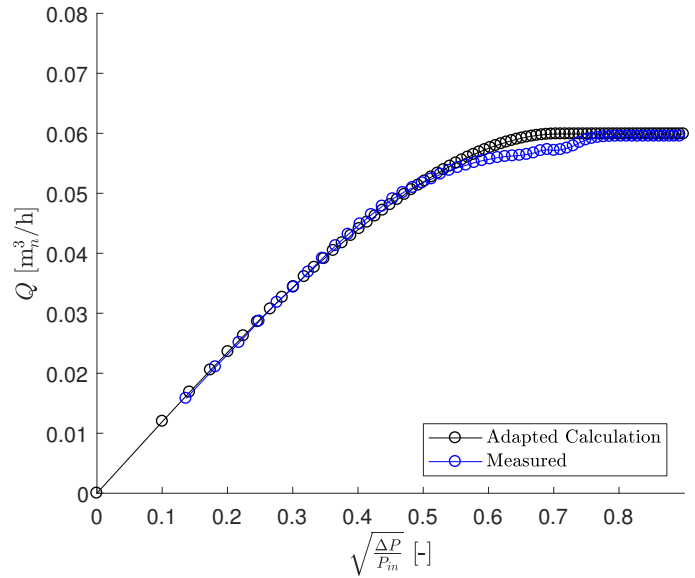
Figure 2.2: Adapted calculated air flow ($d' = 5.5\sqrt{K_v}$) and measured air flow for a magnetic valve with an orifice diameter of 0.14 mm and inlet pressure $P_{in} = 7$ bar (measurement data from [7]).

2.2   Piezo valve

In order to fulfill the customer's request for increasingly lower flows, a new type of valve has been developed: the Piezo valve. This valve is capable of adequately regulating mass flows in the order of 1 gr/h, allowing for a flow controller with a small internal volume and fast control characteristics [5]. The Piezo valve makes use of a Piezo stack actuator [5]. This actuator uses the inverse piezoelectric effect to regulate the flow. The piezoelectric effect is the effect of accumulating electric charge in certain solid materials when a mechanical stress is applied [11]. The inverse is true for these materials as well: they expand when an electric charge is applied. This principle is used for the actuator: the length is increased by applying an electric charge. Hence, the Piezo valve is normally open, as the electric charge is used to increase the length of the actuator such that the flow channel is closed.

A large voltage (150 V [5]) is required to increase the length of the actuator, which makes it possible to regulate

Figure 2.3: Geometry of the Piezo valve.

the movement of the actuator very precisely. This allows the regulating of smaller flows than possible with the common magnetic valves.

The most important part of the Piezo valve for the flow, the flow channel, is shown in figure 2.3. The flow enters through the gap indicated by 1 and leaves through the orifice, number 3. The membrane, 4, is regulated by the actuator and prevents the valve from leaking and regulates the throughflow height. In order to ensure
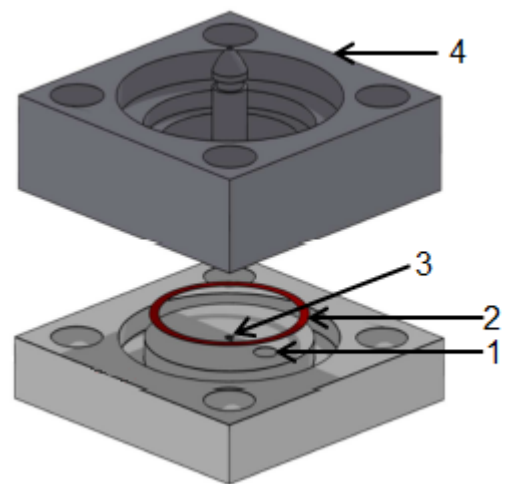
a good leak tightness, the membrane is lapped and polished. Furthermore, it is plastically deformed during the assembly process. After this deformation, the membrane is no longer flat, but the normal distance between orifice block and membrane will be smaller near the orifice (at the centre of the block). However, the exact shape of the membrane after deformation is not known [5]. The shim, number 2, creates distance between the orifice and the membrane, and is therefore also decisive for the throughflow height. The thicker the shim, the larger the required voltage to obtain the same throughflow height as for a thinner shim. In fact, the shim height is decisive for the throughflow height of the valve when no voltage is applied. However, the initial height of the membrane (i.e. the height when no voltage is applied) can be adjusted, such that the throughflow height is not necessarily equal to the shim height. Furthermore, the shape and the roughness of the membrane will also (partly) determine the throughflow height, as the height of the shim is in the order of micrometers [5].

In figure 2.4, the K_v-model has been tested for a Piezo valve, for 2 different shim heights h. It is clearly seen that the results differ significantly for the different shim heights, but the K_v-model does not take this into account. Hence, characterising a Piezo valve with the K_v-value is inappropriate for this valve, as the maximum flow is dominated by the throughflow height rather than by the orifice diameter [5]. Therefore, a model to determine the capacity as a function of the operating and the geometrical conditions should be developed. In an earlier study, a model (with limited validity) was developed for liquids [6]. Therefore, this study aims at developing a model for gases that can determine the capacity of microfluidic valves with given operating and geometrical conditions.
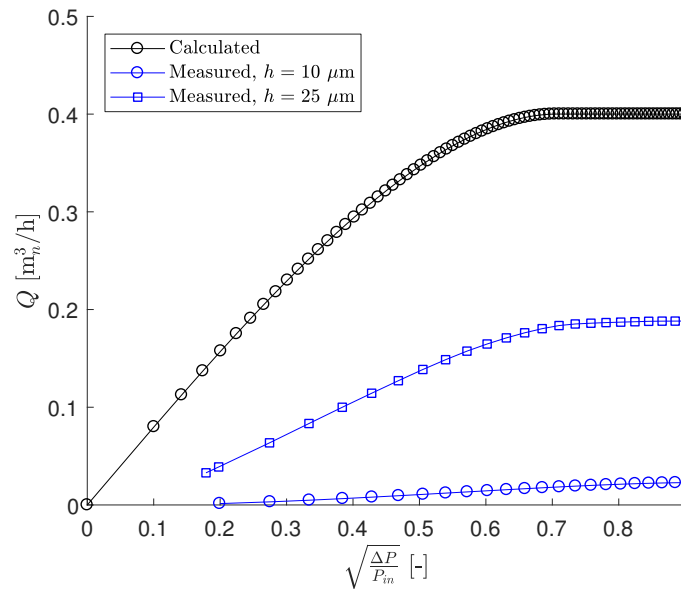

Figure 2.4: Calculated and measured air flow for a piezo valve (with 2 different shim heights h) with an orifice diameter of 0.5 mm and inlet pressure $P_{in} = 7$ bar (measurement data from [7]).

2.3 Main question and subquestions

The goal of the study has been formulated as the main question as follows:

How does the gas mass flow rate in a microfluidic valve depend on the geometrical properties, the type of gas and the operating conditions?

In order to answer the main question, several subquestions were formulated:

- What is the standard K_v-value calculation based on?

- What geometrical parameters characterize a microfluidic valve?

- Which gas parameters and operating conditions characterize the flow in a microfluidic valve?

- How does the flow behave in a valve with low throughflow height?

- How do the theoretical relations compare to reality?

The first subquestion is meant to find an explanation for the deviation between the calculated flow rate from the standard calculation and the actual flow rate. By closely looking into the derivation of the K_v-value (or to the assumptions made in the derivation), it is investigated whether a correction on this value for low throughflow heights may be feasible, or if an entire new model should be developed. The second subquestion is meant to correctly define the problem from a geometrical point of view, i.e. to investigate which dimensions are (or are not) of importance for the flow. The third subquestion aims at finding the important flow parameters, such that a model can be developed for the flow in the valve (fourth subquestion). When the flow within the valve is known for the important geometrical and flow parameters, the mass flow can be predicted as a function of these. This model will then be verified by measurements and, if possible, empirically improved (fifth subquestion).

3 K_v-value

In section 2.2, it was concluded that the K_v-model did not give accurate values for the flow through a Piezo valve. This is caused by the fact that the dominant factor, the throughflow height, is not taken into account in the K_v-model. However, another important observation can be made from figure 2.4: the correlation between the square root of the pressure drop and the normal volume flow is different for the Piezo valve compared to the magnetic valve, observed as a difference in shape of the graphs. This may indicate that the flow in a Piezo valve is characterised by a different regime than the flow in a magnetic valve. The possibility of a correction on the K_v-model for low throughflow heights will be investigated by looking more detailed into the K_v-value.

Although of common use in BHT, documentation on valve flow coefficients has been somewhat lacking: data on how K_v numbers were determined and documentation of testing procedures in BHT are lacking [12]. It is however known that the flow coefficients are dependent on valve geometry and only applicable for incompressible fluids and fully turbulent flows [12]. In appendix A, it is shown how the K_v-value for liquids can be derived from the Navier-Stokes equations. It is seen that, besides incompressible, the flow is assumed steady, one-dimensional and inviscid. Although an exact derivation for the K_v-value for gases could not be found, it is likely that these assumptions are also done for this factor. For the microchannels considered in this study, it is expected that viscosity will play a role. In addition, since gas flow is considered, compressibility effects will be of importance.
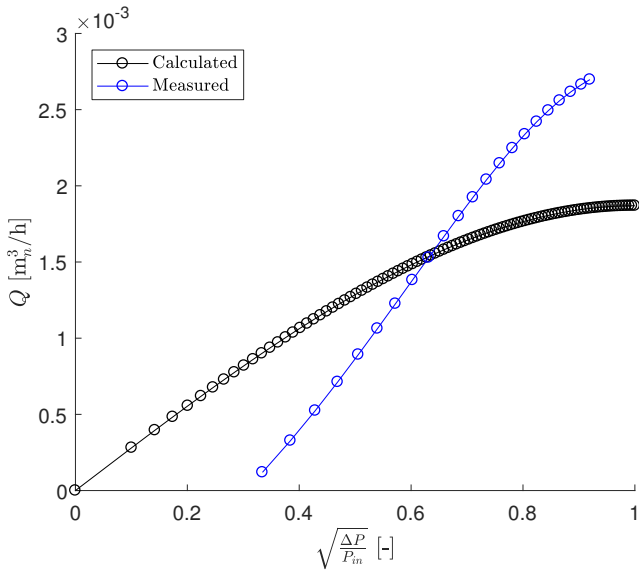
Figure 3.1: Compensated air flow rate, $h = 5$ μm, $d' = 0.5$ mm and $P_{in} = 7$ bar (data from [7]).
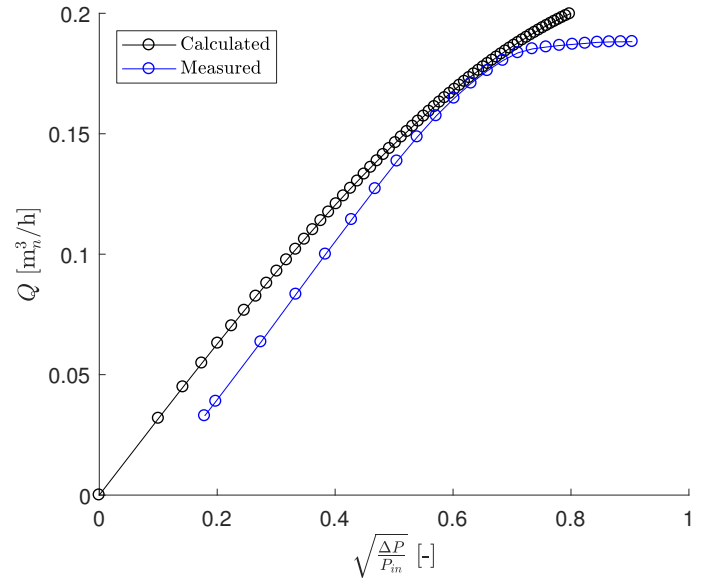
Figure 3.2: Compensated air flow rate, $h = 25$ μm, $d' = 0.5$ mm and $P_{in} = 7$ bar (data from [7]).

The NEN-IEC 60534 norm introduces additional factors to compensate for these and other (e.g. laminar instead of turbulent flow) effects [13], and it was tested in a previous study on the BHT Piezo valve [7]. By doing a "characterisation measurement", the valve coefficient is determined per height. This is done by applying a linear fit to the data in a plot with $\frac{\Delta P}{P_{in}}$ on the x-axis and $Y \cdot C$ on the y-axis, where Y is an expansion factor that accounts for a change in density and C is a compensated volume flow. The intersection of a linear fit to the curve and the y-axis is the K_v-value, and this value is used to calculate the flow for different situations. It appeared, however, that the data was not on an approximate linear curve, such that the approximation of the K_v-value was inaccurate. When this value was used to calculate the flow and the results were compared to the measurement data from which the K_v-value was determined, large deviations were observed. This is shown for shim heights of 5 and 25 μm (the smallest and largest height given) in figures 3.1 and 3.2, respectively. It can be seen that the calculated flow for a height of 25 μm is in the same order of magnitude as the measured flow, but differences upto a factor 2 are observed at low pressure drops. For pressure drops lower than the measured ones, the flow is presumably not linear related to the square root of the pressure drop, as is the case in the model. For a height of 5 μm, the calculated values deviate a lot from the measured values. The results show that correcting the K_v-value to expand its validity to compressible, viscous and laminar flows seems to have reached its limit, as both the values are not realistic and the relation between pressure drop and flow appears to be wrong.

4 Derivation of the Model

In section 2.2, the flow channel was described. In order to derive a model, it is proposed to simplify the geometry to a simple disk, as shown in figure 4.1. L is the radius of the disk, which is given by the inner radius of the shim. d is the orifice diameter, while h represents the throughflow height. The throughflow height is assumed constant, and should therefore be seen as an equivalent height. In practice, the shim height will probably be used as throughflow height, as it is the only representative height that is known. It is assumed that the flow comes from all sides and flows towards the centre, such that the channel is axisymmetric. The radial and lateral coordinates are denoted by r and z (respectively) and defined as shown in the figure.
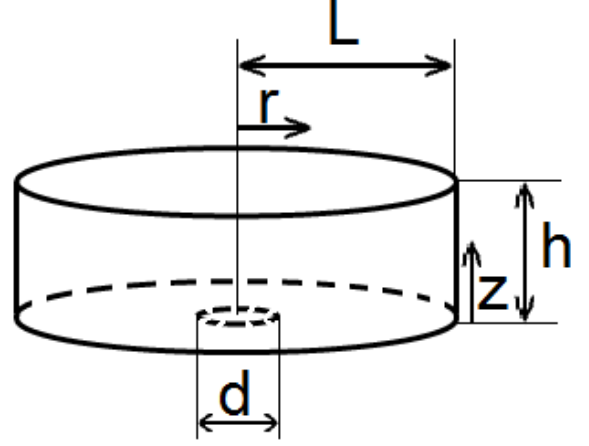
Figure 4.1: Simplified geometry of the Piezo valve.

The geometry of interest is characterised by its small height (ranging from 5 to 75 μm). For these microscale gas flows, the molecular mean free path of the gas, λ, becomes comparable to the characteristic length of the channel [14]. The characteristic length, or hydraulic diameter, is usually defined as $D_h = \frac{4A}{P}$ [14, 15] with A the flow-through area and P the periphery. For the disk-shaped channel that is used in the BHT Piezo valve, the hydraulic diameter is therefore equal to $D_h = 2h$, with h the height of the channel. The Knudsen number is defined as:

$$\text{Kn} = \frac{\lambda}{D_h} \tag{4.1}$$

For air at atmospheric pressure and room temperature, the mean free path is about 65 nm [16], resulting in Knudsen numbers in the range 10^{-3} to 10^{-4}. Flows with a Knudsen number lower than 10^{-3} are classified in the continuum regime, while flows with Knudsen numbers between 10^{-3} and 10^{-1} are classified in the slip flow regime [17]. Hence, flows through the considered channels may be in the slip flow regime, especially for the smallest channels. For the slip flow regime, the Navier-Stokes equations remain valid in the bulk, but not near the boundary [18]. They are however better than the Burnett equation [15]. Therefore, the Navier-Stokes equations are generally used to describe the flow, with a slip model to compensate near the boundaries [15, 19, 20].

4.1 Scaling of the Navier-Stokes equations

An analytical solution to the full Navier-Stokes equations (a set of non-linear partial differential equations) is not known, and numerical solving requires large computational effort. Several studies on microchannels have been done (for example [15, 19, 20]), but none of them used a disk-shaped channel. The obtained analytical solutions in these studies can therefore not be used. To obtain an analytical solution, the Navier-Stokes equations will be non-dimensionalised to find the most important terms and to reduce the number of parameters. Cylindrical coordinates are used to describe the flow. It is assumed that the flow is homogeneous in θ-direction and that there is no azimuthal velocity either. Hence, the flow is considered 2-dimensional. In addition, the flow is assumed to be steady, body forces are neglected and the flow is assumed isothermal. Since viscosity depends mainly on temperature, it is assumed constant in the channel as well. The resulting isothermal 2D Navier-Stokes equations in cylindrical coordinates are given in (4.2) (conservation of mass), (4.3) (conservation of momentum in radial direction) and (4.4) (conservation of momentum in lateral direction).

$$\frac{1}{r}\frac{\partial(\rho r u_r)}{\partial r} + \frac{\partial(\rho u_z)}{\partial z} = 0 \tag{4.2}$$

$$\rho\left(u_r\frac{\partial u_r}{\partial r} + u_z\frac{\partial u_r}{\partial u_z}\right) = -\frac{\partial P}{\partial r} + \mu\left(\frac{\partial^2 u_r}{\partial r^2} + \frac{\partial^2 u_r}{\partial z^2} + \frac{1}{3}\left(\frac{\partial^2 u_r}{\partial r^2} + \frac{\partial^2 u_z}{\partial r\partial z}\right)\right) + \frac{2\mu}{r}\left(\frac{\partial u_r}{\partial r} - \frac{u_r}{r}\right) \tag{4.3}$$

$$\rho\left(u_r\frac{\partial u_z}{\partial r} + u_z\frac{\partial u_z}{\partial z}\right) = -\frac{\partial P}{\partial z} + \mu\left(\frac{\partial^2 u_z}{\partial r^2} + \frac{\partial^2 u_z}{\partial z^2} + \frac{1}{3}\left(\frac{\partial^2 u_z}{\partial z^2} + \frac{\partial^2 u_r}{\partial r\partial z}\right)\right) + \frac{\mu}{r}\left(\frac{\partial u_r}{\partial z} + \frac{\partial u_z}{\partial r}\right) \tag{4.4}$$

The following scalings are introduced (a tilde denotes that the parameter is non-dimensional):

$$P = \tilde{P}P_{in}, \qquad \rho = \tilde{\rho}\rho_{in}, \qquad z = \tilde{z}h, \qquad r = \tilde{r}L, \qquad u_z = \tilde{u}_z\bar{u}_{in}, \qquad u_r = \tilde{u}_r\bar{u}_{in} \tag{4.5}$$

where P_{in} represents the pressure at the inlet, ρ_{in} represents the density at the inlet, h represents the (minimum) height of the channel, L represents the radius of the disk (the flow length) and $\bar{u}_{in}$ is the average radial velocity at the inlet. The reason for choosing the inlet parameters instead of the outlet parameters as scaling parameters is that, when the flow is choking, the flow parameters at the outlet may not be equal to the conditions one would expect based on the pressure and the temperature. These differences will then result in shock and expansion waves [21, p.291]. Substituting these scalings into the conservation of mass (4.2) gives:

$$\frac{\rho_{in}}{L\tilde{r}}\frac{\partial\left(\tilde{\rho}\tilde{r}\tilde{u}_r\right)}{\partial\tilde{r}} + \frac{\rho_{in}}{h}\frac{\partial\left(\tilde{\rho}\tilde{u}_z\right)}{\partial\tilde{z}} = 0 \tag{4.6}$$

Dividing by ρ_{in} and multiplying with h gives the scaled mass conservation equation:

$$\frac{\varepsilon}{\tilde{r}}\frac{\partial\left(\tilde{\rho}\tilde{r}\tilde{u}_r\right)}{\partial\tilde{r}} + \frac{\partial\left(\tilde{\rho}\tilde{u}_z\right)}{\partial\tilde{z}} = 0 \tag{4.7}$$

where ε is defined as:

$$\varepsilon \equiv \frac{h}{L} \tag{4.8}$$

Substituting the scalings into the conservation of momentum in radial direction (4.3) gives:

$$\rho_{in}\bar{u}_{in}^2\tilde{\rho}\left(\frac{\tilde{u}_r}{L}\frac{\partial\tilde{u}_r}{\partial\tilde{r}} + \frac{\tilde{u}_z}{h}\frac{\partial\tilde{u}_r}{\partial zt}\right) = \frac{-P_{in}}{L}\frac{\partial\tilde{P}}{\partial\tilde{r}}$$
$$+ \mu\bar{u}_{in}\left(\frac{1}{L^2}\frac{\partial^2\tilde{u}_r}{\partial\tilde{r}^2} + \frac{1}{h^2}\frac{\partial^2\tilde{u}_r}{\partial\tilde{z}^2} + \frac{1}{3}\left(\frac{1}{L^2}\frac{\partial^2\tilde{u}_r}{\partial\tilde{r}^2} + \frac{1}{Lh}\frac{\partial^2\tilde{u}_z}{\partial\tilde{r}\partial\tilde{z}}\right)\right) + \frac{2\mu\bar{u}_{in}}{L^2\tilde{r}}\left(\frac{\partial\tilde{u}_r}{\partial\tilde{r}} - \frac{\tilde{u}_r}{\tilde{r}}\right) \tag{4.9}$$

Multiplying the equation with $\frac{h^2}{\mu\bar{u}_{in}}$ gives:

$$\frac{\rho_{in}\bar{u}_{in}h}{\mu}\tilde{\rho}\left(\varepsilon\tilde{u}_r\frac{\partial\tilde{u}_r}{\partial\tilde{r}} + \tilde{u}_z\frac{\partial\tilde{u}_r}{\partial\tilde{z}}\right) = \frac{-\varepsilon P_{in}h}{\mu\bar{u}_{in}}\frac{\partial\tilde{P}}{\partial\tilde{r}} + \frac{4\varepsilon^2}{3}\frac{\partial^2\tilde{u}_r}{\partial\tilde{r}^2} + \frac{\partial^2\tilde{u}_r}{\partial\tilde{z}^2} + \frac{\varepsilon}{3}\frac{\partial^2\tilde{u}_z}{\partial\tilde{r}\partial\tilde{z}} + \frac{2\varepsilon^2}{\tilde{r}}\left(\frac{\partial\tilde{u}_r}{\partial\tilde{r}} - \frac{\tilde{u}_r}{\tilde{r}}\right) \tag{4.10}$$

The Reynolds number Re is now introduced, see (4.11). Furthermore, the ideal gas law (4.12) is assumed to be valid (with R the specific gas constant). Since the flow was assumed isothermal, this also means that $\tilde{\rho} = \tilde{P}$. For ideal gases, the speed of sound c is given by (4.13).

$$\text{Re} \equiv \frac{\rho_{in}\bar{u}_{in}h}{\mu} \tag{4.11}$$

$$P = \rho RT \tag{4.12}$$

$$c = \sqrt{\gamma RT} \tag{4.13}$$

$$\text{Ma} \equiv \frac{\bar{u}_{in}}{c} \tag{4.14}$$

With the Mach number as in (4.14), the dimensionless conservation of momentum in radial direction can finally be expressed as:

$$\text{Re}\tilde{P}\left(\varepsilon\tilde{u}_r\frac{\partial\tilde{u}_r}{\partial\tilde{r}} + \tilde{u}_z\frac{\partial\tilde{u}_r}{\partial\tilde{z}}\right) = \frac{-\varepsilon\text{Re}}{\gamma\text{Ma}^2}\frac{\partial\tilde{P}}{\partial\tilde{r}} + \frac{4\varepsilon^2}{3}\frac{\partial^2\tilde{u}_r}{\partial\tilde{r}^2} + \frac{\partial^2\tilde{u}_r}{\partial\tilde{z}^2} + \frac{\varepsilon}{3}\frac{\partial^2\tilde{u}_z}{\partial\tilde{r}\partial\tilde{z}} + \frac{2\varepsilon^2}{\tilde{r}}\left(\frac{\partial\tilde{u}_r}{\partial\tilde{r}} - \frac{\tilde{u}_r}{\tilde{r}}\right) \tag{4.15}$$

Similarly, the dimensionless conservation of momentum in lateral direction can be derived to be:

$$\text{Re}\tilde{P}\left(\varepsilon\tilde{u}_r\frac{\partial\tilde{u}_z}{\partial\tilde{r}} + \tilde{u}_z\frac{\partial\tilde{u}_z}{\partial\tilde{z}}\right) = \frac{-\text{Re}}{\gamma\text{Ma}^2}\frac{\partial\tilde{P}}{\partial\tilde{z}} + \frac{4}{3}\frac{\partial^2\tilde{u}_z}{\partial\tilde{z}^2} + \varepsilon^2\frac{\partial^2\tilde{u}_z}{\partial\tilde{r}^2} + \frac{\varepsilon}{3}\frac{\partial^2\tilde{u}_r}{\partial\tilde{r}\partial\tilde{z}} + \frac{\varepsilon}{\tilde{r}}\left(\frac{\partial\tilde{u}_r}{\partial\tilde{z}} + \varepsilon\frac{\partial\tilde{u}_z}{\partial\tilde{r}}\right) \tag{4.16}$$

As was done in the derivation for the dimensionless equations for conservation of momentum, the assumption of an ideal gas will now also be used in the mass conservation equation (4.7), such that the dimensionless density is replaced by the dimensionless pressure:

$$\frac{\varepsilon}{\tilde{r}}\frac{\partial\left(\tilde{P}\tilde{r}\tilde{u}_r\right)}{\partial\tilde{r}} + \frac{\partial\left(\tilde{P}\tilde{u}_z\right)}{\partial\tilde{z}} = 0 \tag{4.17}$$

4.2   Solving the Navier-Stokes Equations

Equations (4.15), (4.16) and (4.17) now forms the set of equations that is to be solved for $\tilde{u}_r$, $\tilde{u}_z$ and $\tilde{P}$. From the continuity equation, (4.17), it can be seen that the lateral velocity $\tilde{u}_z$ is of order ε. Assuming that Ma and Re are relatively small (both of $\mathcal{O}(\varepsilon)$) and neglecting all terms of $\mathcal{O}(\varepsilon)$ and higher (as ε is small for the considered geometry) reduces the conservation of momentum in $\tilde{z}$-direction (4.16) to:

$$\frac{-\mathrm{Re}}{\gamma \mathrm{Ma}^2} \frac{\partial \tilde{P}}{\partial \tilde{z}} = 0 \tag{4.18}$$

such that it is found that $\tilde{P}$ is constant with $\tilde{z}$ and hence it is only a function of $\tilde{r}$: $\tilde{P} = \tilde{P}(\tilde{r})$. Neglecting all terms of $\mathcal{O}(\varepsilon)$ and higher in the conservation of momentum in $\tilde{r}$-direction (4.15) gives:

$$\frac{-\varepsilon \mathrm{Re}}{\gamma \mathrm{Ma}^2} \frac{\mathrm{d}\tilde{P}}{\mathrm{d}\tilde{r}} + \frac{4}{3} \frac{\partial^2 \tilde{u}_r}{\partial \tilde{z}^2} = 0 \tag{4.19}$$

As it was found that $\tilde{P}$ is only a function of $\tilde{r}$, this equation can be integrated over $\tilde{z}$ twice to obtain an expression for $\tilde{u}_r$:

$$\tilde{u}_r(\tilde{r}, \tilde{z}) = \frac{\varepsilon \mathrm{Re}}{\gamma \mathrm{Ma}^2} \frac{\mathrm{d}\tilde{P}}{\mathrm{d}\tilde{r}} \left(\frac{1}{2} \tilde{z}^2 + c_a \tilde{z} + c_b \right) \tag{4.20}$$

It should be noted that the integration constants c_a and c_b are constant with $\tilde{z}$, but not necessarily with $\tilde{r}$. Therefore it is possible to take the (in $\tilde{z}$ constant) term $\frac{\varepsilon \mathrm{Re}}{\gamma \mathrm{Ma}^2} \frac{\mathrm{d}\tilde{P}}{\mathrm{d}\tilde{r}}$ in the integration constants and to write the expression for $\tilde{u}_r$ in the presented way. The constants are determined from the symmetry condition ($\frac{\partial \tilde{u}_r}{\partial \tilde{z}} \big|_{\tilde{z}=0.5} = 0$) and the slip condition at the boundary. A high-order slip boundary condition is given by [22] as:

$$u_{r,slip} = \frac{2 - \sigma}{\sigma} \left[\lambda \left(\frac{\partial u_r}{\partial \vec{n}} \right)_w + \frac{\lambda^2}{2} \left(\frac{\partial^2 u_r}{\partial \vec{n}^2} \right)_w + \frac{\lambda^3}{6} \left(\frac{\partial^3 u_r}{\partial \vec{n}^3} \right)_w + ... \right] \tag{4.21}$$

with $\vec{n}$ the inward normal vector. In non-dimensional form, this can be written as:

$$\tilde{u}_{r,slip} = \frac{2 - \sigma}{\sigma} \left[\pm 2\mathrm{Kn} \left(\frac{\partial \tilde{u}_r}{\partial \tilde{z}} \right)_w + 2\mathrm{Kn}^2 \left(\frac{\partial^2 \tilde{u}_r}{\partial \tilde{z}^2} \right)_w \pm \frac{4\mathrm{Kn}^3}{3} \left(\frac{\partial^3 \tilde{u}_r}{\partial \tilde{z}^3} \right)_w + ... \right] \tag{4.22}$$

(The minus signs are used on $\tilde{z} = 1$, as the inward normal should be used.) This shape is also obtained in earlier studies [20, 22], but the factors are different due to different scalings or a different definition of the Knudsen number. It can be seen that the no-slip condition follows naturally from this condition for small values of Kn (large characteristic lengths). The first order approximation was found to be valid in the entire slip flow regime [20], and therefore the boundary condition is formulated as:

$$\tilde{u}_{r,slip} = \pm 2C_1 \mathrm{Kn} \left(\frac{\partial \tilde{u}_r}{\partial \tilde{z}} \right)_w \tag{4.23}$$

which is similar to many studies [15, 19, 20, 22, 23]. Common values for the slip coefficient C_1 are 1 or 1.1466 [15]. In this study, $C_1 = 1$ is used. The symmetry condition gives:

$$\frac{\varepsilon \mathrm{Re}}{\gamma \mathrm{Ma}^2} \frac{\mathrm{d}\tilde{P}}{\mathrm{d}\tilde{r}} \left(\frac{1}{2} + c_a \right) = 0 \Rightarrow c_a = -\frac{1}{2} \tag{4.24}$$

The slip boundary condition (4.23) at $\tilde{z} = 0$ and $\tilde{z} = 1$ (which give the same condition) gives:

$$\frac{\varepsilon \mathrm{Re}}{\gamma \mathrm{Ma}^2} c_b = 2C_1 \mathrm{Kn} \frac{\varepsilon \mathrm{Re}}{\gamma \mathrm{Ma}^2} \cdot \frac{-1}{2} \Rightarrow c_b = -C_1 \mathrm{Kn} \tag{4.25}$$

Hence, the radial velocity is given by:

$$\tilde{u}_r(\tilde{r}, \tilde{z}) = \frac{\varepsilon \mathrm{Re}}{2\gamma \mathrm{Ma}^2} \frac{\mathrm{d}\tilde{P}}{\mathrm{d}\tilde{r}} \left(\tilde{z}^2 - \tilde{z} - 2C_1 \mathrm{Kn} \right) \tag{4.26}$$

Because $\tilde{z}$ is, by definition, between 0 and 1, it follows that the radial velocity is always in the direction of decreasing pressure, as one would expect. Since the mean free path depends on pressure, the Knudsen number is a function of $\tilde{r}$. In order to eliminate this indirect dependence, an alternative expression for the Knudsen number can be used [19, 23]:

$$\text{Kn} = \frac{\lambda}{2h} = \frac{1}{2}\sqrt{\frac{\gamma\pi}{2}}\frac{\text{Ma}}{\text{Re}} \tag{4.27}$$

(the factor $\frac{1}{2}$ comes from the definition of Re with h and Kn with $2h$). Scaling with the Knudsen number at inlet, it is obtained that Kn can be expressed as $\text{Kn} = \frac{\text{Kn}_{in}}{\tilde{P}}$, such that the radial velocity of (4.26) turns into:

$$\tilde{u}_r(\tilde{r}, \tilde{z}) = \frac{\varepsilon \text{Re}}{2\gamma\text{Ma}^2}\frac{\mathrm{d}\tilde{P}}{\mathrm{d}\tilde{r}}\left(\tilde{z}^2 - \tilde{z} - 2C_1\frac{\text{Kn}_{in}}{\tilde{P}}\right) \tag{4.28}$$

Substituting $\tilde{P} = \tilde{P}(\tilde{r})$ and (4.28) into (4.17) gives:

$$\frac{\varepsilon}{\tilde{r}}\frac{\partial}{\partial \tilde{r}}\left(\frac{\varepsilon\text{Re}\tilde{r}}{2\gamma\text{Ma}^2}\frac{\mathrm{d}\tilde{P}}{\mathrm{d}\tilde{r}}\left(\tilde{z}^2\tilde{P} - \tilde{z}\tilde{P} - 2C_1\text{Kn}_{in}\right)\right) + \tilde{P}\frac{\partial \tilde{u}_z}{\partial \tilde{z}} = 0 \tag{4.29}$$

Working out the differential yields:

$$\frac{\partial \tilde{u}_z}{\partial \tilde{z}} = \frac{-\varepsilon^2\text{Re}}{2\gamma\text{Ma}^2}\left(\frac{\tilde{z}^2}{\tilde{r}}\frac{\mathrm{d}\tilde{P}}{\mathrm{d}\tilde{r}} + \frac{\tilde{z}^2}{2\tilde{P}}\frac{\mathrm{d}^2\tilde{P}^2}{\mathrm{d}\tilde{r}^2} - \frac{\tilde{z}}{\tilde{r}}\frac{\mathrm{d}\tilde{P}}{\mathrm{d}\tilde{r}} - \frac{\tilde{z}}{2\tilde{P}}\frac{\mathrm{d}^2\tilde{P}^2}{\mathrm{d}\tilde{r}^2} - \frac{2C_1\text{Kn}_{in}}{\tilde{r}\tilde{P}}\frac{\mathrm{d}\tilde{P}}{\mathrm{d}\tilde{r}} - \frac{2C_1\text{Kn}_{in}}{\tilde{P}}\frac{\mathrm{d}^2\tilde{P}}{\mathrm{d}\tilde{r}^2}\right) \tag{4.30}$$

Integrating over $\tilde{z}$ gives an expression for $\tilde{u}_z$:

$$\tilde{u}_z(\tilde{r}, \tilde{z}) = \frac{-\varepsilon^2\text{Re}}{2\gamma\text{Ma}^2}\left(\frac{\tilde{z}^3}{3\tilde{r}}\frac{\mathrm{d}\tilde{P}}{\mathrm{d}\tilde{r}} + \frac{\tilde{z}^3}{6\tilde{P}}\frac{\mathrm{d}^2\tilde{P}^2}{\mathrm{d}\tilde{r}^2} - \frac{\tilde{z}^2}{2\tilde{r}}\frac{\mathrm{d}\tilde{P}}{\mathrm{d}\tilde{r}} - \frac{\tilde{z}^2}{4\tilde{P}}\frac{\mathrm{d}^2\tilde{P}^2}{\mathrm{d}\tilde{r}^2} - \frac{2C_1\text{Kn}_{in}\tilde{z}}{\tilde{r}\tilde{P}}\frac{\mathrm{d}\tilde{P}}{\mathrm{d}\tilde{r}} - \frac{2C_1\text{Kn}_{in}\tilde{z}}{\tilde{P}}\frac{\mathrm{d}^2\tilde{P}}{\mathrm{d}\tilde{r}^2}\right) \tag{4.31}$$

where the integration constant was set to 0, as follows from the boundary condition $\tilde{u}_z(\tilde{r}, \tilde{z} = 0) = 0$. From $\tilde{u}_z(\tilde{r}, \tilde{z} = 1) = 0$ it follows that:

$$\frac{-\varepsilon^2\text{Re}}{2\gamma\text{Ma}^2}\left(\frac{-1}{6\tilde{r}}\frac{\mathrm{d}\tilde{P}}{\mathrm{d}\tilde{r}} - \frac{1}{12\tilde{P}}\frac{\mathrm{d}^2\tilde{P}^2}{\mathrm{d}\tilde{r}^2} - \frac{2C_1\text{Kn}_{in}}{\tilde{r}\tilde{P}}\frac{\mathrm{d}\tilde{P}}{\mathrm{d}\tilde{r}} - \frac{2C_1\text{Kn}_{in}}{\tilde{P}}\frac{\mathrm{d}^2\tilde{P}}{\mathrm{d}\tilde{r}^2}\right) = 0 \tag{4.32}$$

From this condition $\tilde{P}$ is obtained:

$$\tilde{P}(\tilde{r}) = -12C_1\text{Kn}_{in} + \sqrt{(12C_1\text{Kn}_{in})^2 + c_a + c_b\ln(\tilde{r})} \tag{4.33}$$

The constants can be solved from the boundary conditions $\tilde{P}(\tilde{r} = 1) = 1$ and $\tilde{P}(\tilde{r} = \frac{d}{2L}) = \frac{P_{out}}{P_{in}}$:

$$\tilde{P}(\tilde{r} = 1) = 1 \Rightarrow c_a = 1 + 24C_1\text{Kn}_{in} \tag{4.34}$$

$$\tilde{P}\left(\tilde{r} = \frac{d}{2L}\right) = \frac{P_{out}}{P_{in}} \Rightarrow c_b = \frac{\left(\frac{P_{out}}{P_{in}}\right)^2 + 24C_1\text{Kn}_{in}\left(\frac{P_{out}}{P_{in}} - 1\right) - 1}{\ln\left(\frac{d}{2L}\right)} \tag{4.35}$$

Hence, the pressure is described as:

$$\tilde{P}(\tilde{r}) = -12C_1\text{Kn}_{in} + \sqrt{(1 + 12C_1\text{Kn}_{in})^2 + \left(\left(\frac{P_{out}}{P_{in}}\right)^2 + 24C_1\text{Kn}_{in}\left(\frac{P_{out}}{P_{in}} - 1\right) - 1\right)\frac{\ln(\tilde{r})}{\ln\left(\frac{d}{2L}\right)}} \tag{4.36}$$

The flow in the channel for small Re and Ma is given by (4.28), (4.31) and (4.36). For convenience, the dimensional variants of u_r (with the derivative worked out) and P are given in (4.37) and (4.38), respectively. u_z is an order ε smaller and relatively unimportant, and therefore it was left out. The influences of the geometry

(h, d and L), medium properties and using conditions (temperature, pressures) are, as expected, clearly present in the equations.

$$u_r(r,z) = \frac{P_{in}h^2\left[\left(\frac{P_{out}}{P_{in}}\right)^2 + 24C_1\mathrm{Kn}_{in}\left(\frac{P_{out}}{P_{in}}-1\right)-1\right]\left[\left(\frac{z}{h}\right)^2 - \frac{z}{h} - \frac{2C_1\mathrm{Kn}_{in}P_{in}}{P(r)}\right]}{4\mu r \ln\left(\frac{d}{2L}\right)\sqrt{(1+12C_1\mathrm{Kn}_{in})^2 + \left(\left(\frac{P_{out}}{P_{in}}\right)^2 + 24C_1\mathrm{Kn}_{in}\left(\frac{P_{out}}{P_{in}}-1\right)-1\right)\frac{\ln\left(\frac{r}{L}\right)}{\ln\left(\frac{d}{2L}\right)}}} \tag{4.37}$$

$$P(r) = -12C_1\mathrm{Kn}_{in}P_{in} + \sqrt{(P_{in}+12C_1\mathrm{Kn}_{in}P_{in})^2 + \left(P_{out}^2 - P_{in}^2 + 24C_1\mathrm{Kn}_{in}P_{in}\left(P_{out}-P_{in}\right)\right)\frac{\ln\left(\frac{r}{L}\right)}{\ln\left(\frac{d}{2L}\right)}} \tag{4.38}$$

In order to visualize the obtained velocity profile, it has been plotted for a certain (representative) situation, see figure 4.2. For this visualization, and in the rest of the report, the viscosity is calculated using Sutherland's law. This is explained further in appendix B. In the figure, it can be seen that the velocity increases very rapidly near the outlet ($\tilde{r} = \frac{d}{2L}$). In order to get a better view of the radial velocity in height elsewhere, a section view (for different inlet pressures) was made at $\tilde{r} = 0.2$, as shown in figure 4.3. It can be seen that the profile is, as expected, quadratic in $\tilde{z}$ and symmetric around the centre of the channel. Furthermore, the influence of the adopted slip condition can be observed as a non-zero velocity along the walls. In figure 4.4, the pressure profile has been plotted along the channel. It is seen that the pressure decreases very rapidly near the outlet, while it is relatively constant near the inlet. This corresponds to the rapid increase in radial velocity that was observed.
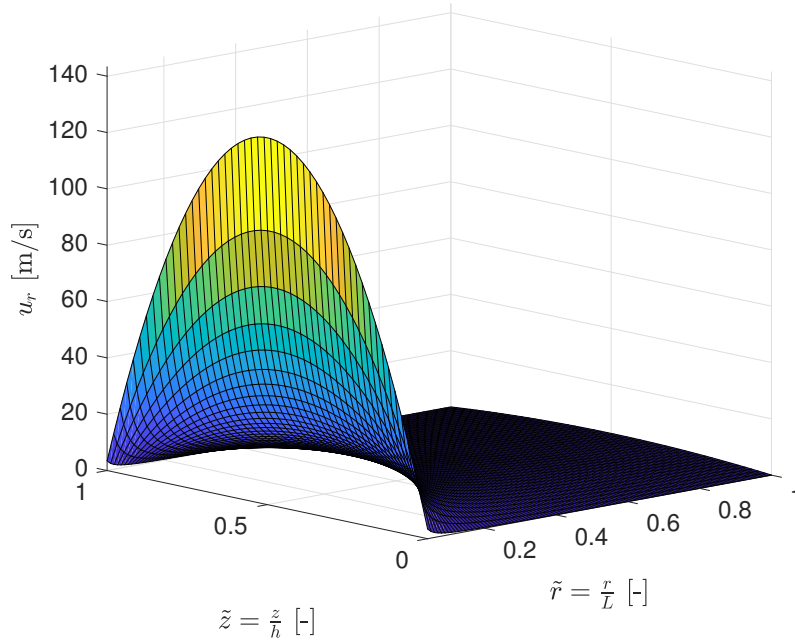
Figure 4.2: Absolute radial velocity in m/s according to (4.37) as a function of the (dimensionless) radial and lateral coordinates for $h = 10$ μm, $P_{in} = 2$ bar, $P_{out} = 1$ bar, $L = 6$ mm, $d = 0.5$ mm and air at $T = 293$ K as medium.

The average radial velocity is now derived from (4.37) and is given by:

$$\bar{u}_r(r) = \frac{-P_{in}h^2\left[\left(\frac{P_{out}}{P_{in}}\right)^2 + 24C_1\mathrm{Kn}_{in}\left(\frac{P_{out}}{P_{in}}-1\right)-1\right]\left[\frac{1}{6} + \frac{2C_1\mathrm{Kn}_{in}P_{in}}{P(r)}\right]}{4\mu r \ln\left(\frac{d}{2L}\right)\sqrt{(1+12C_1\mathrm{Kn}_{in})^2 + \left(\left(\frac{P_{out}}{P_{in}}\right)^2 + 24C_1\mathrm{Kn}_{in}\left(\frac{P_{out}}{P_{in}}-1\right)-1\right)\frac{\ln\left(\frac{r}{L}\right)}{\ln\left(\frac{d}{2L}\right)}}} \tag{4.39}$$

The volumetric flow rate, see (4.40), is obtained by multiplying the average velocity with the throughflow area ($2\pi rh$), and the mass flow rate, see (4.41), is obtained by multiplying the average velocity with the throughflow area and the density. As the mass flow is constant throughout the channel, this will give the same result everywhere and hence it is no function of r.
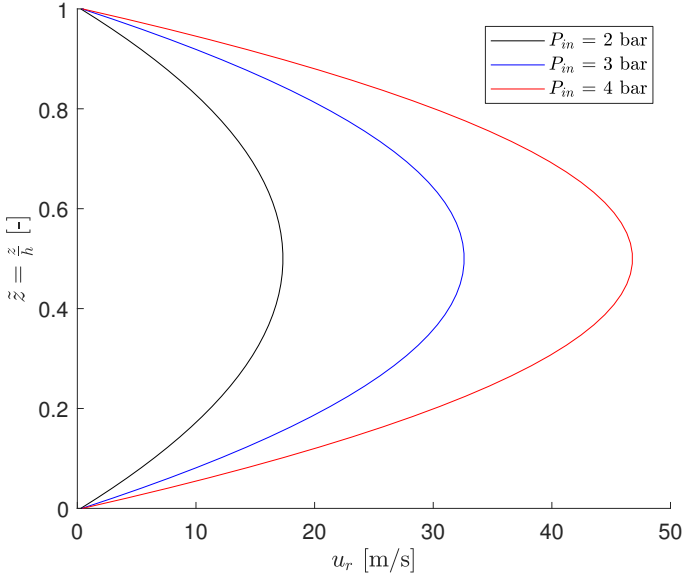
Figure 4.3: Section view of the absolute radial velocity at $\tilde{r} = 0.2$ for $h = 10\ \mu\text{m}$, $P_{out} = 1$ bar, $L = 6$ mm, $d = 0.5$ mm and air at $T = 293$ K as medium.
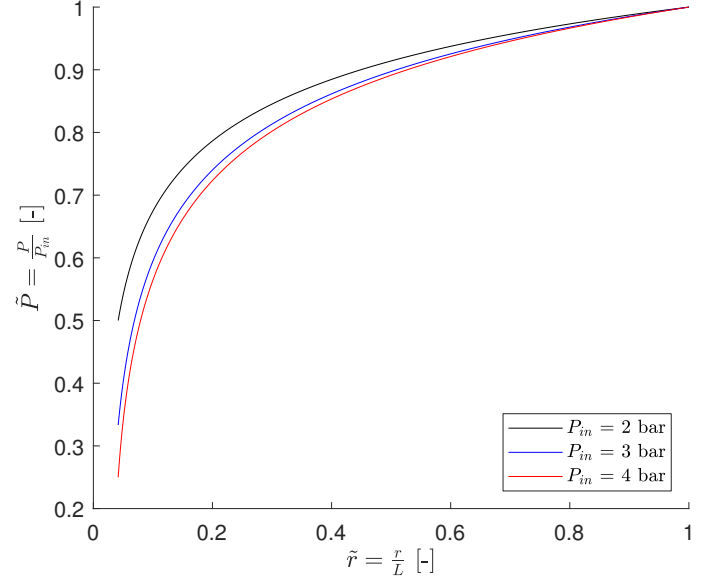
Figure 4.4: Dimensionless pressure along the channel for $h = 10\ \mu\text{m}$, $P_{out} = 1$ bar, $L = 6$ mm, $d = 0.5$ mm and air at $T = 293$ K as medium.

$$Q(r) = \frac{-\pi P_{in} h^3 \left[\left(\frac{P_{out}}{P_{in}} \right)^2 + 24 C_1 \text{Kn}_{in} \left(\frac{P_{out}}{P_{in}} - 1 \right) - 1 \right] \left[\frac{1}{6} + \frac{2 C_1 \text{Kn}_{in} P_{in}}{P(r)} \right]}{2\mu \ln \left(\frac{d}{2L} \right) \sqrt{\left(1 + 12 C_1 \text{Kn}_{in} \right)^2 + \left(\left(\frac{P_{out}}{P_{in}} \right)^2 + 24 C_1 \text{Kn}_{in} \left(\frac{P_{out}}{P_{in}} - 1 \right) - 1 \right) \frac{\ln \left(\frac{r}{L} \right)}{\ln \left(\frac{d}{2L} \right)}}} \tag{4.40}$$

$$\dot{m} = \frac{-\pi P_{in}^2 h^3 \left[\left(\frac{P_{out}}{P_{in}} \right)^2 + 24 C_1 \text{Kn}_{in} \left(\frac{P_{out}}{P_{in}} - 1 \right) - 1 \right] \left[\frac{1}{6} + 2 C_1 \text{Kn}_{in} \right]}{2\mu R T \ln \left(\frac{d}{2L} \right) \left(1 + 12 C_1 \text{Kn}_{in} \right)} \tag{4.41}$$

4.3   Choked Flow

As stated earlier, the derivation does not hold for high Re and Ma (i.e. $\mathcal{O}(\varepsilon^0)$ or more important). In normal operating conditions, it is likely that the assumptions are not always valid. However, taking more terms into account, such that it is accurate to higher Re and Ma, results in unsolvable partial differential equations (i.e. no analytical solution could be found). Instead of using FEM packages, it is chosen to investigate the behaviour of the obtained equations with some scaling factors added (that are to be determined empirically) at higher numbers for Re and Ma. The average velocity will therefore be multiplied by a factor F_1 to allow for some tuning of the equations to measurement data. This factor can also serve as a friction factor to account for losses before and after the geometry considered in the model and losses that are not taken into account in the model.

It is known that, when the maximum velocity in the channel (at the narrowest part, so at the outlet) approaches the speed of sound, the flow becomes choked. The velocity will no longer increase, and hence the mass flow rate can only be increased by increasing the inlet pressure and not by decreasing the outlet pressure [24]. This is because an increase in inlet pressure will lead to an increase in the density at the location of choking and, with the velocity and geometry remaining equal, this results in an increase in mass flow. However, a decrease in outlet pressure cannot be sensed upstream and will therefore not result in increased mass flow.

To take this effect into account in the model, it first needs to be determined whether there is choked flow or not. For a given value of P_{in}, the critical output pressure can be determined by setting the average radial velocity equal to minus the speed of sound c (minus, because flow is in the negative radial direction). However, according to [25], choking (mathematically) occurs at Mach numbers less than 1 for isothermal flow. Therefore, the average velocity $F_1 \bar{u}_r$ will be set equal to $-F_2 c$ to take this effect into account as well. Hence, the critical outlet pressure $P_{out,c}$ for a given value for P_{in} can be solved from (4.42), which follows from setting the average velocity at $r = \frac{d}{2}$ in (4.39) multiplied with the factor F_1 equal to $-F_2 c$.

When the outlet pressure is lower than the critical pressure, the pressure of the flow at the outlet will no longer follow the outlet pressure, but the gas is underexpanded [21]. Shock waves in the orifice (or the pipe behind it) may form to overcome this pressure difference. In the model, the pressure at the outlet for choked flow is constrained at the critical pressure, and hence the pressure profile becomes as described in (4.43) (where subscripts "out" and "in" were abbreviated to "o" and "i", respectively). For the velocity, a similar situation as for the pressure holds. When the outlet pressure is higher than this critical outlet pressure, the velocity is the same as calculated determined from (4.39) with a given inlet and outlet pressure. However, if the outlet pressure is lower than the critical outlet pressure, the flow is choked and the velocity field is expected to be the same as in the critical situation. This behaviour for the velocity is given in (4.44). The mass flow is obtained by multiplying the average velocity at the inlet with the flow-through area and the density at the inlet, see (4.45). In this equation, it is clearly seen that, when the flow is choked, lowering the outlet pressure will not lead to an increase in mass flow, as the velocity remains the same. An increase in inlet pressure will however increase the mass flow rate (although not linear, because the critical pressure changes as well).

$$
F_2 c = \frac{F_1 P_{in} h^2 \left[\left(\frac{P_{out,c}}{P_{in}} \right)^2 - 1 + 24 C_1 \mathrm{Kn}_{in} \left(\frac{P_{out,c}}{P_{in}} - 1 \right) \right] \left[\frac{1}{6} + \frac{2 C_1 \mathrm{Kn}_{in} P_{in}}{P_{out,c}} \right]}{2 \mu d \ln \left(\frac{d}{2L} \right) \left(\frac{P_{out,c}}{P_{in}} + 12 C_1 \mathrm{Kn}_{in} \right)}
\tag{4.42}
$$

$$
P(r) = \begin{cases}
-12 C_1 \mathrm{Kn}_i P_i + P_i \sqrt{(1 + 12 C_1 \mathrm{Kn}_i)^2 + \left(\left(\frac{P_o}{P_i} \right)^2 - 1 + 24 C_1 \mathrm{Kn}_i \left(\frac{P_o}{P_i} - 1 \right) \right) \frac{\ln \left(\frac{r}{L} \right)}{\ln \left(\frac{d}{2L} \right)}}, & P_o \geq P_{o,c} \\[4mm]
-12 C_1 \mathrm{Kn}_i P_i + P_i \sqrt{(1 + 12 C_1 \mathrm{Kn}_i)^2 + \left(\left(\frac{P_{o,c}}{P_i} \right)^2 - 1 + 24 C_1 \mathrm{Kn}_i \left(\frac{P_{o,c}}{P_i} - 1 \right) \right) \frac{\ln \left(\frac{r}{L} \right)}{\ln \left(\frac{d}{2L} \right)}}, & P_o < P_{o,c}
\end{cases}
\tag{4.43}
$$

$$
\bar{u}_r(r) = \begin{cases}
\dfrac{-F_1 P_{in} h^2 \left[\left(\frac{P_{out}}{P_{in}} \right)^2 + 24 C_1 \mathrm{Kn}_{in} \left(\frac{P_{out}}{P_{in}} - 1 \right) - 1 \right] \left[\frac{1}{6} + \frac{2 C_1 \mathrm{Kn}_{in} P_{in}}{P(r)} \right]}{4 \mu r \ln \left(\frac{d}{2L} \right) \sqrt{(1 + 12 C_1 \mathrm{Kn}_{in})^2 + \left(\left(\frac{P_{out}}{P_{in}} \right)^2 + 24 C_1 \mathrm{Kn}_{in} \left(\frac{P_{out}}{P_{in}} - 1 \right) - 1 \right) \frac{\ln \left(\frac{r}{L} \right)}{\ln \left(\frac{d}{2L} \right)}}}, & P_{out} \geq P_{out,c} \\[8mm]
\dfrac{-F_1 P_{in} h^2 \left[\left(\frac{P_{out,c}}{P_{in}} \right)^2 + 24 C_1 \mathrm{Kn}_{in} \left(\frac{P_{out,c}}{P_{in}} - 1 \right) - 1 \right] \left[\frac{1}{6} + \frac{2 C_1 \mathrm{Kn}_{in} P_{in}}{P(r)} \right]}{4 \mu r \ln \left(\frac{d}{2L} \right) \sqrt{(1 + 12 C_1 \mathrm{Kn}_{in})^2 + \left(\left(\frac{P_{out,c}}{P_{in}} \right)^2 + 24 C_1 \mathrm{Kn}_{in} \left(\frac{P_{out,c}}{P_{in}} - 1 \right) - 1 \right) \frac{\ln \left(\frac{r}{L} \right)}{\ln \left(\frac{d}{2L} \right)}}}, & P_{out} < P_{out,c}
\end{cases}
\tag{4.44}
$$

$$
\dot{m} = 2 \pi L h \frac{P_{in}}{RT} \bar{u}_r(r = L)
\tag{4.45}
$$

When the valve is used to regulate the flow, the height will be changed to achieve the desired flow. For a better insight on how the flow, according to this model, will respond to a change in height the reader is referred to appendix C.

4.4   Reversed Flow

In the model, the flow was assumed to flow towards the centre, which is the direction that is currently used. However, it was observed that the velocity increased rapidly near the centre of the disk. This is caused by the combination of the expansion of the fluid and the geometry of the channel. The throughflow area decreases towards the centre, such that, in order to get the same mass flow through it, the velocity needs to increase. It was stated that when the velocity reaches the speed of sound, the flow chokes. Increasing the mass flow rate (for a constant height) was then only possible by increasing the inlet pressure. The choking of the flow limited the maximum mass flow significantly. When a relatively high flow rate is desired, this behaviour is undesired and

it would be beneficial to lower the critical outlet pressure. From a geometrical point of view, it would therefore be beneficial to reverse the flow direction (i.e. have the inflow at the centre of the disk and flow outwards). The geometrical acceleration is in this way removed, such that the maximum occuring velocity for certain operating conditions and outward flow is lower than for the same operating conditions with inward flow. Therefore, the maximum flow rate (in choked conditions) may be increased. In order to describe the reversed (outward) flow, the boundary conditions are changed. Upto (4.33), the derivation still holds. However, in this case the constants are solved from the boundary conditions $\tilde{P}(\tilde{r} = 1) = \frac{P_{out}}{P_{in}}$ and $\tilde{P}(\tilde{r} = \frac{d}{2L}) = 1$:

$$\tilde{P}(\tilde{r} = 1) = \frac{P_{out}}{P_{in}} \Rightarrow c_a = \left(\frac{P_{out}}{P_{in}}\right)^2 + 24C_1\mathrm{Kn}_{in}\frac{P_{out}}{P_{in}} \tag{4.46}$$

$$\tilde{P}(\tilde{r} = \frac{d}{2L}) = 1 \Rightarrow c_b = \frac{1 - \left(\frac{P_{out}}{P_{in}}\right)^2 + 24C_1\mathrm{Kn}_{in}\left(1 - \frac{P_{out}}{P_{in}}\right)}{\ln\left(\frac{d}{2L}\right)} \tag{4.47}$$

Hence, the pressure profile is, for outward flow, described as:

$$\tilde{P}(\tilde{r}) = -12C_1\mathrm{Kn}_{in} + \sqrt{\left(\frac{P_{out}}{P_{in}} + 12C_1\mathrm{Kn}_{in}\right)^2 + \left(1 - \left(\frac{P_{out}}{P_{in}}\right)^2 + 24C_1\mathrm{Kn}_{in}\left(1 - \frac{P_{out}}{P_{in}}\right)\right)\frac{\ln(\tilde{r})}{\ln\left(\frac{d}{2L}\right)}} \tag{4.48}$$

The average radial velocity is then given by:

$$\bar{u}_r(r) = \frac{-P_{in}h^2\left[1 - \left(\frac{P_{out}}{P_{in}}\right)^2 + 24C_1\mathrm{Kn}_{in}\left(1 - \frac{P_{out}}{P_{in}}\right)\right]\left[\frac{1}{6} + \frac{2C_1\mathrm{Kn}_{in}P_{in}}{P(r)}\right]}{4\mu r\ln\left(\frac{d}{2L}\right)\sqrt{\left(\frac{P_{out}}{P_{in}} + 12C_1\mathrm{Kn}_{in}\right)^2 + \left(1 - \left(\frac{P_{out}}{P_{in}}\right)^2 + 24C_1\mathrm{Kn}_{in}\left(1 - \frac{P_{out}}{P_{in}}\right)\right)\frac{\ln(\tilde{r})}{\ln\left(\frac{d}{2L}\right)}}} \tag{4.49}$$

Also for outward flow, the maximum velocity occurs at the centre of the channel. When choking is implemented similarly as was done for inward flow, the critical outlet pressure for a certain inlet pressure should be calculated from (4.50). This equation follows from setting (4.49) with the factor F_1 at the critical location $r = \frac{d}{2}$ equal to $F_2 c$. The pressure and average radial velocity are then given by (4.51) and (4.52), respectively. The calculation of the mass flow remains unchanged, but is shown again in (4.53).

$$F_2 c = \frac{-F_1 P_{in}h^2\left[1 - \left(\frac{P_{out,c}}{P_{in}}\right)^2 + 24C_1\mathrm{Kn}_{in}\left(1 - \frac{P_{out,c}}{P_{in}}\right)\right]}{12\mu d\ln\left(\frac{d}{2L}\right)} \tag{4.50}$$

$$P(r) = \begin{cases} -12C_1\mathrm{Kn}_iP_i + P_i\sqrt{\left(\frac{P_o}{P_i} + 12C_1\mathrm{Kn}_i\right)^2 + \left(1 - \left(\frac{P_o}{P_i}\right)^2 + 24C_1\mathrm{Kn}_i\left(1 - \frac{P_o}{P_i}\right)\right)\frac{\ln(\tilde{r})}{\ln\left(\frac{d}{2L}\right)}}, & P_o \geq P_{o,c} \\[3em] -12C_1\mathrm{Kn}_iP_i + P_i\sqrt{\left(\frac{P_{o,c}}{P_i} + 12C_1\mathrm{Kn}_i\right)^2 + \left(1 - \left(\frac{P_{o,c}}{P_i}\right)^2 + 24C_1\mathrm{Kn}_i\left(1 - \frac{P_{o,c}}{P_i}\right)\right)\frac{\ln(\tilde{r})}{\ln\left(\frac{d}{2L}\right)}}, & P_o < P_{o,c} \end{cases} \tag{4.51}$$

$$\bar{u}_r(r) = \begin{cases} \dfrac{-F_1 P_ih^2\left[1 - \left(\frac{P_o}{P_i}\right)^2 + 24C_1\mathrm{Kn}_i\left(1 - \frac{P_o}{P_i}\right)\right]\left[\frac{1}{6} + \frac{2C_1\mathrm{Kn}_iP_i}{P(r)}\right]}{4\mu r\ln\left(\frac{d}{2L}\right)\sqrt{\left(\frac{P_o}{P_i} + 12C_1\mathrm{Kn}_i\right)^2 + \left(1 - \left(\frac{P_o}{P_i}\right)^2 + 24C_1\mathrm{Kn}_i\left(1 - \frac{P_o}{P_i}\right)\right)\frac{\ln(\tilde{r})}{\ln\left(\frac{d}{2L}\right)}}}, & P_o \geq P_{o,c} \\[4em] \dfrac{-F_1 P_ih^2\left[1 - \left(\frac{P_{o,c}}{P_i}\right)^2 + 24C_1\mathrm{Kn}_i\left(1 - \frac{P_{o,c}}{P_i}\right)\right]\left[\frac{1}{6} + \frac{2C_1\mathrm{Kn}_iP_i}{P(r)}\right]}{4\mu r\ln\left(\frac{d}{2L}\right)\sqrt{\left(\frac{P_{o,c}}{P_i} + 12C_1\mathrm{Kn}_i\right)^2 + \left(1 - \left(\frac{P_{o,c}}{P_i}\right)^2 + 24C_1\mathrm{Kn}_i\left(1 - \frac{P_{o,c}}{P_i}\right)\right)\frac{\ln(\tilde{r})}{\ln\left(\frac{d}{2L}\right)}}}, & P_o < P_{o,c} \end{cases} \tag{4.52}$$

$$\dot{m} = 2\pi Lh\frac{P_{in}}{RT}\bar{u}_r(r = L) \tag{4.53}$$

5   Measurements

In order to check and improve the proposed model, measurements need to be done. For different throughflow heights, the mass flow will be determined as a function of the pressures, temperature and type of gas. This section describes the experimental setup and the method that will be used. It was derived from an earlier study on the same topic by Korenblik [7]. The results of the measurements will be presented in the next chapter and appendix E, in combination with the validation and improvement of the model.

5.1   Experimental Setup

The measurements will be done on a test Piezo valve. This valve consists of five different components. The basis is a block through which the flow will enter and leave this testing device. On the block, an orifice is placed. On top of the orifice, a shim is placed, which determines the throughflow height. A membrane is placed on top of the orifice and shim and should prevent the valve from leaking. Lastly, four bolts are used to keep the components together. Fastening the bolts should be done using a torque wrench, as it may influence the throughflow height of the channel. A torque of 2 Nm will be used.

The experimental setup consists of the following components:

1. Stand alone valve

2. Pressure meter EL-PRESS, maximum 10 bar

3. Test Piezo valve (DUT)

4. Pressure difference meter EL-PRESS, maximum 5 bar

5. Stand alone valve

6. Flow meter EL-FLOW (different capacities)

7. Connectors
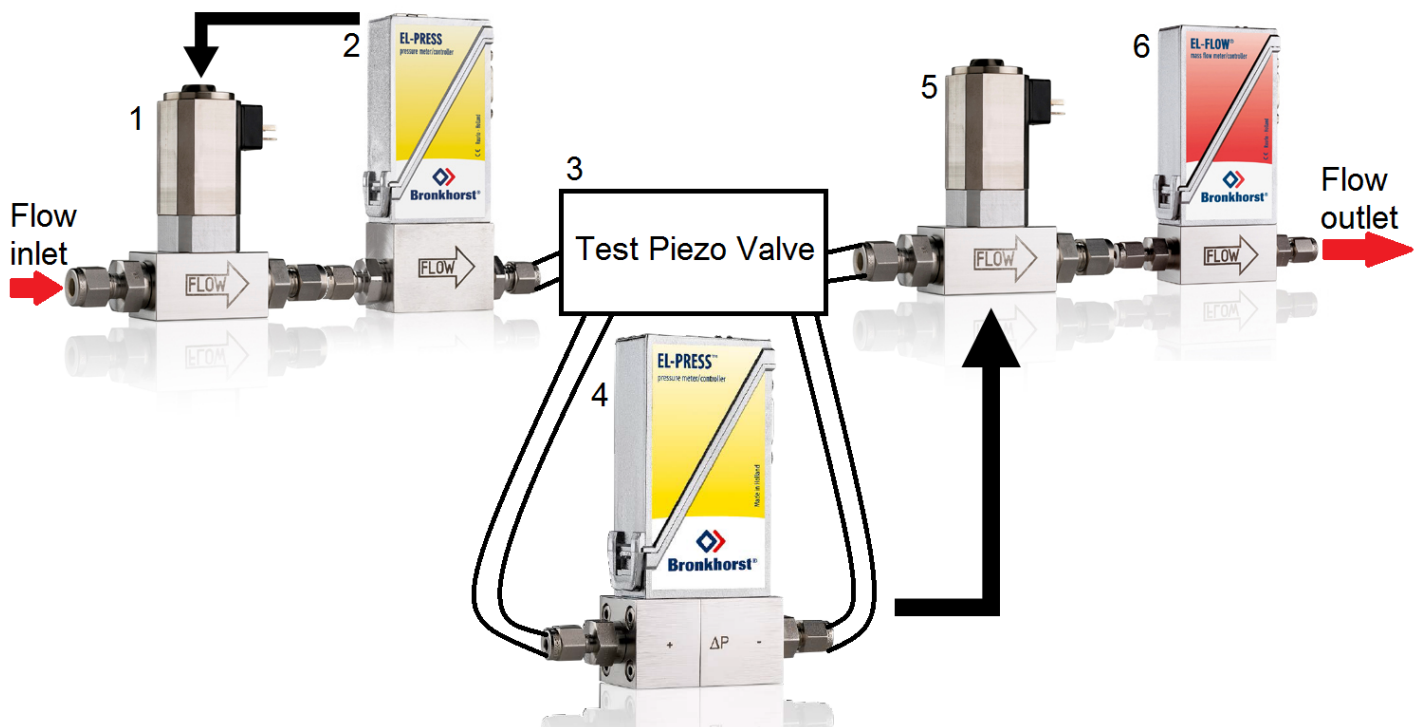
Figure 5.1: Schematic visualisation of the experimental setup. The black arrows indicate how the signal of the pressure meters is used to regulate the pressure.

The setup is shown schematically in figure 5.1, where the numbers refer to the list above. Photographs of the setup and the test Piezo valve are shown in appendix D. In addition to the listed components, a computer with the software FlowDDE, Flowplot and Excel, cables to connect the instruments, a transformer for communication between the instruments and the computer and a conditioned room to do the experiments are required. The following data will be recorded:

1. Pressure at inlet

2. Pressure difference over the valve

3. Volume flow at normal conditions

It should be noted that the EL-FLOW sensors are not capable of measuring density. They are capable of giving a value for volume flow, but this is a volume flow at normal conditions, for the European standard given by atmospheric pressure and a temperature of 0 °C [10]. Hence, it is in fact a scaled mass flow, as the conditions on which the density is calculated remain equal under all circumstances.

5.2   Method

Measurements will be done with air, argon, helium and hydrogen as fluids. For safety reasons, argon, helium and hydrogen are drained outside. The inlet pressures that will be tested range from 1 to 5 bar, while the outlet pressures range from 1 to 4.9 bar. The outlet pressure is controlled by the pressure difference over the valve, as it is more accurate (i.e. closer over the valve) than to regulate the outlet pressure itself and calculate the pressure difference by subtracting the outlet pressure from the inlet pressure. The difference between controlling the outlet pressure or the pressure difference should be equal to the pressure loss between the valve and the pressure regulator. Normally, this will be negligible. The tested shim heights are 5, 10, 20, 25 and 50 μm. The following method, with constant inlet pressure, will be used during testing:

1. Place test Piezo valve with desired height

2. Set inlet pressure to desired value and set the pressure difference to 0

3. Set pressure difference to the desired value, starting with the smallest value

4. Record pressures and mass flow

5. Go back to step 3 and increase the pressure difference, until the maximum desired pressure difference is reached

6. Repeat steps 2 until 5 for all inlet pressure

7. Repeat steps 1 until 6 for all shim heights

Besides keeping the inlet pressure constant, also the outlet pressure can be kept constant. This will be done using the following method:

1. Place test Piezo valve with desired height

2. Set inlet pressure to the value of the desired outlet pressure, and set the pressure difference to 0

3. Increase the inlet pressure with the desired step

4. Increase the pressure difference with the same step as done in 3

5. Record pressures and mass flow

6. Repeat steps 3 until 5 for all inlet pressures

7. Repeat steps 2 until 6 for all outlet pressures

8. Repeat steps 1 until 7 for all shim heights

For the case that an atmospheric outlet pressure is desired, the second stand alone valve (number 5) is removed from the setup to take away its effect on the flow. The pressure difference over the valve is then only measured, and not used to regulate the outlet pressure.

6 Improving the Model

In this section the measurement data is compared to the model. Only a part of the measurement data is presented here, but in appendix E all data is shown, in combination with the uncorrected model. It will be tried to improve the model empirically using the implemented fudge factors F_1 and F_2. First of all, only the measurement data of air will be used, such that the influence of the height and the inlet pressure can be observed. After that, the resulting factors are applied to the other fluids. If required and possible, the factors will be corrected for the fluid properties with respect to the properties of air.

6.1 Air

In figures 6.1 and 6.2, the results of the measurements and the results of the uncorrected model are shown for air with various fixed inlet pressures and a shim height of 5 μm and 10 μm, respectively. When comparing the model to the data, it is observed that the behaviour of $\dot{m}$ with ΔP is quite similar (i.e. the shape of the graphs are very comparable). The only real exceptions to this are seen for inlet pressures of $P_{in} = 4$ bar and $P_{in} = 5$ bar and a height of $h = 10$ μm, where the predicted choking ($\dot{m}$ does not increase with ΔP anymore) is not observed in the data. However, for all cases the predicted mass flow is significantly lower than the measured mass flow. This implies that the factor F_1 should be increased. Since the model is closer to the data for $h = 10$ μm than for $h = 5$ μm, it is proposed to use a factor that is inversely proportional to the height. From figures 6.3 and 6.4, it is seen that the model without corrections tends to overpredict the mass flow through the valve, and that this problem is larger for the larger shim height. It is therefore likely that there exists a height, somewhere between 10 and 20 μm, for which the uncorrected model exactly follows the data. When applying scalings of $F_1 = \frac{12 \cdot 10^{-6}}{h}$ and $F_2 = \left(\frac{12 \cdot 10^{-6}}{h} \right)^{0.4}$ the results as shown in figures 6.5 to 6.8 are obtained. It is now observed that the adapted model follows the data well for low shim heights and low inlet pressures. For larger heights and inlet pressures, the model follows the data well at (very) low pressure drops. For higher pressure drops, the influence of choking is visible in the data as an asymptotic behaviour, but this is not included in the model. Therefore, in this region, the model overpredicts the flow. At even higher pressure drops, where the measured flow is fully choked, the data and the adapted model correspond reasonably well.

It should be noted that it is possible to achieve very similar results by using an effective height (the height used for the calculations in the model) instead of applying height based corrections. The factor F_2, that changes the choking velocity, may then be taken as a constant value. This method, and the results from it, are described in appendix H. Because the height is not measured, and the surface roughness of the membrane is also expected to influence it, it is expected that the height is indeed different from the height of the shim. It is however highly questionable that the real height is equal to the effective height determined in the appendix.

Measurements were also performed with a 50 μm shim, as shown in figure 6.9. It is observed that besides the fact that the model largely overpredicts the mass flow also the behaviour of the mass flow to the pressure drop seems to be different. There seems to be a region where the mass flow is almost linearly related to the pressure drop, and the whole curve appears a bit less smooth than for lower shim heights. Nevertheless, the earlier used scaling has been applied to the model for this height as well, as shown in appendix F. The model gives mass flows that differ a lot from the measurements and hence this scaling is not valid for this shim height. Besides that, it is observed that a linear scaling of the model will never give a good approximation to the measured mass flow for this shim height, as the predicted mass flow increases too much with the pressure drop. It is expected that (a part of) the assumptions made in the derivation of the model are substantially wrong for air and a shim height of $h = 50$ μm. In order to investigate the probability that the flow is orifice-dominated for this type of channel, the measurement data have been plotted together with the mass flow calculated from the K_v-model (which is independent of the channel height), see figure 6.10. Although the K_v-model approximates the mass flow better than the model developed in section 4, especially in choked conditions, it does not offer a very good approximation for the flow at a given pressure drop.

6.2 Argon

In order to investigate the dependence on the medium, other gases than air are tested. As was done for the measurements with air, the inlet pressures were taken constant while the outlet pressure was varied. The results
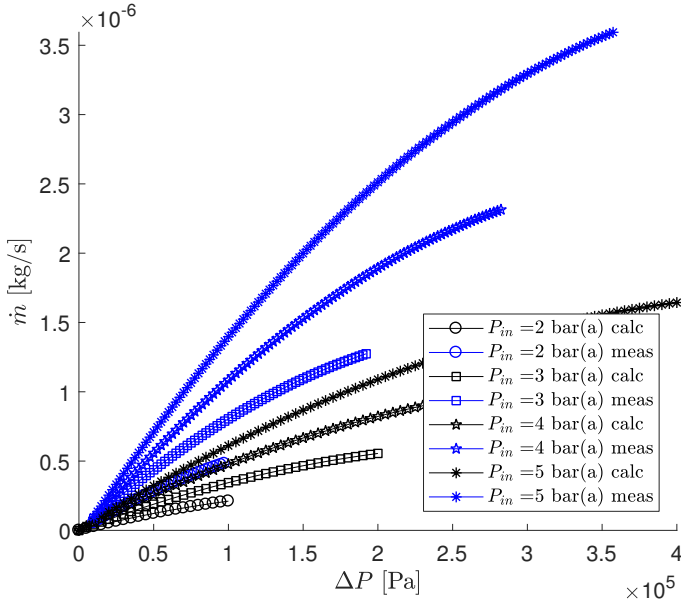
Figure 6.1: Model with $F_1 = F_2 = 1$ and measurement data for air with $h = 5$ μm.
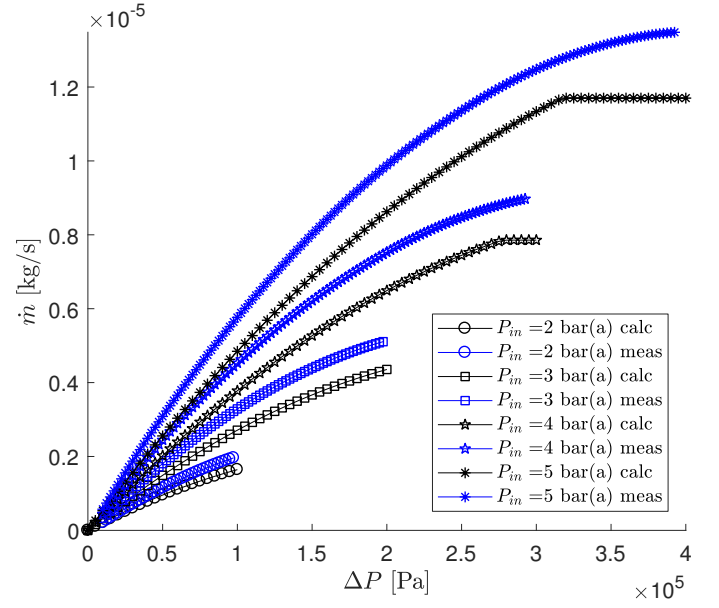
Figure 6.2: Model with $F_1 = F_2 = 1$ and measurement data for air with $h = 10$ μm.
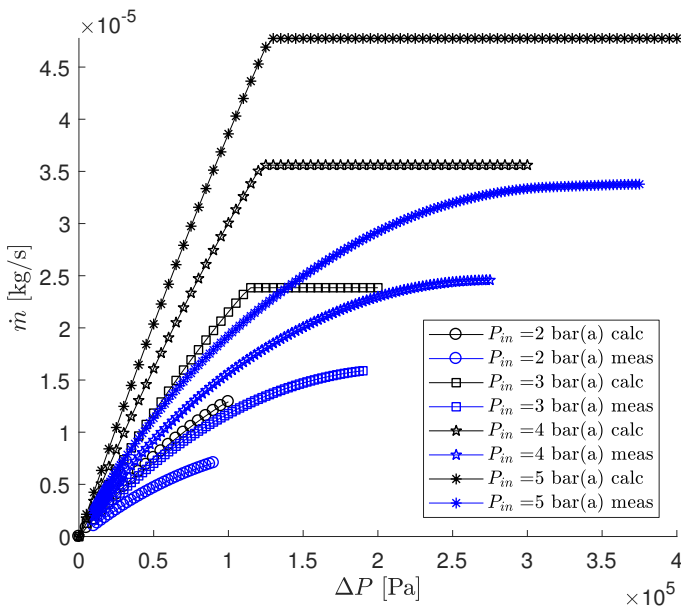
Figure 6.3: Model with $F_1 = F_2 = 1$ and measurement data for air with $h = 20$ μm.
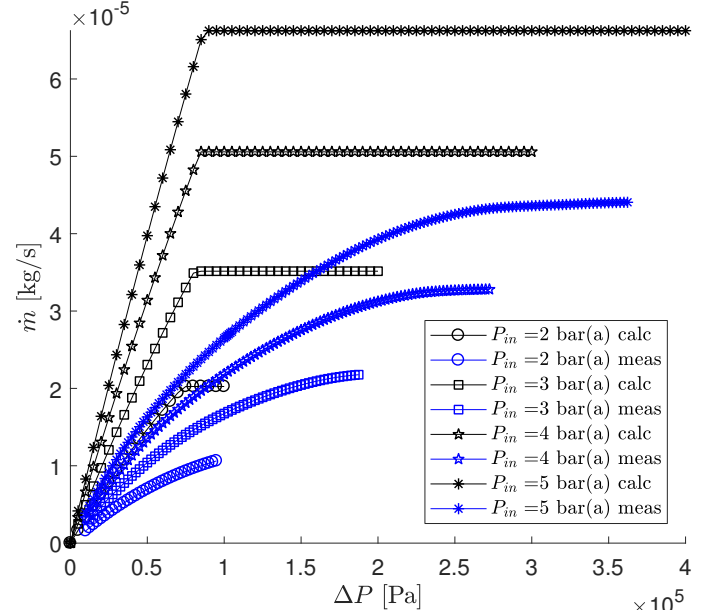
Figure 6.4: Model with $F_1 = F_2 = 1$ and measurement data for air with $h = 25$ μm.

for argon, in combination with the uncorrected model, are given in appendix E. It is seen that the measurements do not correspond to the model. However, for air a height-based correction was found that improved the model. Since the heights are equal to those for air (i.e. the tested devices are exactly the same), it makes sense that this height-based correction should also be applied for argon. This is shown in figures 6.11 and 6.12 for $h = 5$ μm and $h = 25$ μm. The same has been done for the other heights, as can be found in appendix F. It is observed that the model overpredicts the mass flow for all inlet pressures and shim heights. However, the shape of the calculated and measured curves look quite similar, indicating that a linear (gas-specific) scaling might be feasible.

In figures 6.13 and 6.14, the fudge factors were multiplied with 0.5 for $h = 5$ μm and $h = 25$ μm. The same has been done for the other heights, as can be found in appendix G. It is seen that the adapted model now offers a good approximation to the mass flow. However, an explanation for the factor 0.5 needs to be sought.
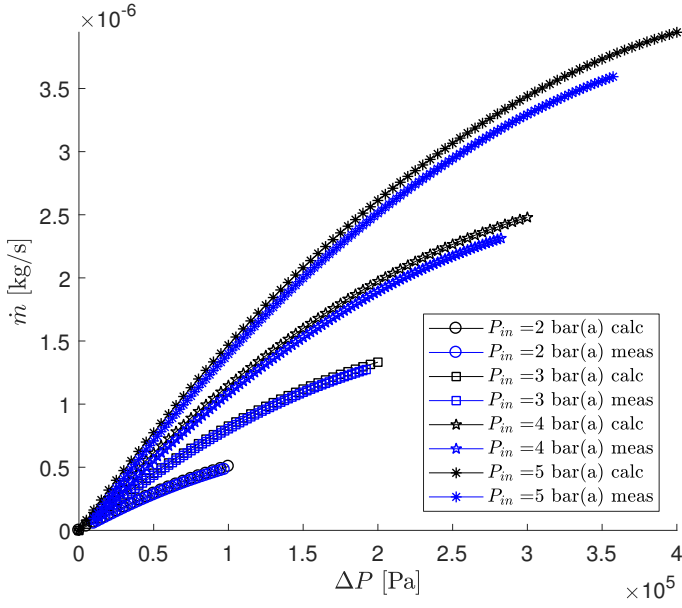
Figure 6.5: Model with $F_1 = \frac{12 \cdot 10^{-6}}{h}$ and $F_2 = \left(\frac{12 \cdot 10^{-6}}{h}\right)^{0.4}$ and data for air with $h = 5$ μm.
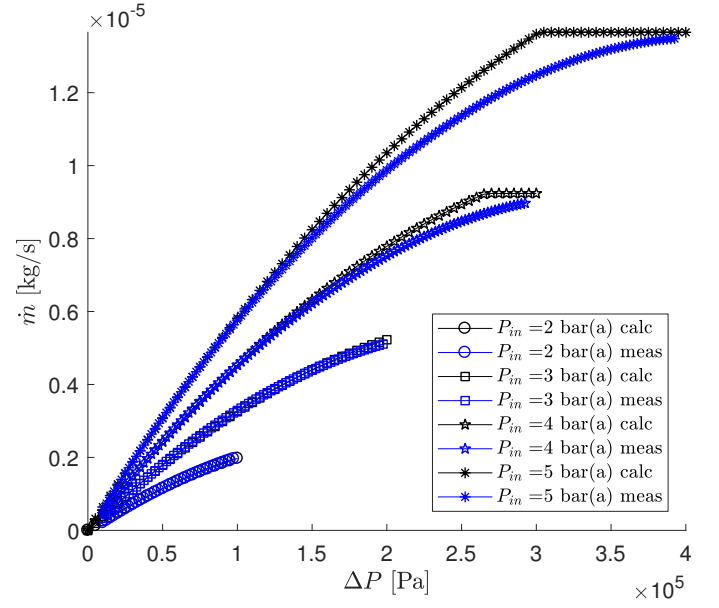
Figure 6.6: Model with $F_1 = \frac{12 \cdot 10^{-6}}{h}$ and $F_2 = \left(\frac{12 \cdot 10^{-6}}{h}\right)^{0.4}$ and data for air with $h = 10$ μm.
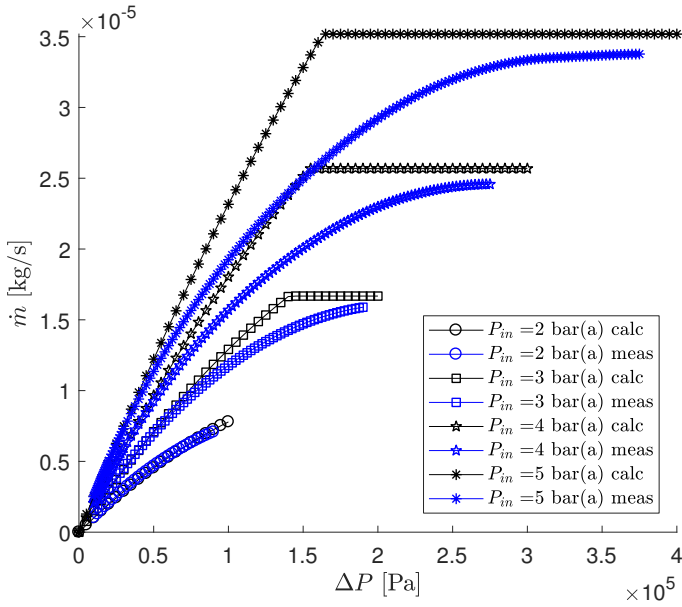
Figure 6.7: Model with $F_1 = \frac{12 \cdot 10^{-6}}{h}$ and $F_2 = \left(\frac{12 \cdot 10^{-6}}{h}\right)^{0.4}$ and data for air with $h = 20$ μm.
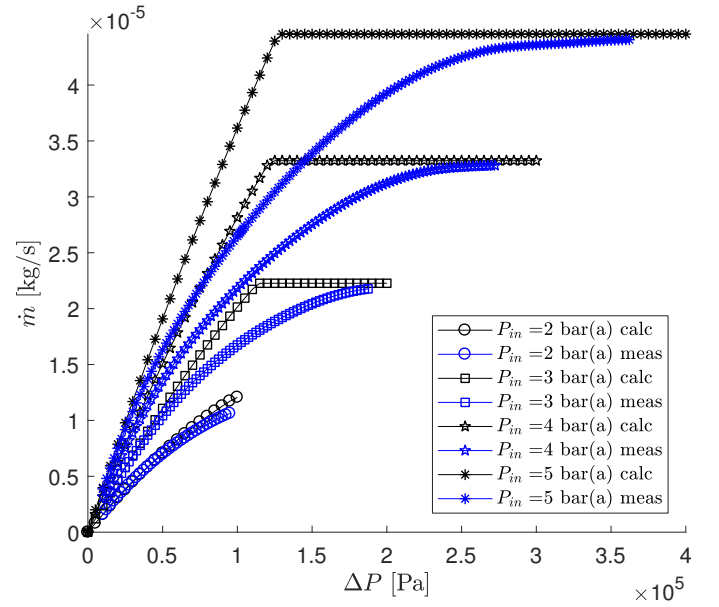
Figure 6.8: Model with $F_1 = \frac{12 \cdot 10^{-6}}{h}$ and $F_2 = \left(\frac{12 \cdot 10^{-6}}{h}\right)^{0.4}$ and data for air with $h = 25$ μm.

6.3   Helium

In order to further investigate the dependence on the medium, helium was tested. As was done for the measurements with air and argon, the inlet pressures were taken constant while the outlet pressure was varied. The results for helium, in combination with the uncorrected model, are given in appendix E. It is seen that the measurements do not correspond to the model. It was, however, stated earlier that the height-based correction should be applied for all measurements, since the height is always the same for the same shim height. This result is shown in figures 6.15 and 6.16 for respectively $h = 5$ and $h = 25$ μm. The same has been done for the other heights, as can be found in appendix F. It is observed that the model underpredicts the mass flow for all inlet pressures and shim heights. However, the shape of the calculated and measured curves look quite similar, indicating that a linear (gas-specific) scaling might be feasible.

Figure 6.9: Model with $F_1 = F_2 = 1$ and measurement data for air with $h = 50\ \mu$m.
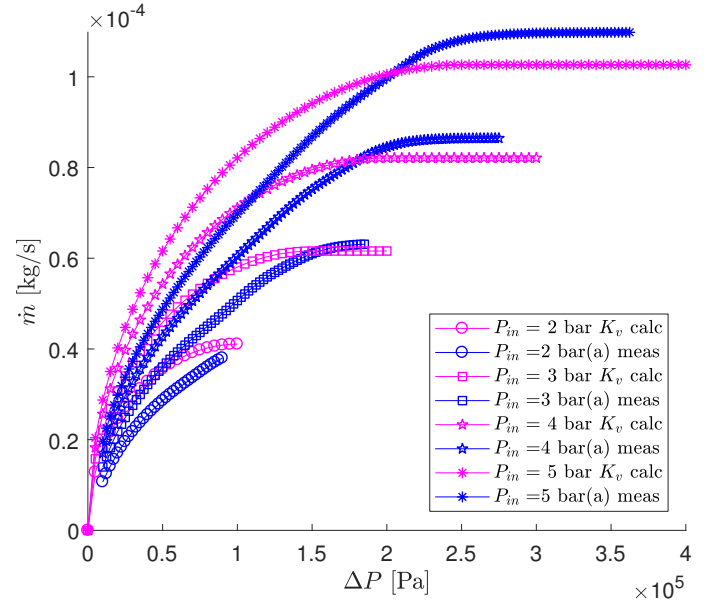
Figure 6.10: K_v-model and measurement data for air and $h = 50\ \mu$m.
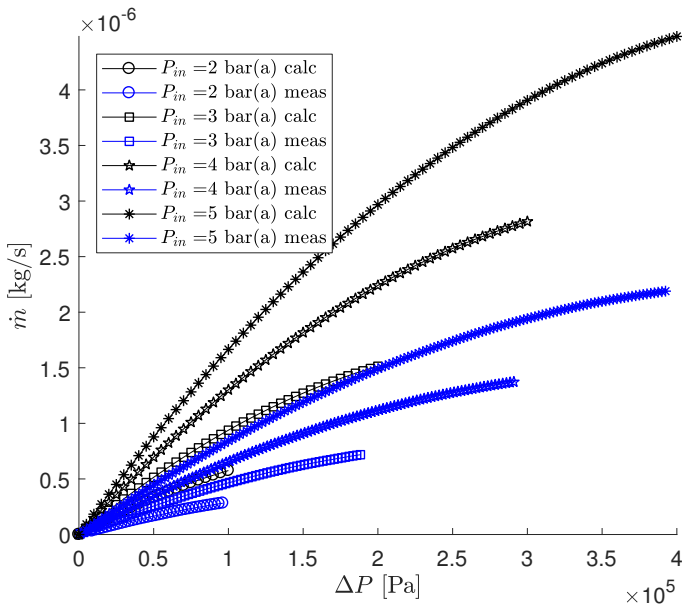
Figure 6.11: Model with $F_1 = \frac{12 \cdot 10^{-6}}{h}$ and $F_2 = \left(\frac{12 \cdot 10^{-6}}{h}\right)^{0.4}$ and data for argon with $h = 5\ \mu$m.
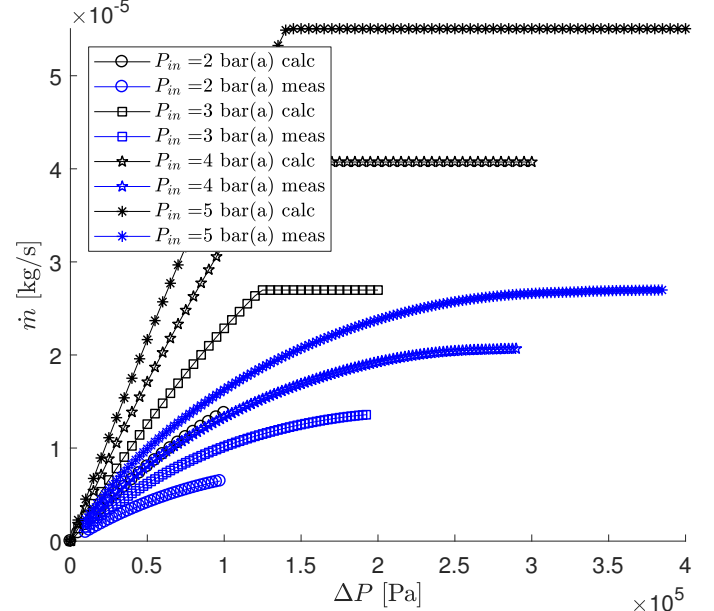
Figure 6.12: Model with $F_1 = \frac{12 \cdot 10^{-6}}{h}$ and $F_2 = \left(\frac{12 \cdot 10^{-6}}{h}\right)^{0.4}$ and data for argon with $h = 25\ \mu$m.

In figures 6.17 and 6.18, the fudge factors were multiplied with 5.35 for $h = 5\ \mu$m and $h = 25\ \mu$m. The same has been done for the other heights, as can be found in appendix G. It is seen that the adapted model now offers a good approximation to the mass flow. For $h = 5\ \mu$m there is an offset between the data and the model, but the data does not go through the point (0,0). It is expected that the flow meter is not calibrated well and the real flow is a bit higher, such that the model is also a good approximation for this height. An explanation for the factor 5.35 needs to be sought, however.

6.4   Hydrogen

A fourth medium, hydrogen, was tested to have more reference data for the gas-specific corrections. As before, the inlet pressures were taken constant while the outlet pressure was varied. The results in combination with the
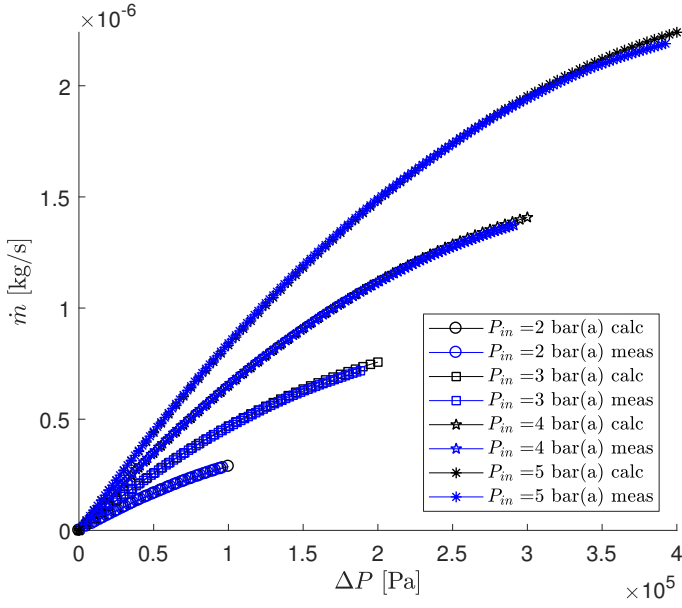
Figure 6.13: Model with $F_1 = \frac{1}{2} \cdot \frac{12 \cdot 10^{-6}}{h}$ and $F_2 = \frac{1}{2} \cdot \left(\frac{12 \cdot 10^{-6}}{h} \right)^{0.4}$ and data for argon with $h = 5 \ \mu$m.
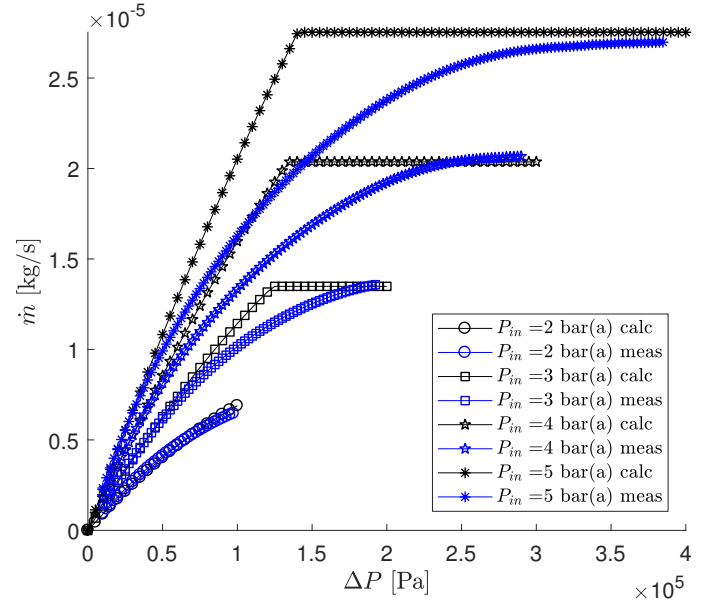
Figure 6.14: Model with $F_1 = \frac{1}{2} \cdot \frac{12 \cdot 10^{-6}}{h}$ and $F_2 = \frac{1}{2} \cdot \left(\frac{12 \cdot 10^{-6}}{h} \right)^{0.4}$ and data for argon with $h = 25 \ \mu$m.
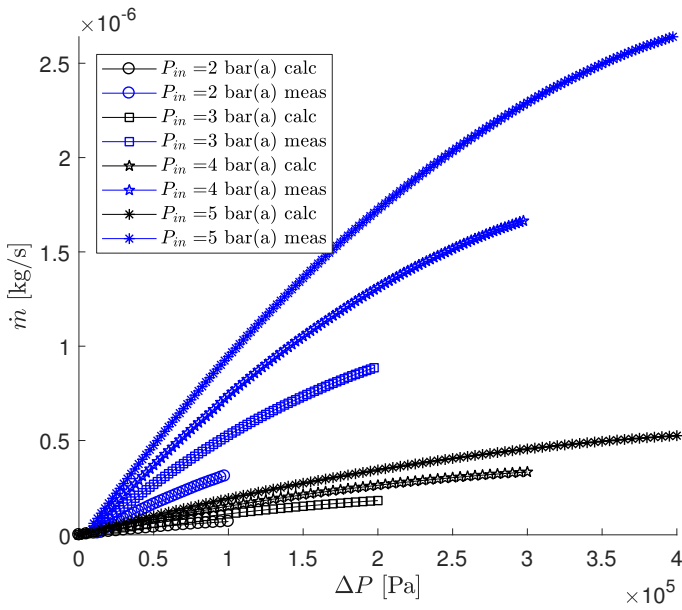
Figure 6.15: Model with $F_1 = \frac{12 \cdot 10^{-6}}{h}$ and $F_2 = \left(\frac{12 \cdot 10^{-6}}{h} \right)^{0.4}$ and data for helium with $h = 5 \ \mu$m.
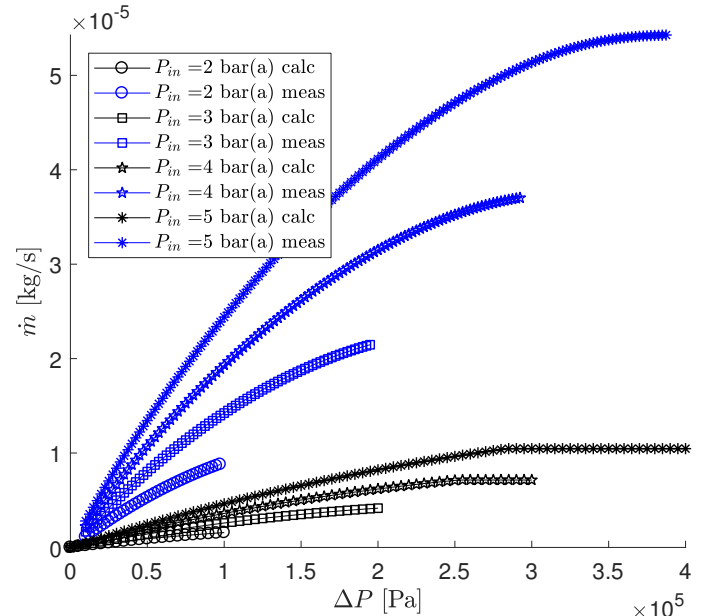
Figure 6.16: Model with $F_1 = \frac{12 \cdot 10^{-6}}{h}$ and $F_2 = \left(\frac{12 \cdot 10^{-6}}{h} \right)^{0.4}$ and data for helium with $h = 25 \ \mu$m.

uncorrected model are given in appendix E. It is seen that the measurements do not correspond to the model. When applying the height-based fudge factors, the results shown in figure 6.19 are obtained for $h = 10 \ \mu$m. The same figures for the other heights can be found in appendix F. It is observed that the model underpredicts the mass flow for all inlet pressures and shim heights. However, the shape of the calculated and measured curves look quite similar, indicating that a linear (gas-specific) scaling might be feasible.

In figure 6.20, the fudge factors were multiplied with 14 for $h = 10 \ \mu$m. The same has been done for the other heights, as shown in appendix G. The adapted model is seen to offer a good approximation to the mass flow. For $h = 5 \ \mu$m there is an offset between the data and the model, but the data does not go through the point (0,0).The flow meter is expected to not be well-calibrated and the real flow will be a bit higher, such that the model offers a good approximation for this height. An explanation for the factor 14 still needs to be found.
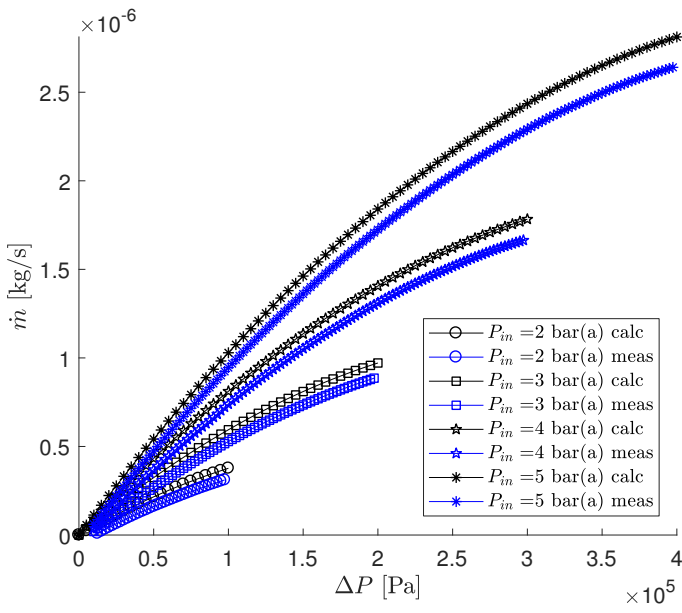
Figure 6.17: Model with $F_1 = 5.35 \cdot \frac{12 \cdot 10^{-6}}{h}$ and $F_2 = 5.35 \cdot \left(\frac{12 \cdot 10^{-6}}{h} \right)^{0.4}$ and data for helium with $h = 5\ \mu$m.
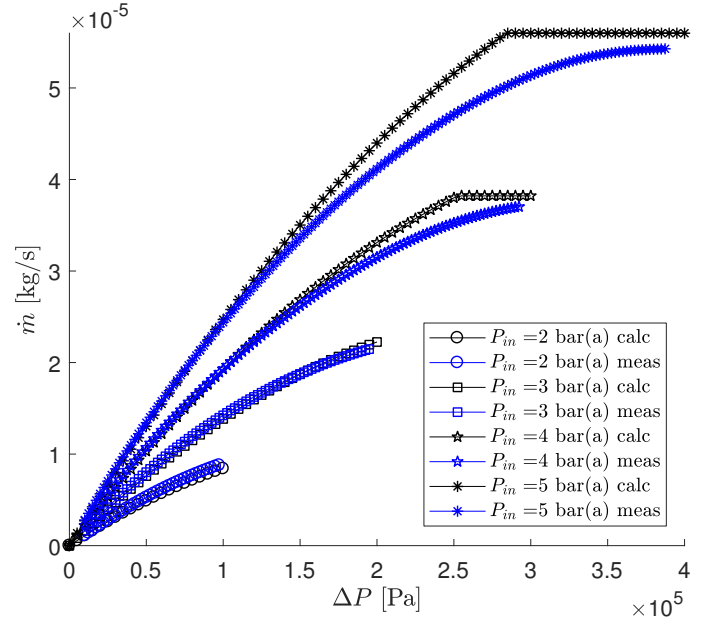
Figure 6.18: Model with $F_1 = 5.35 \cdot \frac{12 \cdot 10^{-6}}{h}$ and $F_2 = 5.35 \cdot \left(\frac{12 \cdot 10^{-6}}{h} \right)^{0.4}$ and data for helium with $h = 25\ \mu$m.
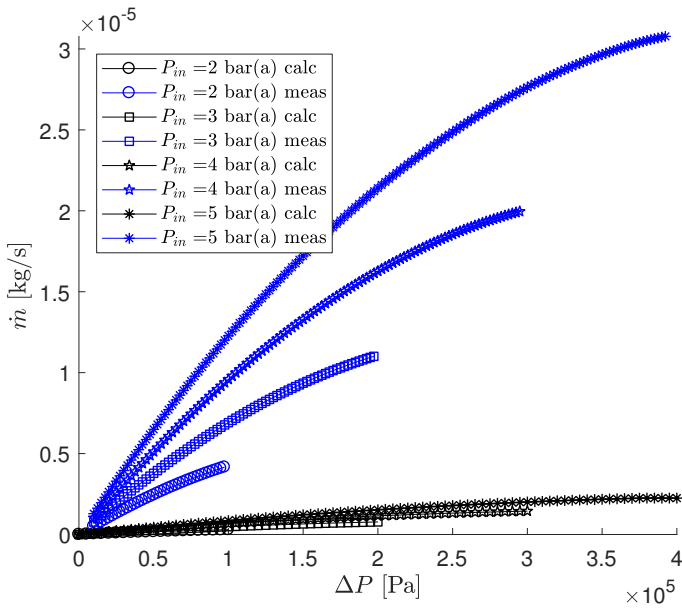
Figure 6.19: Model with $F_1 = \frac{12 \cdot 10^{-6}}{h}$ and $F_2 = \left(\frac{12 \cdot 10^{-6}}{h} \right)^{0.4}$ and data for hydrogen with $h = 10\ \mu$m.
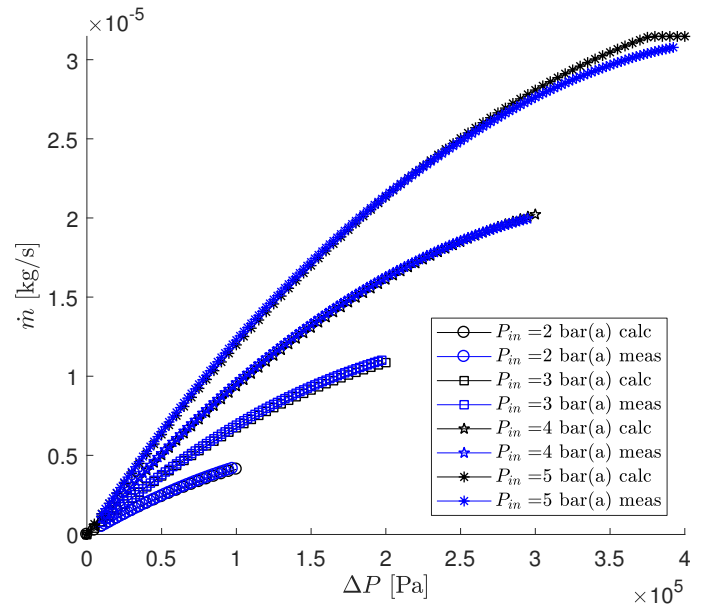
Figure 6.20: Model with $F_1 = 14 \cdot \frac{12 \cdot 10^{-6}}{h}$ and $F_2 = 14 \cdot \left(\frac{12 \cdot 10^{-6}}{h} \right)^{0.4}$ and data for hydrogen with $h = 10\ \mu$m.

6.5   Gas-Dependent Corrections

It was found that the global behaviour of the mass flow to the pressure drop (with constant inlet pressure) could be described with the model, but that some fudge factors were required to obtain the correct values. Besides a height-based correction, that may be explained by the fact that the actual throughflow height is different from the shim height, there was also need for a different correction per gas. In table 6.1, the desired factors per gas and some (possibly) important gas specifics are given.

A physically satisfying expression for the gas-specific factors was not found. Testing more gases, and testing mixtures of gases, may help to identify the important gas parameters in a next study.

It should also be noted that, since the pressure drop cannot be measured only over the channel, there may be

Table 6.1: Required gas-specific factors and gas specifics. Viscosity is calculated at $T = 293$ K.

Gas	Required Factor [-]	$\gamma = \frac{c_P}{c_v}$ [-]	R [J/(kgK)]	μ [$\cdot 10^{-5}$ Pa·s]
Argon	0.5	1.667	208	2.2319
Air	1.0	1.4	286.9	1.8362
Helium	5.35	1.667	2077	1.9991
Hydrogen	14.0	1.405	4124	0.8742

more effects that influence the flow. In appendix I, the pressure loss in the pipes to and from the microchannel was estimated. It appeared that this pressure drop was negligibly small compared to the pressure drop in the microchannel. Furthermore, the influence of the Joule-Thomson effect was investigated in appendix J, but found to be negligible. The sensitivity of the model to the temperature and to the orifice diameter is discussed in appendix K. The influence of the temperature is relatively small. The influence of the orifice diameter is however large for choked conditions. It is assumed that this is a numerical effect of the model, rather than a realistic effect. The implementation of choked flow in the model may therefore be improved.

Besides the mentioned effects, there may also be influences of for example the development of the flow in the microchannel or the change in flow direction to flow through the orifice. Also the assumption of axisymmetric flow may have a significant effect. Non-axisymmetric flow will however result in far more complex equations. However, it may be useful to investigate if better results can be obtained by modeling the geometry as a duct, as described in for example [15, 19, 22]. For current use of the model, it is recommended to do a calibration measurement for a gas such that the fudge factor can be determined. With this factor, the flow can be calculated for other shim heights and inlet pressures with the same gas to an acceptable accuracy.

7 Flow Direction

In section 4.4 it was mentioned that reversing the flow direction may give a higher flow rate when the flow becomes choked. In order to validate this statement, measurements were done. It is remarked that the flow in non-choked conditions is expected to remain approximately equal when the flow is dominated by the channel, as the channel is not changed by reversing the flow direction.

It should be noted that inward flow is regarded (and sometimes described) as the common direction, and that terms like "reversed flow" indicate outward flow. Only a part of the results will be shown here. For all results, the reader is referred to appendix L.

7.1 Air

At first, the measurements for air will be discussed. The measurements were performed similarly as the measurements for inward flow, so the inlet pressure was taken constant and the outlet pressure was varied. As was seen before, the flow is not significantly influenced by choking for $h = 5$ μm. It was expected that for these situations the flow direction would not influence the mass flow. In figure 7.1, it is seen that this is indeed the case. The data curves for inward and outward flow are almost on top of each other. In figure 7.2 it is seen that this does not hold for $h = 20$ μm. Higher pressure drops, combined with a higher inlet pressure, increase the influence of the flow direction. It is seen that the outward flow follows the model to higher values for $\frac{\Delta P}{P_{in}}$, corresponding to the hypothesis that the asymptotic behaviour is caused by choking. Moreover, it is seen that the maximum flow through the channel for a constant inlet pressure is significantly higher when the flow is reversed, which corresponds to the hypothesis that choking starts later (i.e. at a higher pressure drop) for the reversed flow direction. However, it is not as high as predicted by the model. Presumably a different (height-based) scaling is required for the choke speed. This factor should then also account for the non-axisymmetric outflow. In figure 7.3 the results for $h = 50$ μm are shown. It was already seen that the model does not give realistic values for the mass flow for this height. However, it is interesting to see that the inward and outward flow compare different to each other than at $h = 20$ μm. The outward flow results in a (much) higher mass flow already at low pressure drops, which supports the assumption that the flow is no longer dominated by the through-flow height of the channel. The orifice may be dominant, such that the mass flow for outward flow is larger for low pressure drops. The "orifice" (hole that now functions as orifice) at the side of the disk (used for outward flow) is larger than the orifice at the centre (used for inward flow), such that the flow increases more rapidly with $\frac{\Delta P}{P_{in}}$. However, the difference in the maximum mass flow through the channel seems to be small, especially for high inlet pressures. It is assumed that the inlet gap limits the flow when it is small compared to the orifice. It is assumed that this causes the small difference in maximum flow.

7.2 Argon

Measurements were done with different gases in order to see whether the effect of reversing the flow is gas-dependent. In this section the results for argon are discussed. The results for $h = 20$ μm and $h = 50$ μm are shown in figures 7.4 and 7.5, respectively. The results with other shim heights are given in appendix L. It is seen that the results are very comparable to those of air: the expected delayed choking is seen for all shim heights, except for 50 μm, where the relation of the mass flow with $\frac{\Delta P}{P_{in}}$ changes with the flow direction.

7.3 Helium

To further see whether the effect of reversing the flow is gas-dependent, also helium was used as medium. The results for $h = 20$ μm and $h = 50$ μm are shown in figures 7.6 and 7.7, respectively. The results with other shim heights are given in appendix L. Since the choking is observed at larger heights and inlet pressures than for air and argon, the effect of reversing the flow has also shifted. The difference for $h = 20$ μm is relatively small compared to air and argon, although the general behaviour is similar. For $h = 50$ μm, however, this is not the case. The maximum flow is significantly increased when the flow is reversed, whereas the effect for this height was relatively small for air and argon. Both directions also start on top of each other, which was not seen for air and argon. In a way, the situation for $h = 50$ μm with helium compares to the situation for $h = 25$ μm with air or argon.
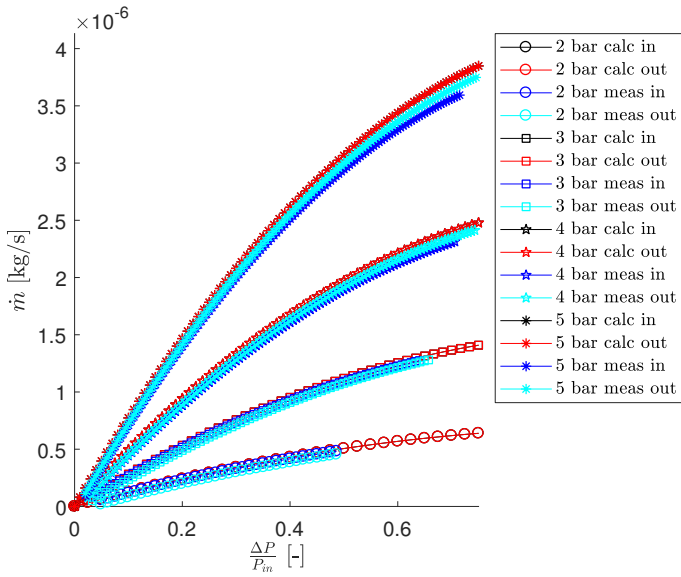
Figure 7.1: Calculated and measured mass flows for inward (blue curves) and outward (cyan curves) flow for $h = 5$ μm. Air was used at various constant inlet pressures, and the corrected model was applied.
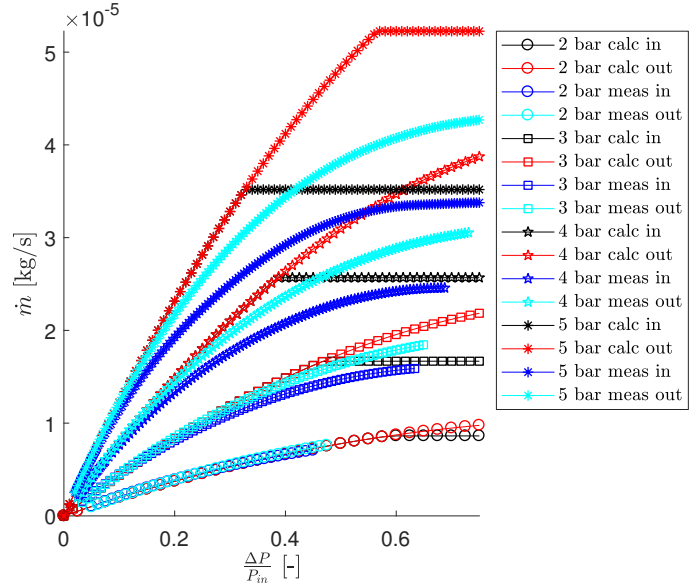
Figure 7.2: Calculated and measured mass flows for inward (blue curves) and outward (cyan curves) flow for $h = 20$ μm. Air was used at various constant inlet pressures, and the corrected model was applied.
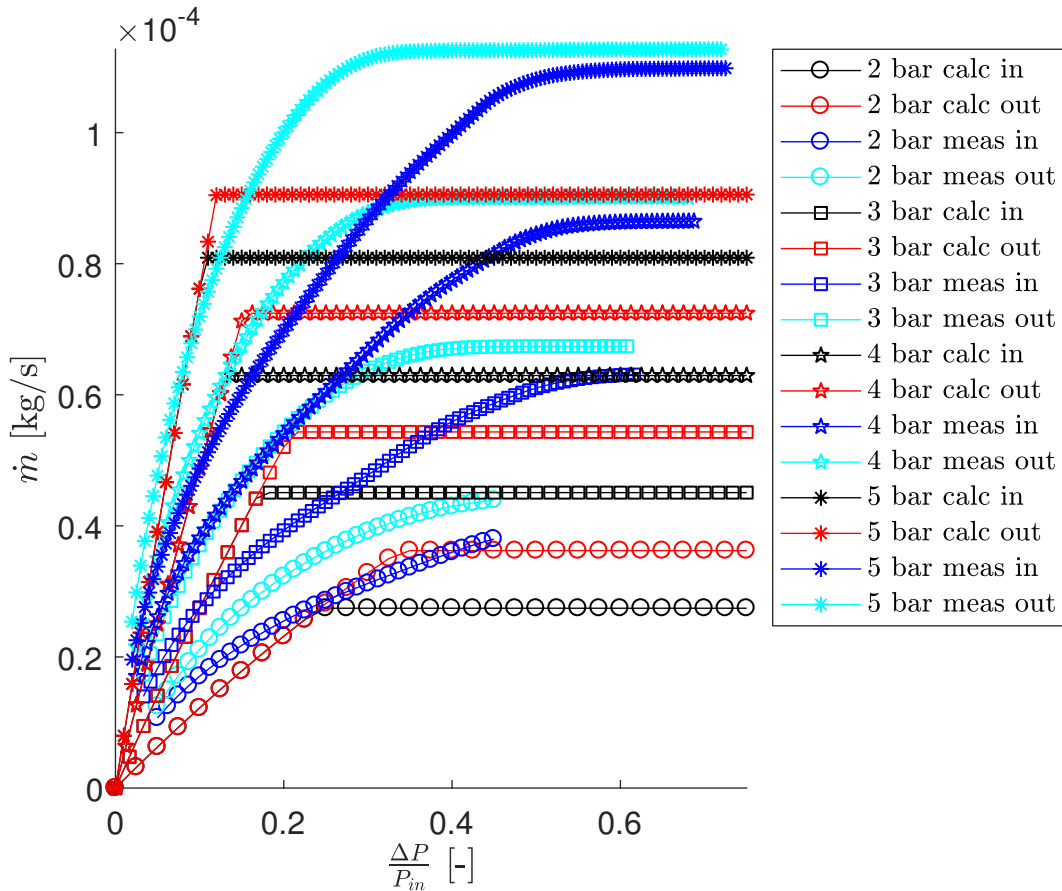
Figure 7.3: Calculated and measured mass flows for inward (blue curves) and outward (cyan curves) flow for $h = 50$ μm. Air was used at various constant inlet pressures, and the corrected model was applied.
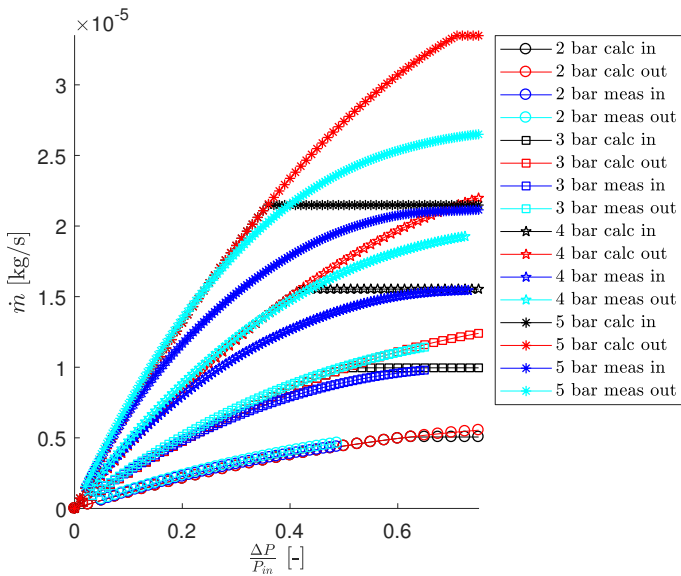
Figure 7.4: Calculated and measured mass flows for inward (blue curves) and outward (cyan curves) flow for $h = 20$ μm. Argon was used at various constant inlet pressures, and the corrected model was applied.
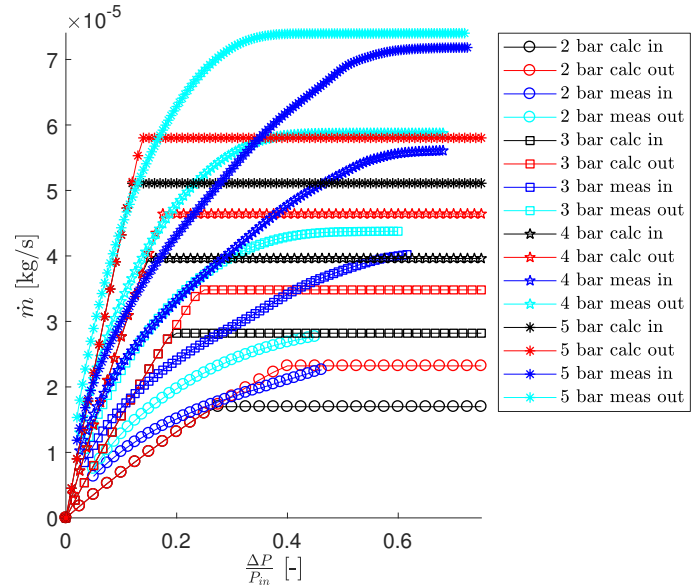
Figure 7.5: Calculated and measured mass flows for inward (blue curves) and outward (cyan curves) flow for $h = 50$ μm. Argon was used at various constant inlet pressures, and the corrected model was applied.
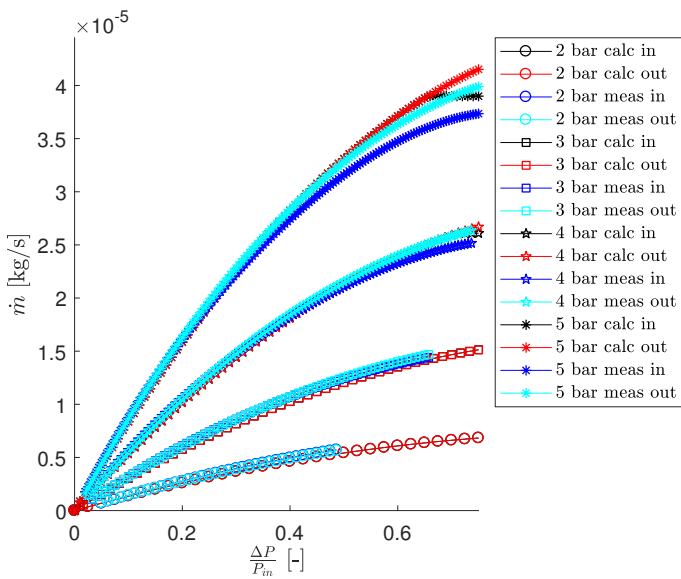
Figure 7.6: Calculated and measured mass flows for inward (blue curves) and outward (cyan curves) flow for $h = 20$ μm. Helium was used at various constant inlet pressures, and the corrected model was applied.
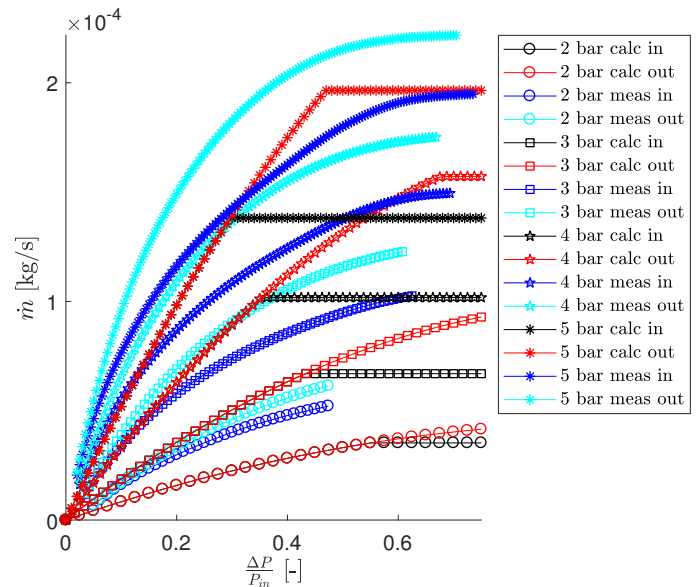
Figure 7.7: Calculated and measured mass flows for inward (blue curves) and outward (cyan curves) flow for $h = 50$ μm. Helium was used at various constant inlet pressures, and the corrected model was applied.

7.4   Using Reversed Flow

It was seen that the reversion of the flow direction may give a higher flow. This is especially the case for shim heights upto 25 μm where, for inwards flow, the applied pressure drop is higher than the critical pressure drop belonging to a certain inlet pressure. In these situations, it may be useful to reverse the flow direction when it is found that the capacity of the valve is insufficient for the process. When applying a pressure drop that is lower than the critical pressure drop, the effect is mostly small and the use is negligible.

8 Using the Model

When the model is used to select the required shim height for reaching a flow, it is important that this height is indeed sufficient to reach it. The valve can be calibrated by changing the initial actuator height, but a too thin shim will affect the leak-tightness of the valve, while a too thick shim may affect the controller performance. So, for a selected height, the calculated flow should be as close as possible to, but always below, the actual flow.

It is proposed to implement a safety margin in the model as a safety factor for the mass flow. In this way, the model should become conservative, i.e. the calculated mass flow should always be too low. In figures G.1 until G.20 the deviation between model and data was seen to become more severe when choking is calculated to start at lower values of $\frac{\Delta P}{P_{in}}$. A part of the safety factor will therefore be related to the calculated critical pressure. Besides this part, a constant factor is included, which is dominant for low shim heights or low inlet pressures. The following iterative procedure is proposed for selecting a shim height h_{select} for given operating conditions:

1. Guess a shim height h_{guess}

2. Calculate the critical outlet pressure $P_{out,c}$ from (4.42)

3. Calculate the predicted mass flow $\dot{m}$ from (4.44) and (4.45).

4. Calculate the safe mass flow $\dot{m}_{\text{safe}}$ as:

$$\dot{m}_{\text{safe}} = S_1 \cdot S_2(P_{in}, P_{out,c}) \cdot \dot{m} \tag{8.1}$$

   where $S_1 = 0.9$ and $S_2(P_{in}, P_{out,c}) = \sqrt[4]{\frac{P_{in} - P_{out,c}}{P_{in}}}$ are the safety factors.

5. Compare the required mass flow $\dot{m}_{\text{req}}$ to the safe mass flow $\dot{m}_{\text{safe}}$. Perform 1 of the three actions below:

   a. $\dot{m}_{\text{req}} > \dot{m}_{\text{safe}}$: $h_{\text{low}} = h_{\text{guess}}$.
   b. $\dot{m}_{\text{req}} < \dot{m}_{\text{safe}}$: $h_{\text{select}} = h_{\text{guess}}$.
   c. $\dot{m}_{\text{req}} = \dot{m}_{\text{safe}}$: $h_{\text{select}} = h_{\text{guess}}$ and end the selecting procedure.

   When both h_{low} and h_{select} have been defined, the most optimal shim height was found and the selecting procedure is finished. When only h_{low} has been defined, go back to step 1 for the shim that is one level higher (if this is possible, otherwise no suitable height can be found). When only h_{select} has been defined, go back to step 1 for the shim that is one level lower (if this is possible, otherwise this is the most suitable height).

This procedure guarantees that the most suitable shim height is found when it exists. In appendix M the safe model is compared to the measurement data. It is observed that this model is indeed always below the measurement data. Furthermore it is seen that the safety margin is in some cases relatively high. When the transition to choked flow is modeled more accurately, this safety margin can be decreased (by changing S_2). Currently, the critical point prohibits the use of a smaller safety margin (i.e. a higher number S_2).

$$F_2 c = \frac{F_1 P_{in} h^2 \left[\left(\frac{P_{out,c}}{P_{in}} \right)^2 - 1 + 24 C_1 \text{Kn}_{in} \left(\frac{P_{out,c}}{P_{in}} - 1 \right) \right] \left[\frac{1}{6} + \frac{2 C_1 \text{Kn}_{in} P_{in}}{P_{out,c}} \right]}{2 \mu d \ln\left(\frac{d}{2L}\right) \left(\frac{P_{out,c}}{P_{in}} + 12 C_1 \text{Kn}_{in} \right)} \tag{4.42 revisited}$$

$$\bar{u}_r(r) = \begin{cases} \dfrac{-F_1 P_{in} h^2 \left[\left(\frac{P_{out}}{P_{in}} \right)^2 + 24 C_1 \text{Kn}_{in} \left(\frac{P_{out}}{P_{in}} - 1 \right) - 1 \right] \left[\frac{1}{6} + \frac{2 C_1 \text{Kn}_{in} P_{in}}{P(r)} \right]}{4 \mu r \ln\left(\frac{d}{2L}\right) \sqrt{(1 + 12 C_1 \text{Kn}_{in})^2 + \left(\left(\frac{P_{out}}{P_{in}} \right)^2 + 24 C_1 \text{Kn}_{in} \left(\frac{P_{out}}{P_{in}} - 1 \right) - 1 \right) \frac{\ln\left(\frac{r}{L}\right)}{\ln\left(\frac{d}{2L}\right)}}}, & P_{out} \geq P_{out,c} \\[4ex] \dfrac{-F_1 P_{in} h^2 \left[\left(\frac{P_{out,c}}{P_{in}} \right)^2 + 24 C_1 \text{Kn}_{in} \left(\frac{P_{out,c}}{P_{in}} - 1 \right) - 1 \right] \left[\frac{1}{6} + \frac{2 C_1 \text{Kn}_{in} P_{in}}{P(r)} \right]}{4 \mu r \ln\left(\frac{d}{2L}\right) \sqrt{(1 + 12 C_1 \text{Kn}_{in})^2 + \left(\left(\frac{P_{out,c}}{P_{in}} \right)^2 + 24 C_1 \text{Kn}_{in} \left(\frac{P_{out,c}}{P_{in}} - 1 \right) - 1 \right) \frac{\ln\left(\frac{r}{L}\right)}{\ln\left(\frac{d}{2L}\right)}}}, & P_{out} < P_{out,c} \end{cases}$$

$$\text{(4.44 revisited)}$$

$$\dot{m} = 2\pi L h \frac{P_{in}}{RT} \bar{u}_r(r = L) \tag{4.45 revisited}$$

9   Conclusion

This report focused on the development of a model to determine the capacity of the microfluidic Piezo valve. The main question of this study was formulated as:

How does the gas mass flow rate in a microfluidic valve depend on the geometrical properties, the type of gas and the operating conditions?

It was found that the K_v-model, as used within BHT to characterise the capacity of valves, did not correspond to the measurement data for the microfluidic Piezo valve. It appeared that the relation between the pressure drop and the flow was different and that the throughflow height, which was proven to be an important parameter for the flow capacity, is not taken into account in the model. Several correction methods were tested in earlier studies, but these did not give the desired results.

Therefore, a new theoretical model was derived from the Navier-Stokes equations with a slip condition at the boundary. The geometry of the channel was simplified to an axisymmetric disk, while the flow was assumed to be steady and isothermal and the gases were assumed to be ideal. Using a dimensional analysis, the less important terms in the equation were identified and neglected. The resulting simplified equations were solved algebraically. In order to account for choked flow, the critical regions were identified and included in the model. Two fudge factors were included to allow empirical corrections for effects that were not taken into account.

Measurements were conducted to verify the model, which showed the need for a height-based correction and a correction per gas to approximate the measured gas flow with the model. An explanation for the gas-specific correction was not found, leaving the need for a calibration measurement per gas. Furthermore, deviations between the model and the data existed due to the influence of choking. The flow through the valve with a shim height of 50 μm was found to be characterised by a different relation between pressure drop and mass flow, and hence the model was not valid for this height.

Finally, a safety factor was introduced to ensure that desired flows can always be reached by a shim height (upto 25 μm) that is selected with the model. This is important for BHT when the model is used to select the valve for a customer. The safety margin was shown to be relatively large for certain situations due to (the transition to) choked flow.

Resuming to the main question, it is concluded that a relation between the gas mass flow rate in a microfluidic valve on the one hand and the geometrical properties and the operating conditions on the other hand was found for shim heights of 25 μm and less. The influence of the type of gas cannot be fully predicted and needs to be (partly) accounted for by a calibration measurement. Further research on choked flow and the gas dependency is required to optimise the model.

10 Recommendations

In this study a model was developed that characterised the flow in the BHT Piezo valve. It has, however, several shortcomings that should be solved by further research. In this section recommendations are given that offer a guideline for further research. They are subdivided into different categories.

First of all, the empirically determined correction factors need to be explained. In order to do this, it is recommended to:

- Investigate how the actual throughflow height is related to the shim height.

- Investigate the influence of non-axisymmetric flow.

- Perform measurements with more gases and study how the gas-specific correction factor depends on the gas properties.

- Study how the gas-specific correction of a mixture of gases relates to the gas-specific corrections of the separate gases.

- Quantify the entrance and exit effects of the flow to and from the disk.

Secondly, the model needs to be verified on some untested effects. Therefore, it is recommended to:

- Measure the influence of the orifice diameter on the mass flow.

- Measure the influence of the temperature of the medium on the mass flow.

- Compare the flow through the test Piezo valve to the flow through the actual Piezo valve.

Lastly, it is desired to expand the validity of the model to different flow regimes. It is therefore recommended to:

- Research the exact cause of choked flow.

- Investigate the transition to choked flow.

- Study the flow regime of the valve using larger shim heights.

Bibliography

[1] Bronkhorst High-Tech B.V., "Company profile," 2017, [Accessed 24-10-2017]. [Online]. Available: https://www.bronkhorst.com/en/about_us/company_profile/

[2] ——, "Thermal mass flow measurement," 2017, [Accessed 24-10-2017]. [Online]. Available: https://www.bronkhorst.com/en/products/theory/thermal_mass_flow_measurement/

[3] ——, "Coriolis mass flow measuring principle," 2017, [Accessed 24-10-2017]. [Online]. Available: https://www.bronkhorst.com/en/products/theory/coriolis_mass_flow_measuring_principle/

[4] R. Van 't Rood and N. Kupper, "Valve calculation methods," Bronkhorst High-Tech, Tech. Rep., 2017.

[5] J. Van De Geest, "Elastomeric sealed piezo valve," Bronkhorst High-Tech, Tech. Rep., 2015.

[6] K. Reinders, "Karakterisatie lage debietventielen voor vloeistoffen," Bronkhorst B.V., Tech. Rep., 2015.

[7] J. Korenblik, "Karakterisatie van lage debietventielen voor gassen," Bronkhorst B.V., Tech. Rep., 2017.

[8] Swagelok, "Valve sizing," Swagelok Company, Tech. Rep., 2007.

[9] H. Boysen, "k_v: what, why, how, whence?" Danfoss A/S, [Technical paper], 2011, retrieved from: http://heating.danfoss.com/PCMPDF/VFHBG202_kv.pdf.

[10] Bronkhorst High-Tech B.V., "Volume flow versus mass flow," 2017, [Accessed 27-11-2017]. [Online]. Available: https://www.bronkhorst.com/en/products/theory/volume_flow_versus_mass_flow/

[11] Wikipedia, "Piezoelectricity," 2017, [Accessed 11-10-2017]. [Online]. Available: https://en.wikipedia.org/w/index.php?title=Piezoelectricity&oldid=804659251

[12] S. Klein Hesselink, "NEN-IEC 60534 directive scope industrial process control valves," Bronkhorst High-Tech, Tech. Rep., 2014.

[13] ISA, "Flow equations for sizing control valves," Standard, 2007, iSA-75.01.01-2007 (60534-2-1 Mod).

[14] Z. Duan and Y. Muzychka, "Slip flow in non-circular microchannels," *Microfluidics and Nanofluidics*, vol. 3, no. 4, pp. 473–484, 2007.

[15] N. Dongari, A. Agrawal, and A. Agrawal, "Analytical solution of gaseous slip flow in long microchannels," *International Journal of Heat and Mass Transfer*, vol. 50, no. 17, pp. 3411 – 3421, 2007.

[16] S. Jennings, "The mean free path in air," *Journal of Aerosol Science*, vol. 19, no. 2, pp. 159 – 166, 1988.

[17] N. Dongari, A. Sharma, and F. Durst, "Pressure-driven diffusive gas flows in micro-channels: from the knudsen to the continuum regimes," *Microfluidics and Nanofluidics*, vol. 6, no. 5, pp. 679–692, 2009.

[18] G. A. Radtke, N. G. Hadjiconstantinou, S. Takata, and K. Aoki, "On the second-order temperature jump coefficient of a dilute gas," *Journal of Fluid Mechanics*, vol. 707, p. 331341, 2012.

[19] E. B. Arkilic, M. A. Schmidt, and K. S. Breuer, "Gaseous slip flow in long microchannels," *Journal of Microelectromechanical Systems*, vol. 6, no. 2, pp. 167–178, 1997.

[20] A. Beskok and G. E. Karniadakis, "Report: A model for flows in channels, pipes, and ducts at micro and nano scales," *Microscale Thermophysical Engineering*, vol. 3, no. 1, pp. 43–77, 1999.

[21] B. Lautrup, *Physics of Continuous Matter: Exotic and Everyday Phenomena in the Macroscopic World*, 2nd ed.   Taylor & Francis, 2009.

[22] X. Zhu, Q. Liao, and M. D. Xin, "Gas flow in microchannel of arbitrary shape in slip flow regime," *Nanoscale and Microscale Thermophysical Engineering*, vol. 10, no. 1, pp. 41–54, 2006.

[23] H. P. Kavehpour, M. Faghri, and Y. Asako, "Effects of compressibility and rarefaction on gaseous flows in microchannels," *Numerical Heat Transfer, Part A: Applications*, vol. 32, no. 7, pp. 677–696, 1997.

[24] Wikipedia, "Choked flow," 2017, [Accessed 5-October-2017]. [Online]. Available: https://en.wikipedia.org/w/index.php?title=Choked_flow&oldid=802493352

[25] T. Walters, "Gas-flow calculations: Don't choke," *Chemical Engineering*, pp. 70–76, Jan. 2000.

[26] Wikipedia, "Viscosity," 2017, [Accessed 13-10-2017]. [Online]. Available: https://en.wikipedia.org/w/index.php?title=Viscosity&oldid=804075218

[27] W. Sutherland, "LII. The viscosity of gases and molecular force," *Philosophical Magazine*, vol. 36, no. 223, pp. 507–531, 1893.

[28] Wikipedia, "Sutherland-model," 2016, [Accessed 13-10-2017]. [Online]. Available: https://de.wikipedia.org/w/index.php?title=Sutherland-Modell&oldid=159343192

[29] ——, "Darcy-weisbach equation," 2017, [Accessed 07-12-2017]. [Online]. Available: https://en.wikipedia.org/w/index.php?title=Darcy%E2%80%93Weisbach_equation&oldid=810445358

[30] Ohio Medical Corporation, "Pressure drop in air piping systems," Tech. Rep., 2006.

[31] "Moody friction factor graph," 2004, [Accessed 07-12-2017]. [Online]. Available: https://faculty-web.msoe.edu/tritt/be382/MoodyChart.html

[32] S. Jayanti, "Bends, flow and pressure drop in," *Thermopedia*, 2011.

[33] Wikipedia, "Joule-thomson effect," 2017, [Accessed 08-12-2017]. [Online]. Available: https://en.wikipedia.org/w/index.php?title=Joule%E2%80%93Thomson_effect&oldid=811060211

[34] The Engineering Toolbox, "Air properties," n.d., [Accessed on 08-12-2017]. [Online]. Available: https://www.engineeringtoolbox.com/air-properties-d_156.html

Appendices

A   Derivation K_v-value for Liquids

Given is the steady, 1D Navier-Stokes equation:

$$\rho\left(u\frac{\partial u}{\partial x}\right) = \rho g_x - \frac{\partial P}{\partial x} + \frac{4}{3}\frac{\partial}{\partial x}\left(\mu\frac{\partial u}{\partial x}\right) \tag{A.1}$$

Neglecting gravity and assuming the fluid to be incompressible gives:

$$\frac{\partial}{\partial x}\left(\frac{1}{2}\rho u^2 + P + \frac{4}{3}\mu\frac{\partial u}{\partial x}\right) = 0$$

Assuming the fluid to be inviscid and integrating from inlet to outlet gives:

$$\frac{1}{2}\rho_2 u_2^2 + P_2 - \frac{1}{2}\rho_1 u_1^2 - P_1 = 0$$

Neglecting the inlet velocity u_1 results in:

$$u_2 = \sqrt{\frac{2\Delta P}{\rho}}$$

where $\Delta P = P_1 - P_2$. It should be noted that the assumptions of the flow to be steady, one-dimensional and incompressible in combination with the assumption of an inlet velocity of zero violate the equation for conservation of mass for non-zero outlet velocities. In fact, requiring steady, incompressible and one-dimensional flow requires the velocity to remain constant in the channel.

The volume flow is equal to $Q = u_2 A$, with A the flow area. The area is a characteristic of the valve and it determines, together with the density and the inlet and outlet pressure, how much flow is going through the valve. Defining K_v as the volume flow of water through the valve and ΔP_w as the pressure drop along the valve corresponding to this water flow, the following expression can be obtained:

$$Q\sqrt{\frac{\rho}{2\Delta P}} = A = K_v\sqrt{\frac{\rho_w}{2\Delta P_w}}$$

Rewriting gives:

$$K_v = Q\sqrt{\frac{\rho\Delta P_w}{\rho_w\Delta P}}$$

The valve flow coefficient is defined as the water flow in m^3/h through the valve at a pressure drop of 1 bar [9]. Taking both pressure differences in bar, the flow rates (Q and K_v) in m^3/h and substituting the density of water as $\rho_w = 1000$ kg/m^3 and the pressure drop of water as $\Delta P_w = 1$, one obtains the definition of the K_v-value for liquids:

$$K_v = Q\sqrt{\frac{\rho}{\Delta P \cdot 1000}} \tag{A.2}$$

B Viscosity

The viscosity of a fluid is a measure of its resistance to gradual deformation by shear or tensile stress [26]. Maxwell discovered that the viscosity is not a function of pressure, but only of temperature, which accelerated the acceptance of the kinetic theory of gases [27]. This did however not fully fit the experiments, and in 1893 Sutherland came with a relation between the absolute temperature and the dynamic viscosity, based on the kinetic theory of ideal gases and the intermolecular force [27]. This equation, see (B.1), is known as Sutherland's law and is still commonly used to calculate the viscosity for ideal gases. Also in this study, it will be used to calculate the viscosity of ideal gases at the desired temperature from the viscosity at a reference temperature. In table B.1, the values for the reference viscosity, reference temperature and the constant C are given for several gases used during this study. It should be noted that the value of the constant C is depending on the reference temperature [27], and therefore it may differ from other sources.

$$\mu = \mu_{ref} \frac{T_{ref} + C}{T + C} \left(\frac{T}{T_{ref}} \right)^{3/2} \tag{B.1}$$

Table B.1: Reference temperature, reference viscosity and value for constant C for various gases (all data from [28]).

Gas	T_{ref} [K]	μ_{ref} [$\cdot 10^{-6}$ Pa$\cdot$s]	C [K]
Air	291.15	18.27	120
Argon	273.15	21.0	165
Helium	273	19	79.4
Hydrogen	293.85	8.76	72

C   Regulating the flow

In order to give a better insight on how the flow (according to the model described by (4.42) to (4.45)) will respond to a change in height, the three possible situations (non-choked flow, choked flow and critical flow) will be considered. All situations use a fixed inlet and outlet pressure, while the height of the channel is being changed to regulate the flow. It is important to note that there are three parameters influencing the mass flow: throughflow area, velocity, and density. These should all be taken into account when determining the mass flow.

A. Non-choked flow, i.e. $P_{out} > P_{out,c}$, is considered. Lowering the height will now have the following consequences on the important parameters:

- The throughflow area of the channel is reduced. From (4.45), it can be seen that this will linearly reduce the mass flow.
- The resistance to the flow is increased, such that the velocity of the channel is reduced. From (4.44), it is seen that the velocity for non-choked flow is quadratically dependent on the throughflow height, so the mass flow is quadratically reduced by this factor.
- The pressures remain equal, such that the density remains constant. The mass flow is therefore not changed by the density with a change in height.

Taking all these influences together, it can be concluded that a decrease in height will cubically reduce the mass flow in non-choked conditions. Similarly, an increase in height will cubically increase the mass flow in non-choked situations. This behaviour is also seen in figure C.1, where a cubic fit exactly fits the data from the model.
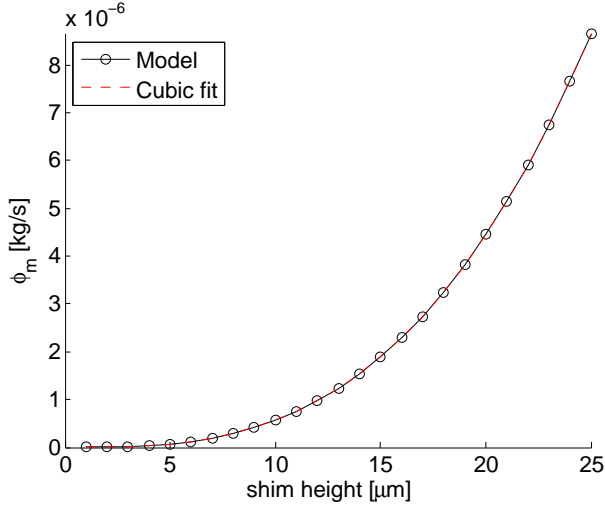
Figure C.1: Air mass flow versus height in non-choked condition ($P_{in} = 1.5$ bar, $P_{out} = 1$ bar, $T = 293$ K).
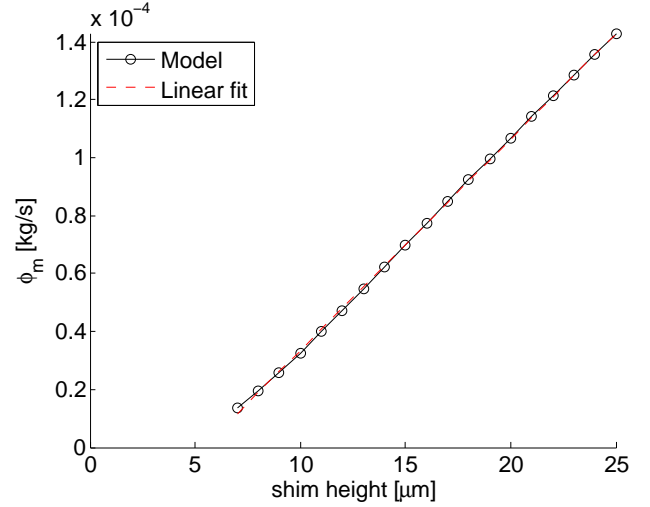
Figure C.2: Air mass flow versus height in choked condition ($P_{in} = 10$ bar, $P_{out} = 1$ bar, $T = 293$ K).

B. Choked flow, i.e. $P_{out} < P_{out,c}$, is considered. Lowering the height will now have the following consequences on the important parameters:

- The throughflow area of the channel is reduced. From (4.45), it can be seen that this will linearly reduce the mass flow.
- Since the flow is choked, the velocity will remain the same. Hence, the mass flow is not changed by the velocity with a change in height in this situation.
- The resistance to the flow is increased, such that the critical pressure goes down. This can also be seen in (4.42). The exact relation of the critical pressure to the height is difficult to determine, as also the Knudsen number is height-dependent. However, the reduction in critical outlet pressure will decrease the density at this location, such that the mass flow is reduced. In (4.45), it is seen that the mass flow is determined at

the inlet, using the inlet velocity. This velocity is however dependent on both the critical output pressure and the height, as seen in (4.44).

Taking all these influences together, it can be concluded that a decrease in height will reduce the mass flow when the flow is choked. This influence is not linear, as one may expect when only considering the reduction in area. This behaviour is also seen in figure C.2, where a linear fit is not exactly on the model data, but comes very close to it.

C. Critical flow, i.e. $P_{out} = P_{out,c}$, is considered. The influence of the height on the flow can be found from considering the above situations. When lowering the height, the critical output pressure is decreased by an increase in resistance, such that the flow is no longer choked. Situation A will therefore apply. Increasing the height, however, will result in a higher critical outlet pressure. The velocity was already at its maximum, such that the pressure at the outlet increases (and shock waves may form). Hence, situation B will apply.

D Photos Measurement Setup

In this appendix, the photographs of the measurement setup are shown. In figure D.1, the measurement setup is shown. In figure D.2, the test Piezo valve is shown.
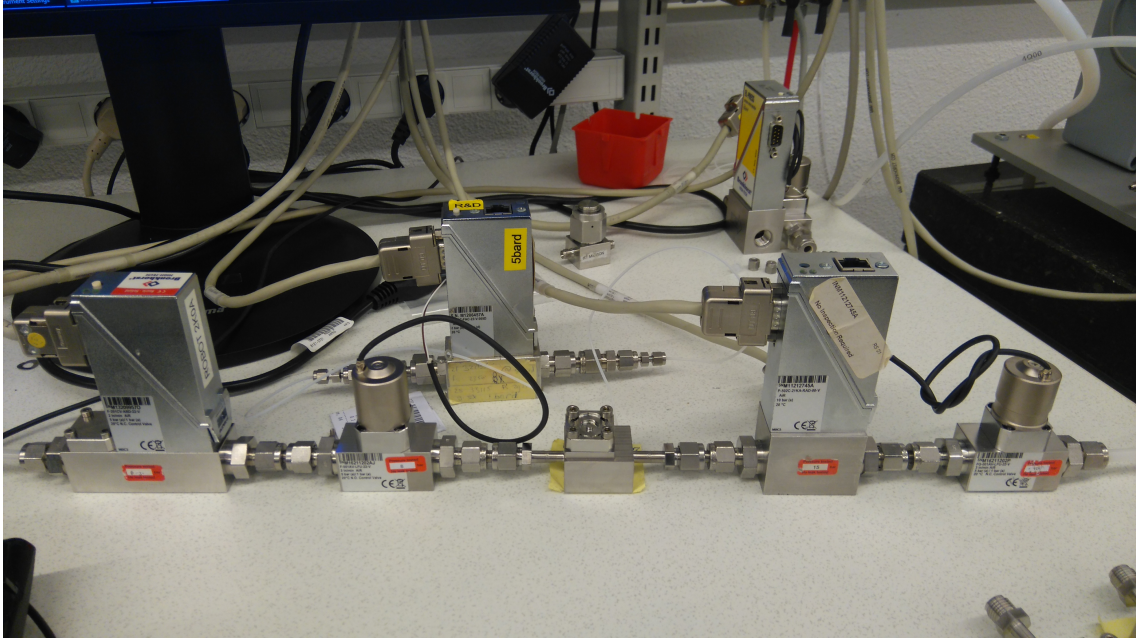
Figure D.1: Photograph of the measurement setup. Flow inlet is at the right side, while the outlet is at the left.
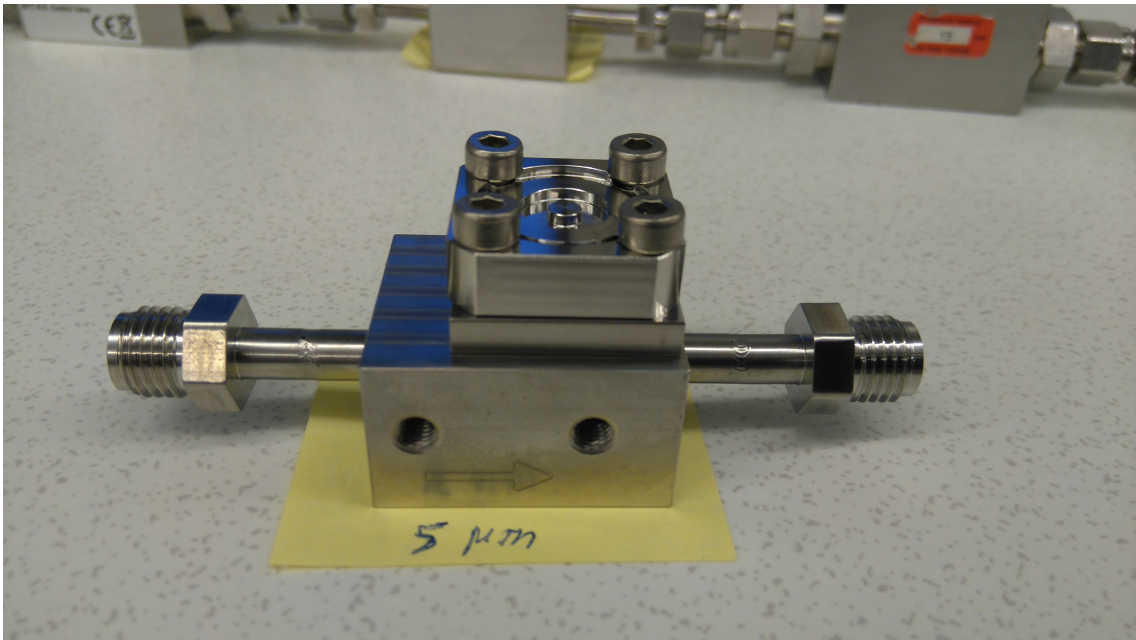
Figure D.2: Photograph of the test Piezo valve.

E   Measurement results

In this appendix, the measurement results for four different inlet pressures are given for all tested shim heights (5, 10, 20, 25 and 50 μm), in combination with the uncorrected model ($F_1 = F_2 = 1$). The medium that is used is specified in the caption. In all cases, the temperature is approximately 293 K and the medium flows inward (the "normal" direction).
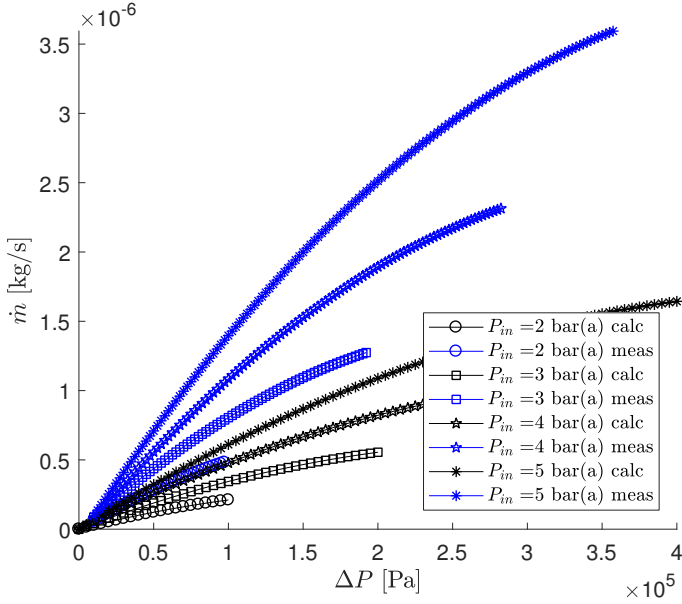
Figure E.1: Model with $F_1 = F_2 = 1$ and measurement data for air with $h = 5$ μm.
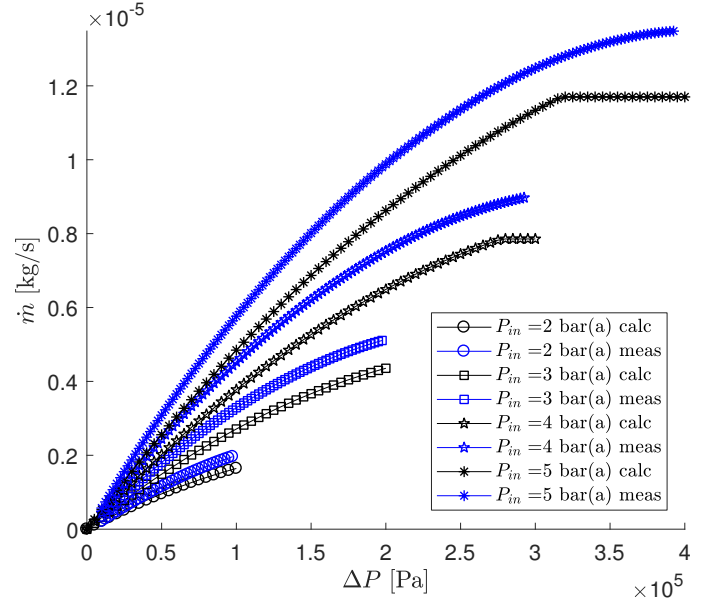
Figure E.2: Model with $F_1 = F_2 = 1$ and measurement data for air with $h = 10$ μm.
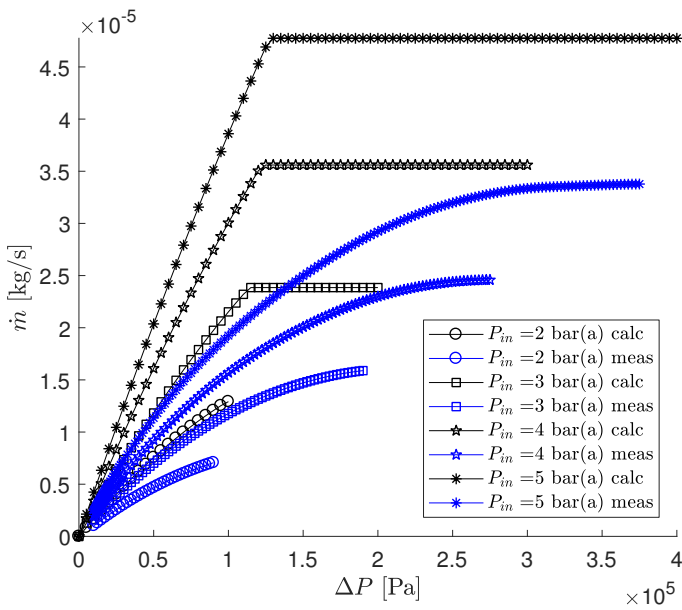
Figure E.3: Model with $F_1 = F_2 = 1$ and measurement data for air with $h = 20$ μm.
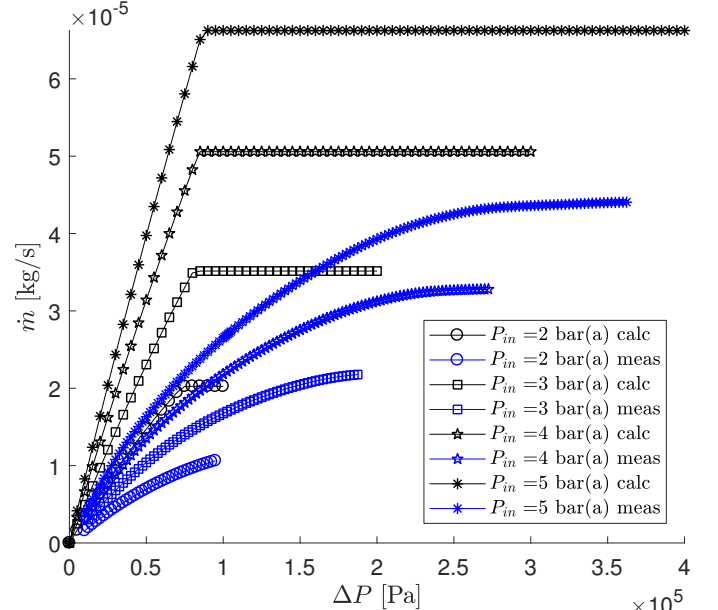
Figure E.4: Model with $F_1 = F_2 = 1$ and measurement data for air with $h = 25$ μm.
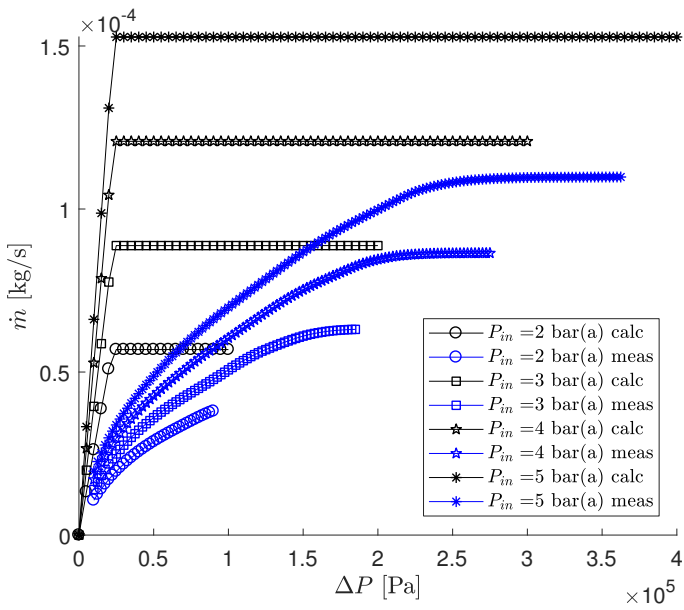
Figure E.5: Model with $F_1 = F_2 = 1$ and measurement data for air with $h = 50$ μm.
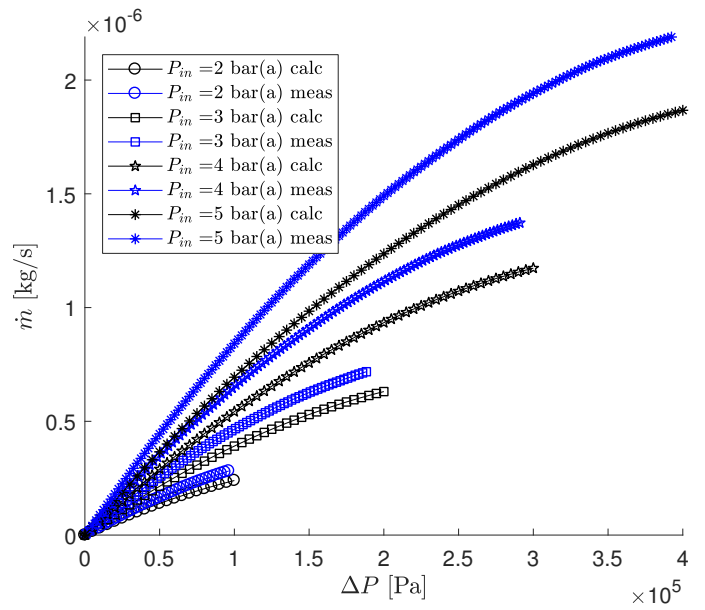
Figure E.6: Model with $F_1 = F_2 = 1$ and measurement data for argon with $h = 5$ μm.
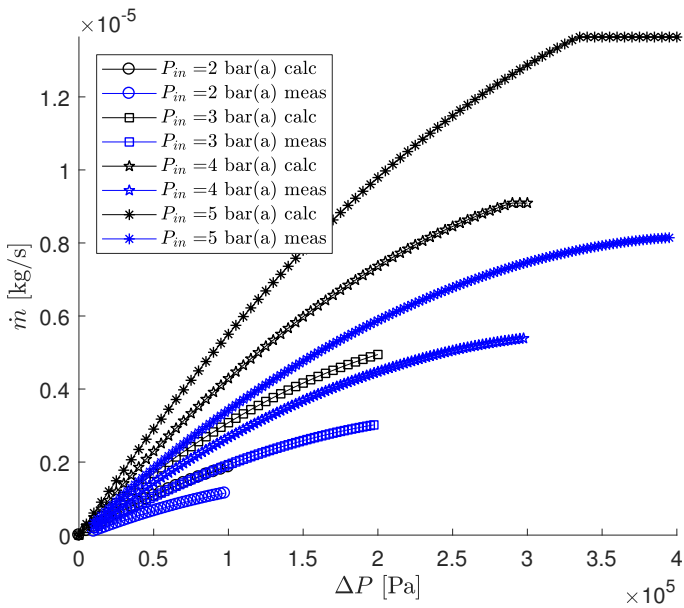
Figure E.7: Model with $F_1 = F_2 = 1$ and measurement data for argon with $h = 10$ μm.
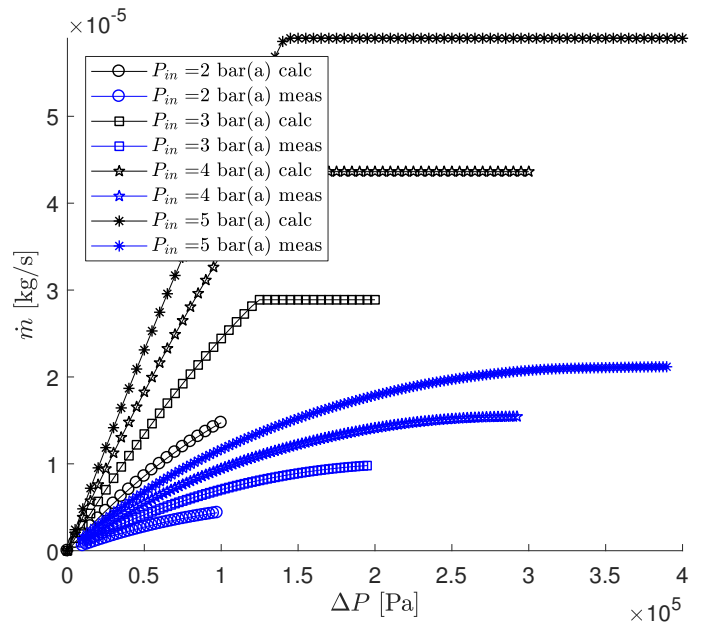
Figure E.8: Model with $F_1 = F_2 = 1$ and measurement data for argon with $h = 20$ μm.
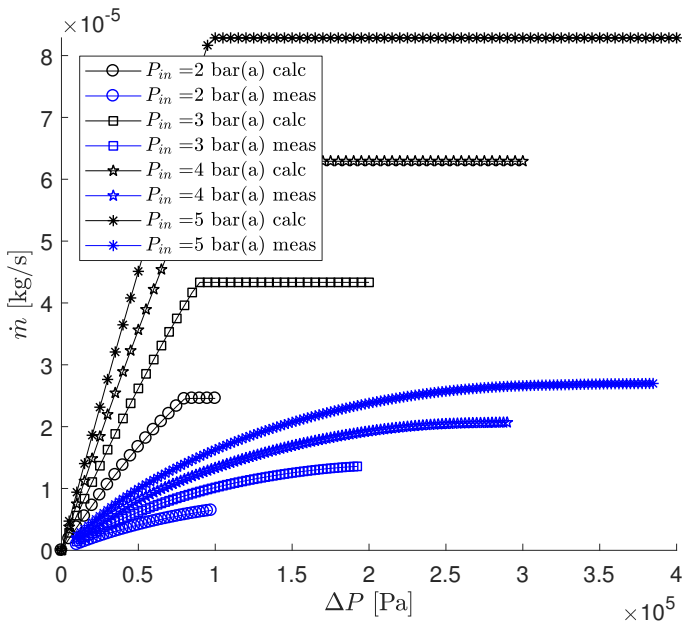
Figure E.9: Model with $F_1 = F_2 = 1$ and measurement data for argon with $h = 25$ μm.
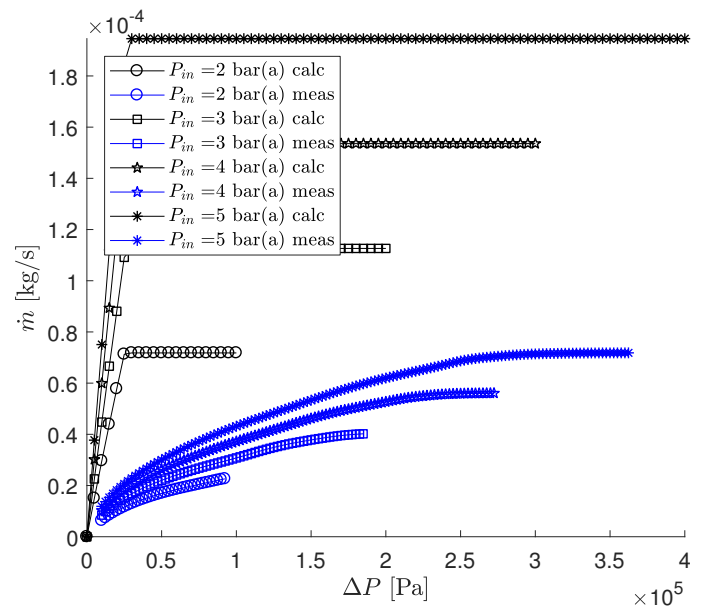
Figure E.10: Model with $F_1 = F_2 = 1$ and measurement data for argon with $h = 50$ μm.
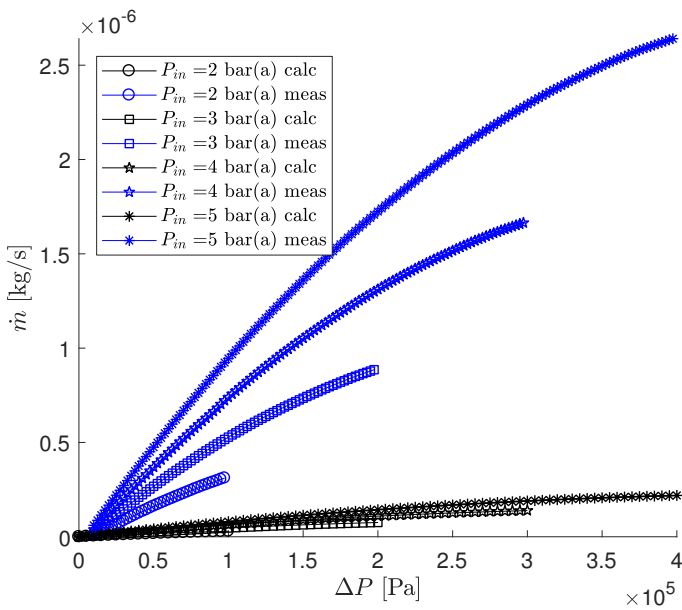
Figure E.11: Model with $F_1 = F_2 = 1$ and measurement data for helium with $h = 5$ μm.
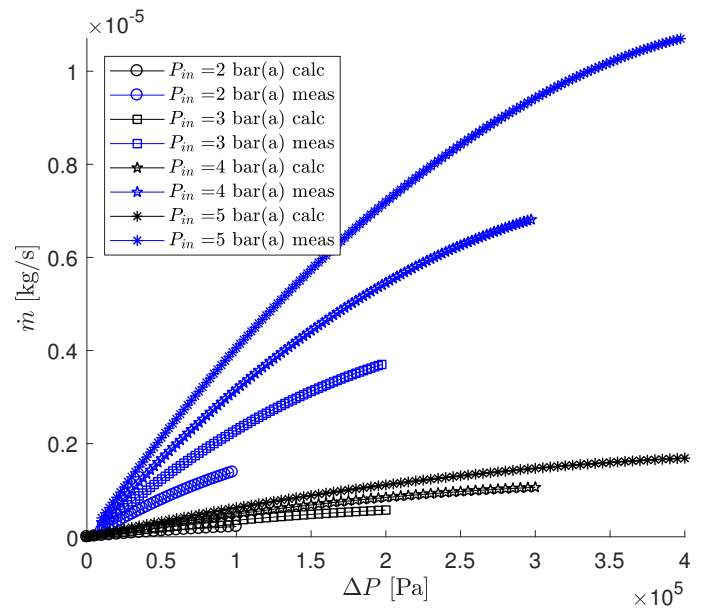
Figure E.12: Model with $F_1 = F_2 = 1$ and measurement data for helium with $h = 10$ μm.
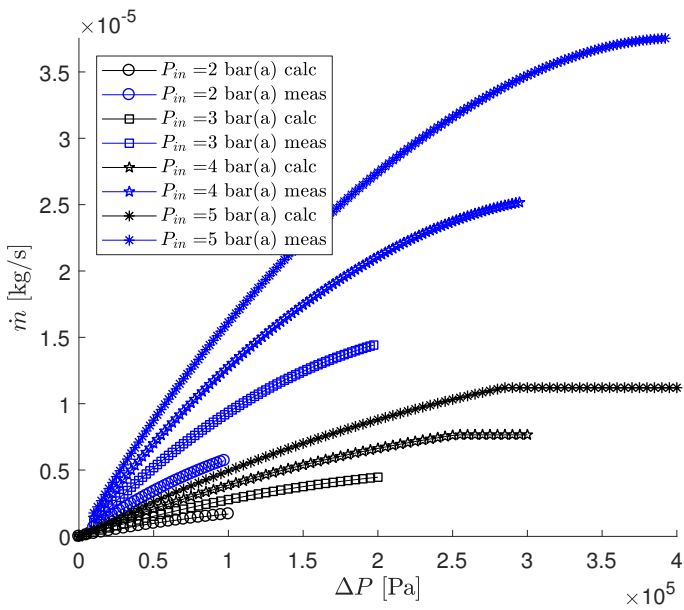
Figure E.13: Model with $F_1 = F_2 = 1$ and measurement data for helium with $h = 20$ μm.
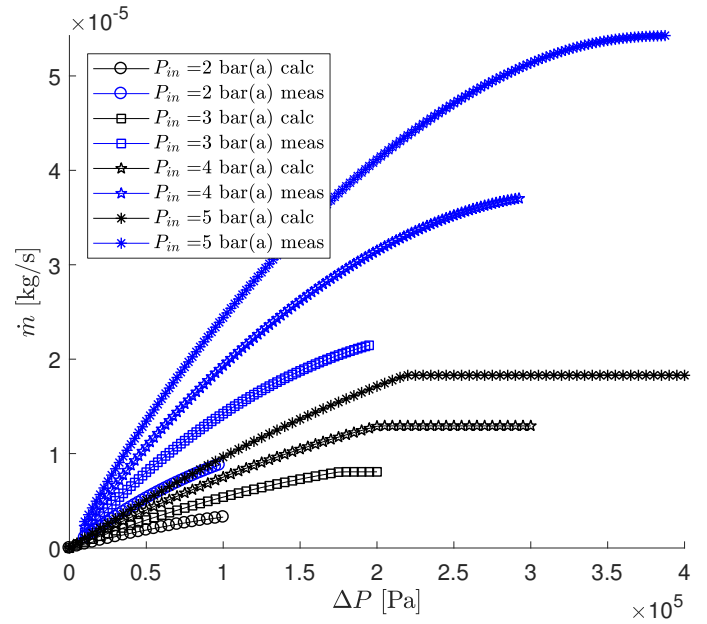
Figure E.14: Model with $F_1 = F_2 = 1$ and measurement data for helium with $h = 25$ μm.
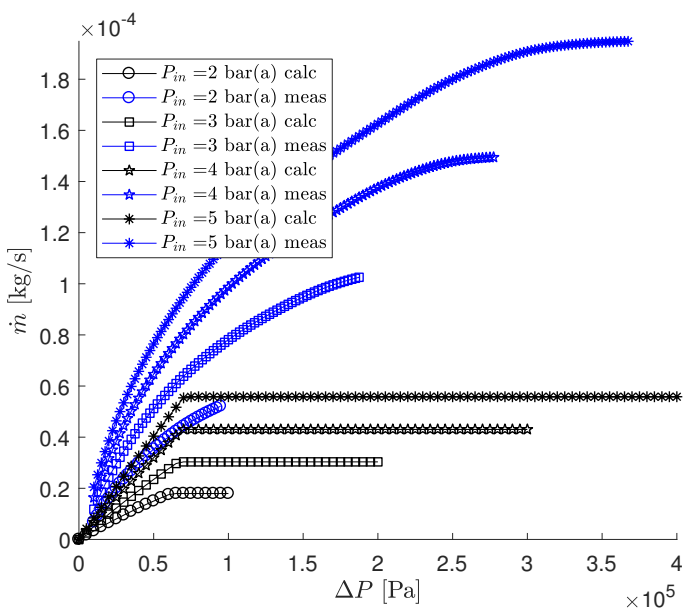
Figure E.15: Model with $F_1 = F_2 = 1$ and measurement data for helium with $h = 50$ μm.
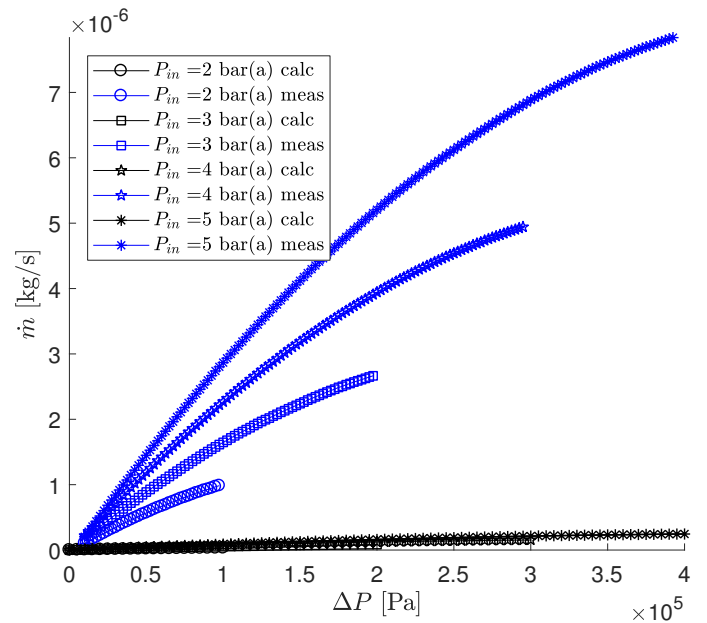
Figure E.16: Model with $F_1 = F_2 = 1$ and measurement data for hydrogen with $h = 5$ μm.
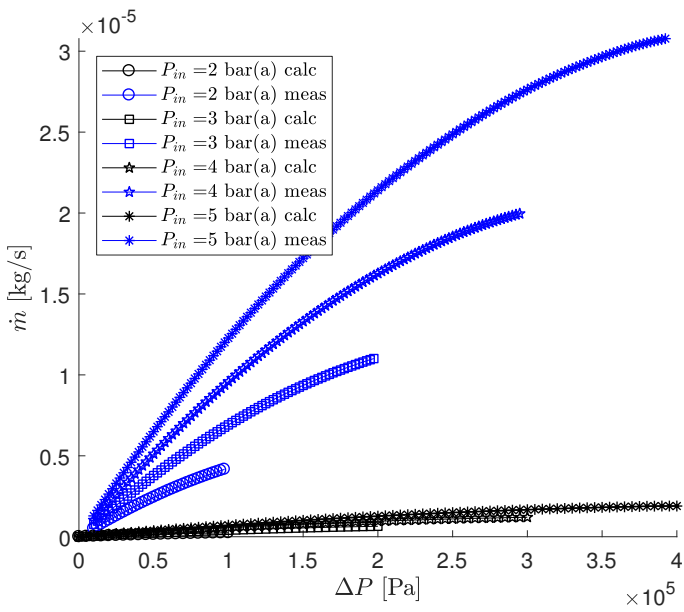
Figure E.17: Model with $F_1 = F_2 = 1$ and measurement data for hydrogen with $h = 10$ μm.
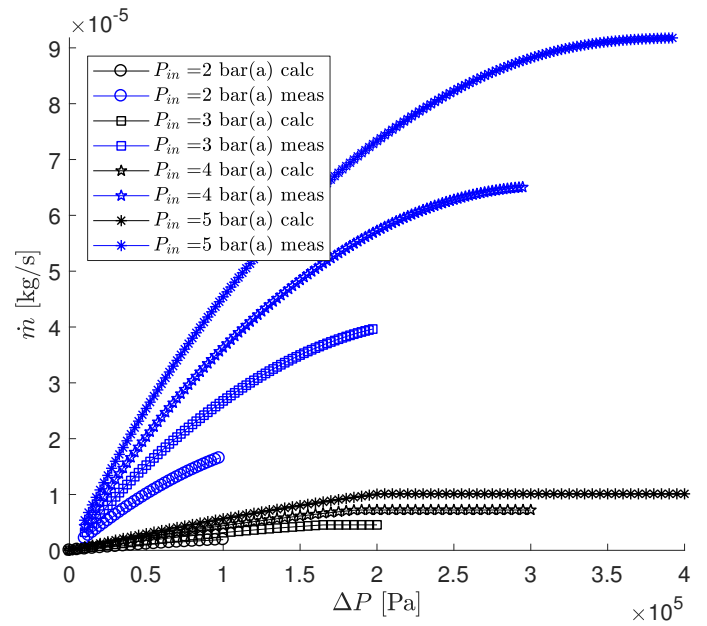
Figure E.18: Model with $F_1 = F_2 = 1$ and measurement data for hydrogen with $h = 20$ μm.
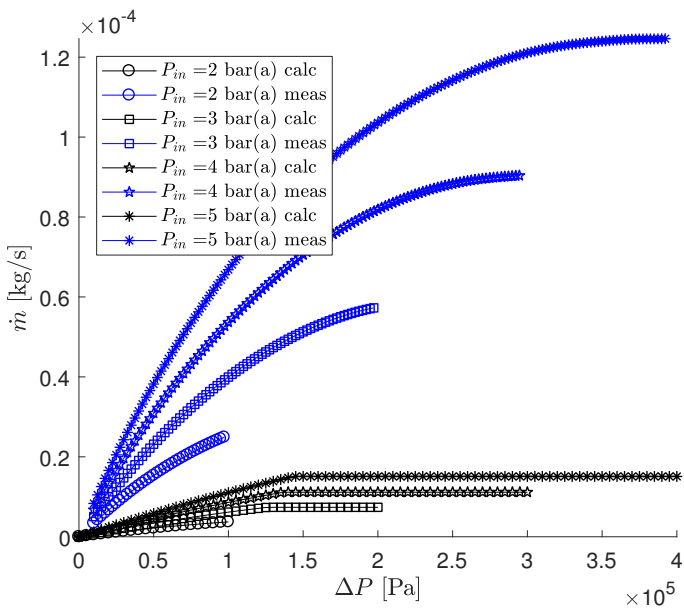
Figure E.19: Model with $F_1 = F_2 = 1$ and measurement data for hydrogen with $h = 25$ μm.
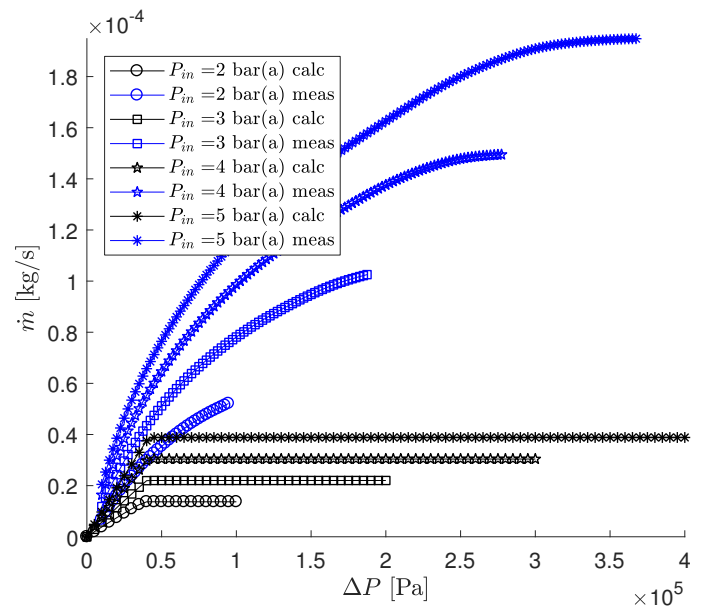
Figure E.20: Model with $F_1 = F_2 = 1$ and measurement data for hydrogen with $h = 50$ μm.

F   Measurement results with height-based correction

In this appendix, the measurement results for four different inlet pressures are given for all tested shim heights (5, 10, 20, 25 and 50 μm), in combination with the height-based corrections: $F_1 = \frac{12 \cdot 10^{-6}}{h}$ and $F_2 = \left(\frac{12 \cdot 10^{-6}}{h}\right)^{0.4}$. The medium that is used is specified in the caption. In all cases, the temperature is approximately 293 K and the medium flows inward (the "normal" direction). It can be observed that the correction works relatively good for air, but not for the largest shim height ($h = 50 \mu$m). For the other gases, the correction is insufficient.
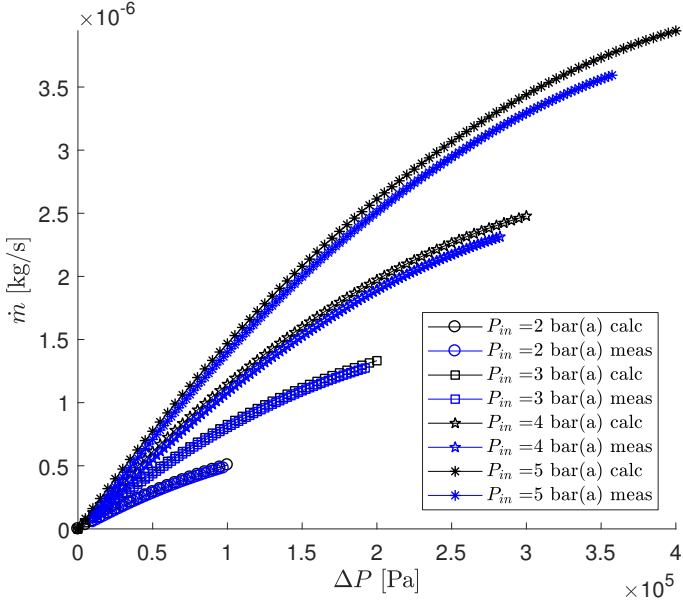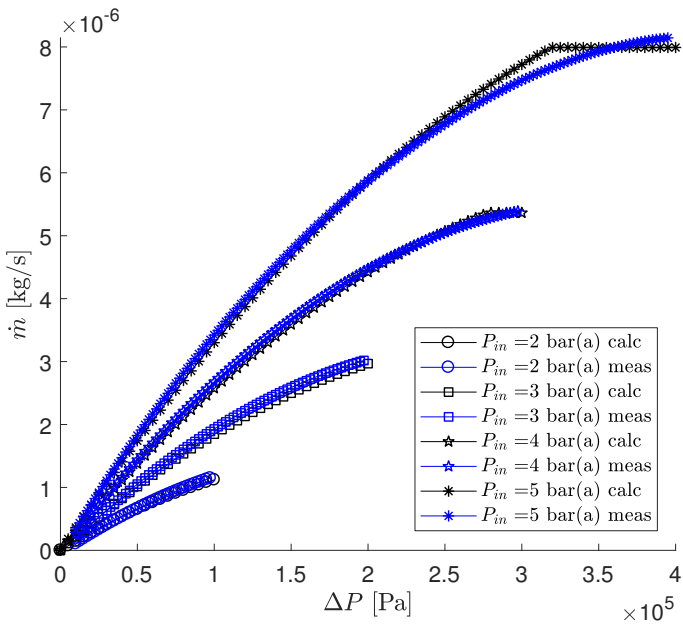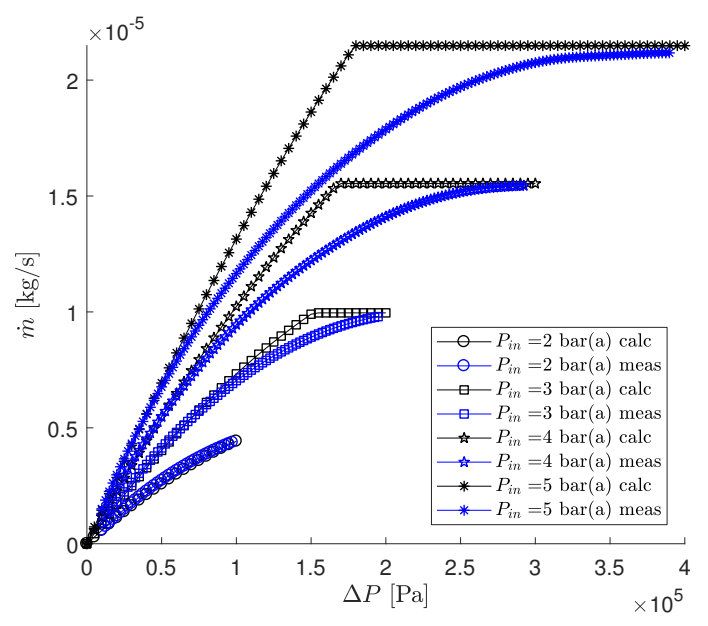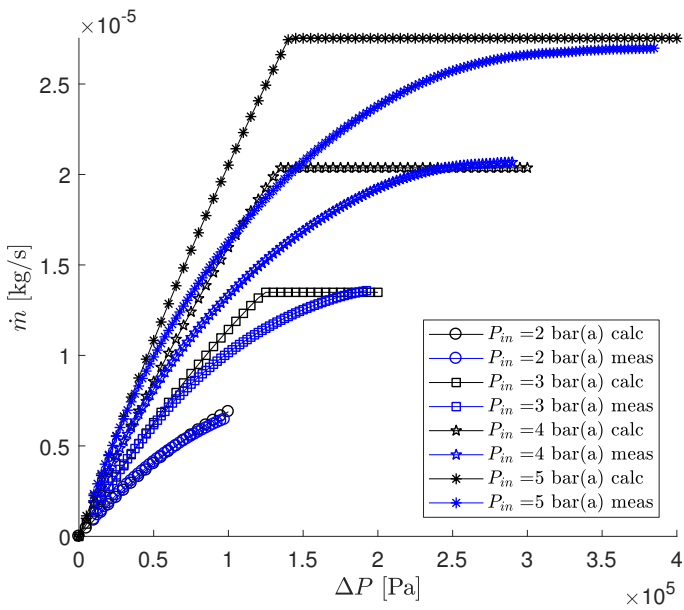

Figure F.1: Model with $F_1 = \frac{12 \cdot 10^{-6}}{h}$ and $F_2 = \left(\frac{12 \cdot 10^{-6}}{h}\right)^{0.4}$ and data for air with $h = 5 \mu$m.
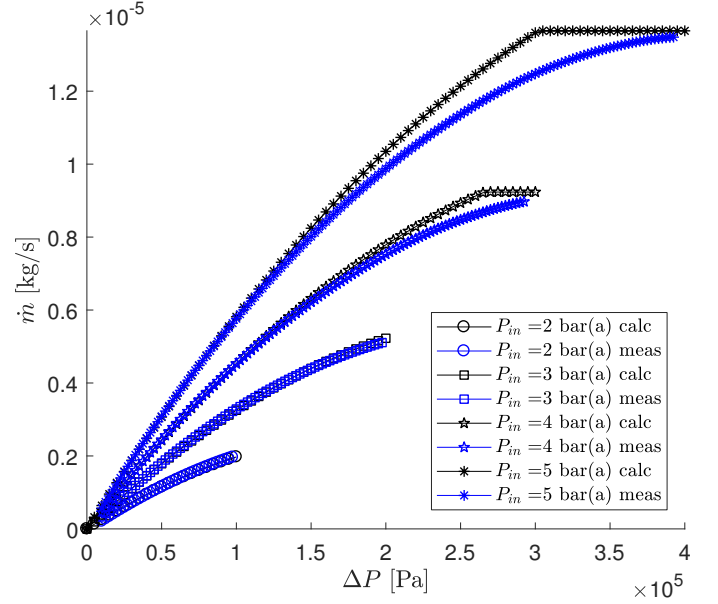
Figure F.2: Model with $F_1 = \frac{12 \cdot 10^{-6}}{h}$ and $F_2 = \left(\frac{12 \cdot 10^{-6}}{h}\right)^{0.4}$ and data for air with $h = 10 \mu$m.
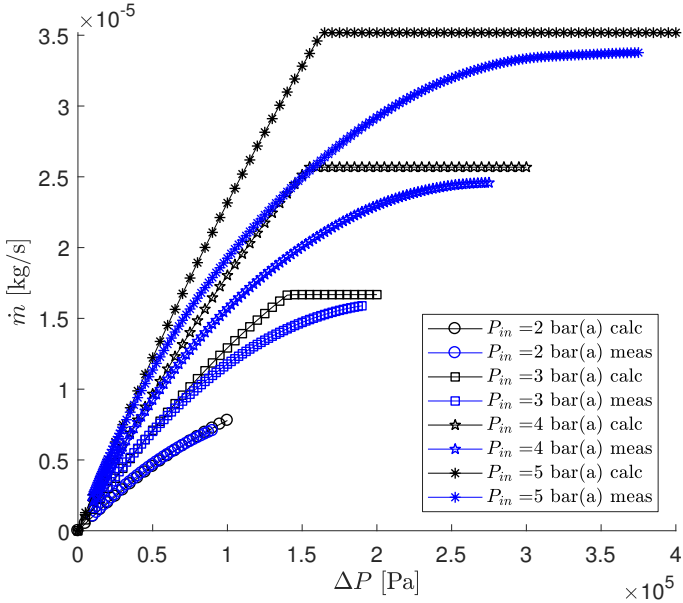
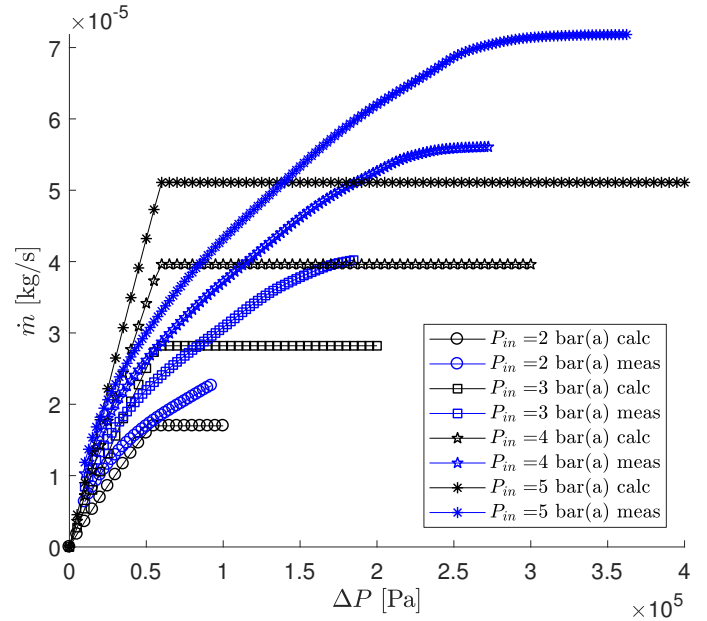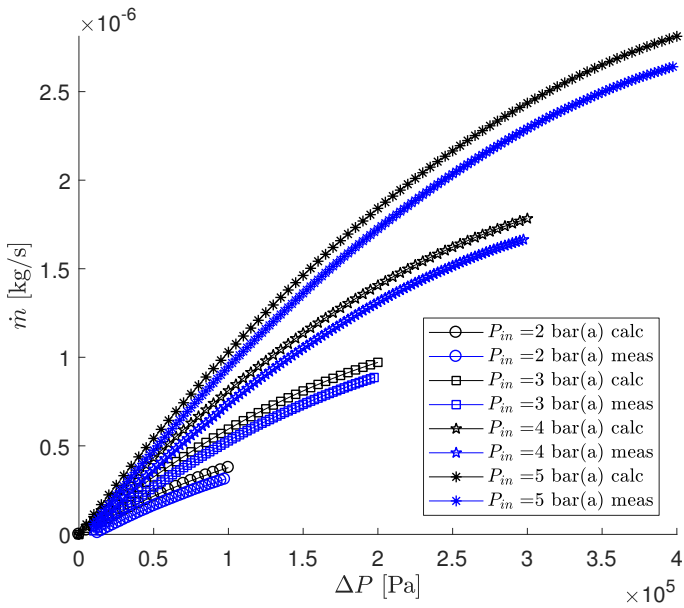Figure F.3: Model with $F_1 = \frac{12 \cdot 10^{-6}}{h}$ and $F_2 = \left(\frac{12 \cdot 10^{-6}}{h}\right)^{0.4}$ and data for air with $h = 20 \mu$m.
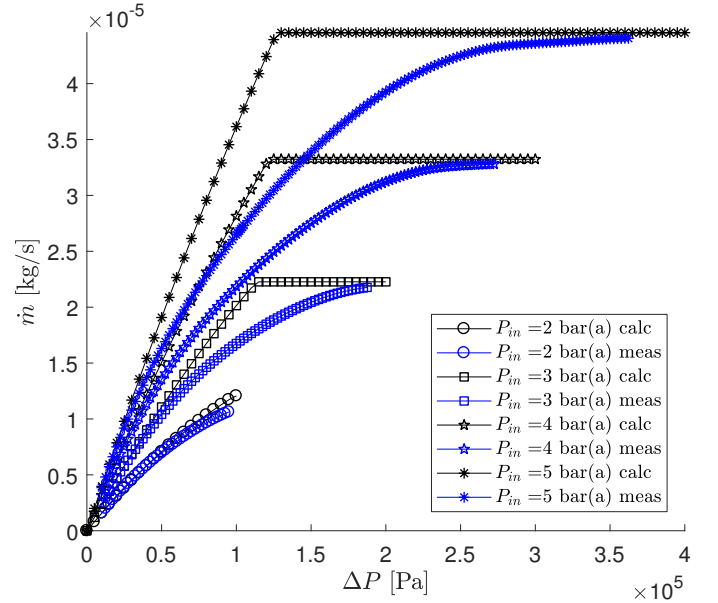
Figure F.4: Model with $F_1 = \frac{12 \cdot 10^{-6}}{h}$ and $F_2 = \left(\frac{12 \cdot 10^{-6}}{h}\right)^{0.4}$ and data for air with $h = 25 \mu$m.
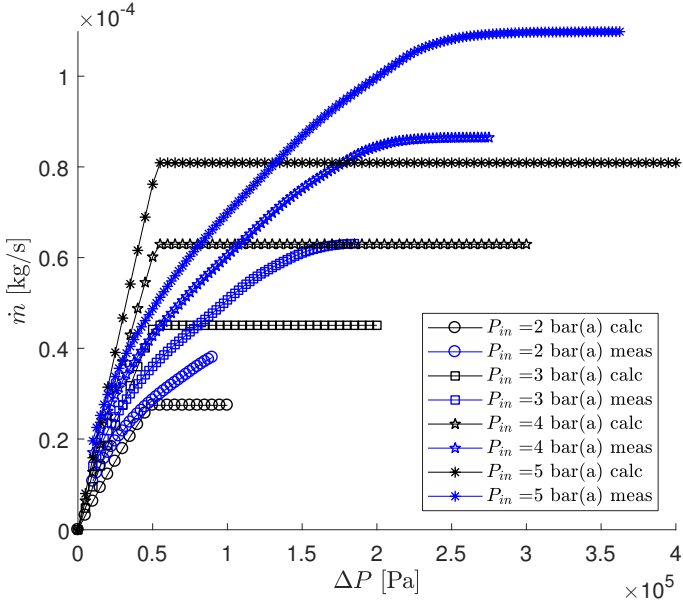
Figure F.5: Model with $F_1 = \frac{12 \cdot 10^{-6}}{h}$ and $F_2 = \left(\frac{12 \cdot 10^{-6}}{h}\right)^{0.4}$ and data for air with $h = 50 \ \mu$m.
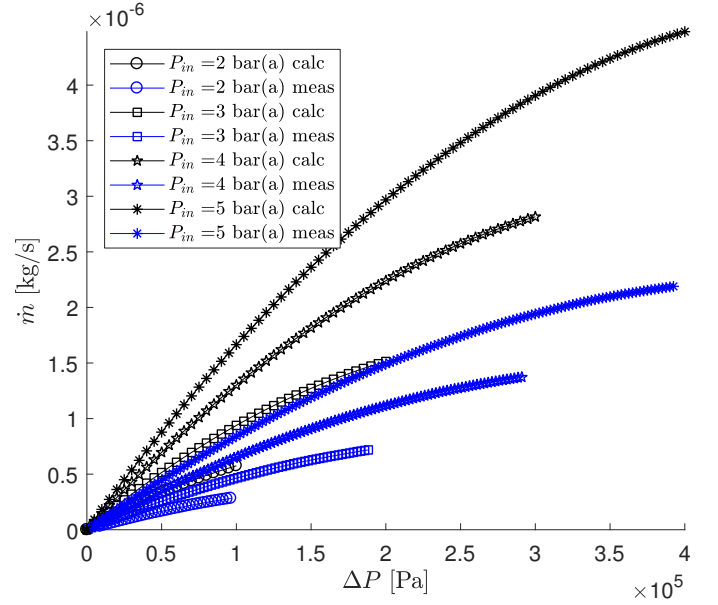
Figure F.6: Model with $F_1 = \frac{12 \cdot 10^{-6}}{h}$ and $F_2 = \left(\frac{12 \cdot 10^{-6}}{h}\right)^{0.4}$ and data for argon with $h = 5 \ \mu$m.
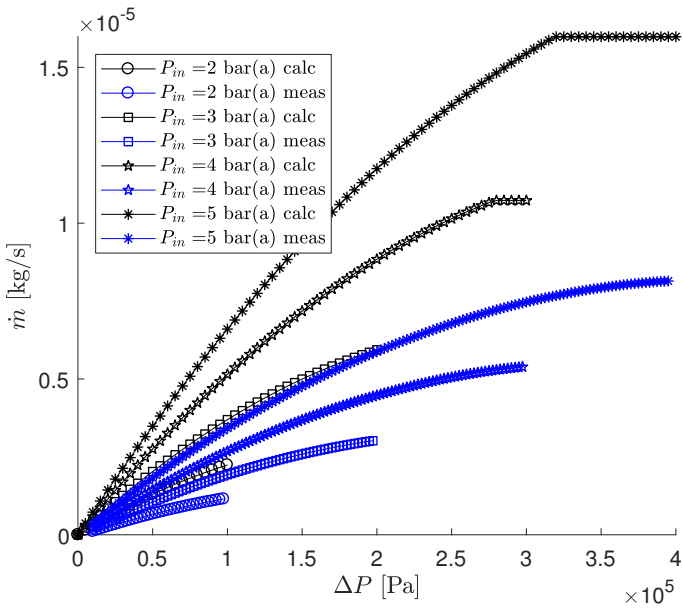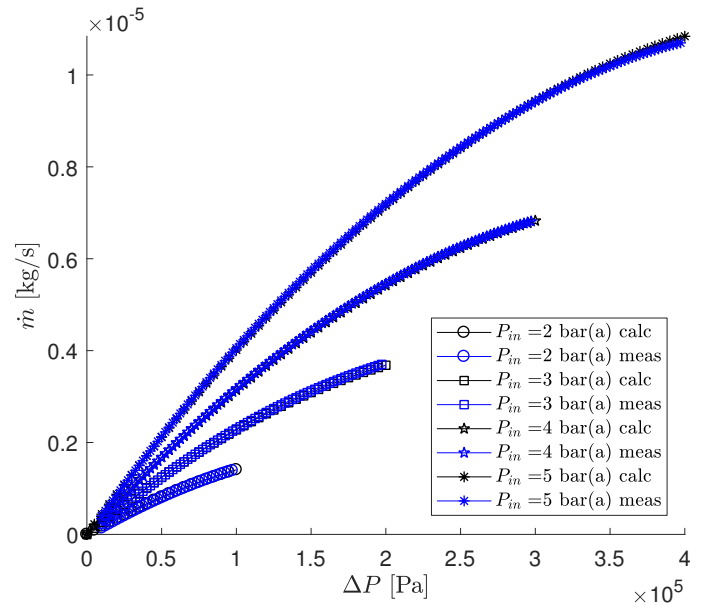

Figure F.7: Model with $F_1 = \frac{12 \cdot 10^{-6}}{h}$ and $F_2 = \left(\frac{12 \cdot 10^{-6}}{h}\right)^{0.4}$ and data for argon with $h = 10 \ \mu$m.
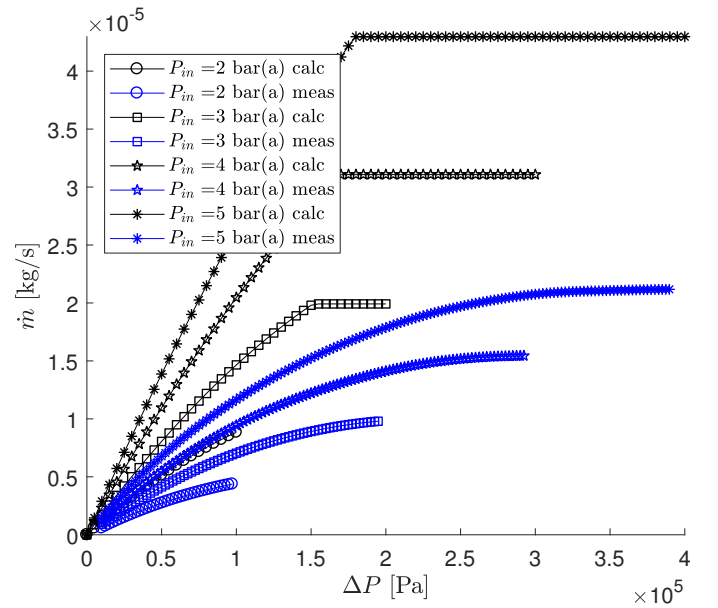
Figure F.8: Model with $F_1 = \frac{12 \cdot 10^{-6}}{h}$ and $F_2 = \left(\frac{12 \cdot 10^{-6}}{h}\right)^{0.4}$ and data for argon with $h = 20 \ \mu$m.
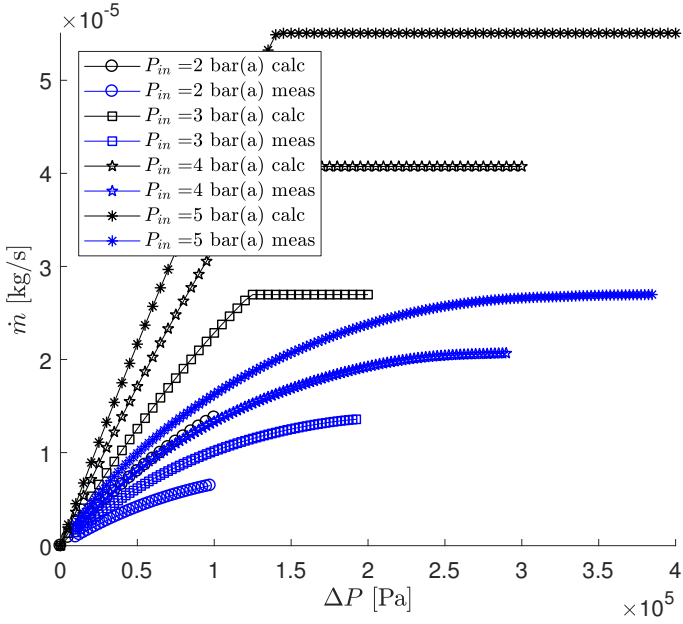
Figure F.9: Model with $F_1 = \frac{12 \cdot 10^{-6}}{h}$ and $F_2 = \left(\frac{12 \cdot 10^{-6}}{h}\right)^{0.4}$ and data for argon with $h = 25\ \mu$m.
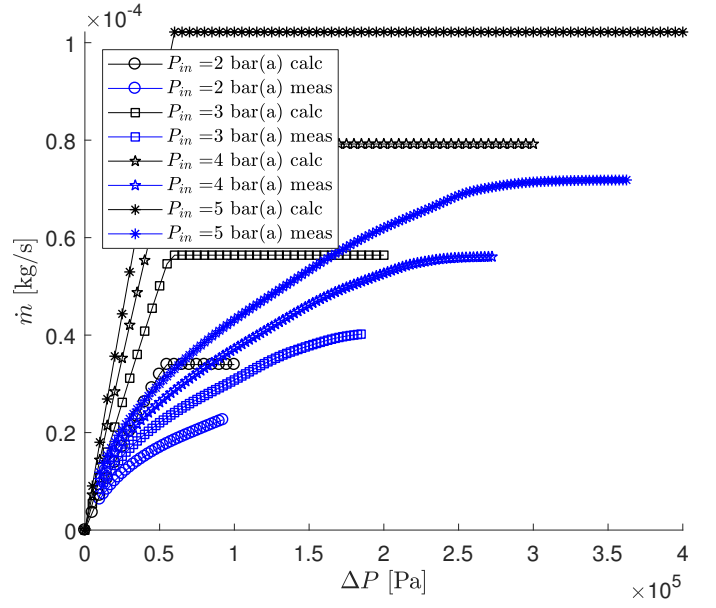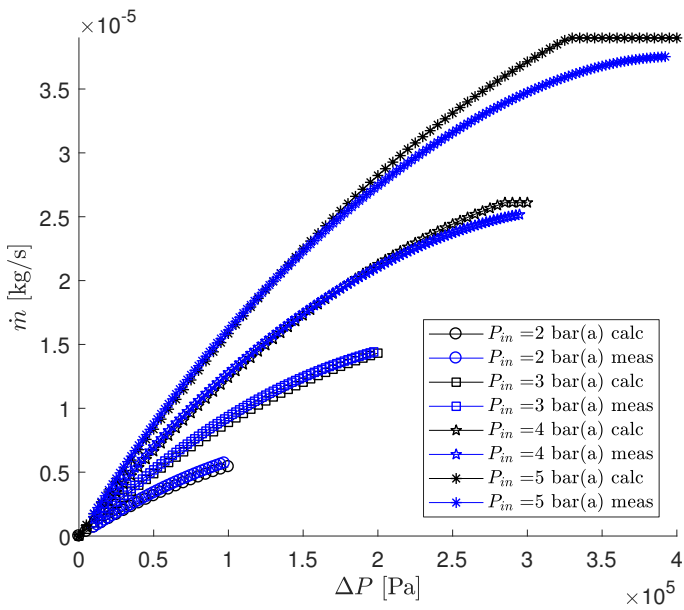

Figure F.10: Model with $F_1 = \frac{12 \cdot 10^{-6}}{h}$ and $F_2 = \left(\frac{12 \cdot 10^{-6}}{h}\right)^{0.4}$ and data for argon with $h = 50\ \mu$m.
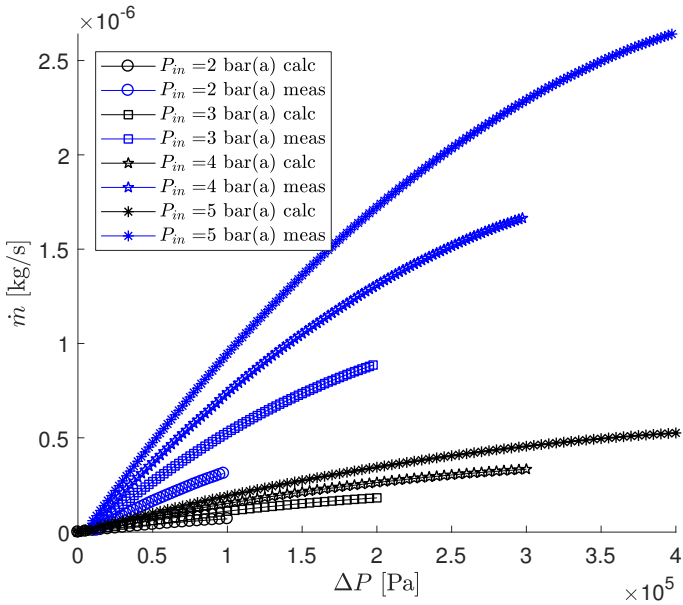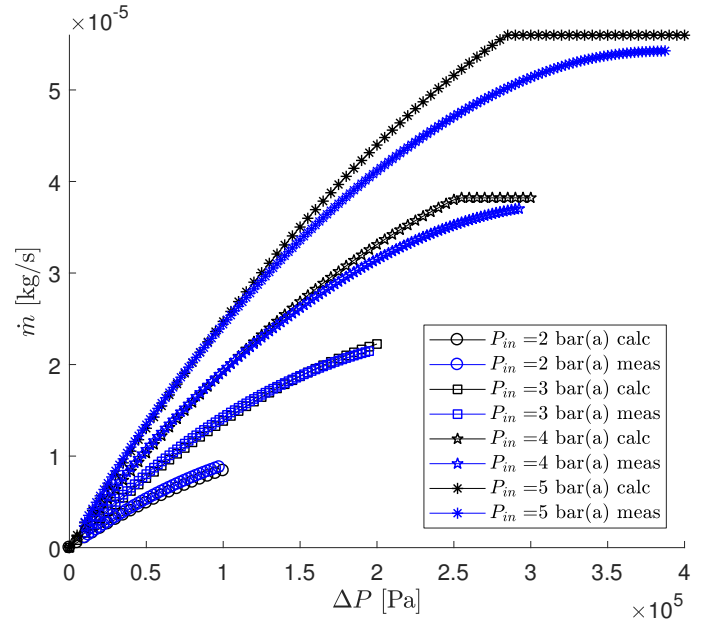

Figure F.11: Model with $F_1 = \frac{12 \cdot 10^{-6}}{h}$ and $F_2 = \left(\frac{12 \cdot 10^{-6}}{h}\right)^{0.4}$ and data for helium with $h = 5\ \mu$m.
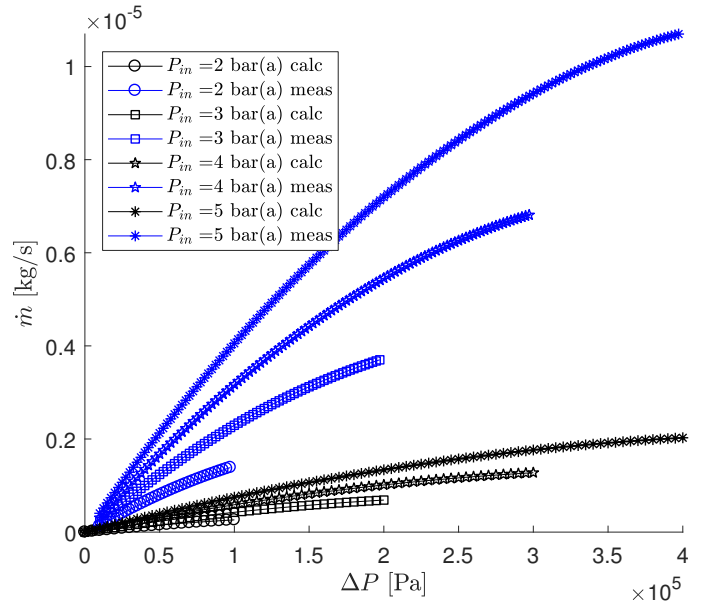
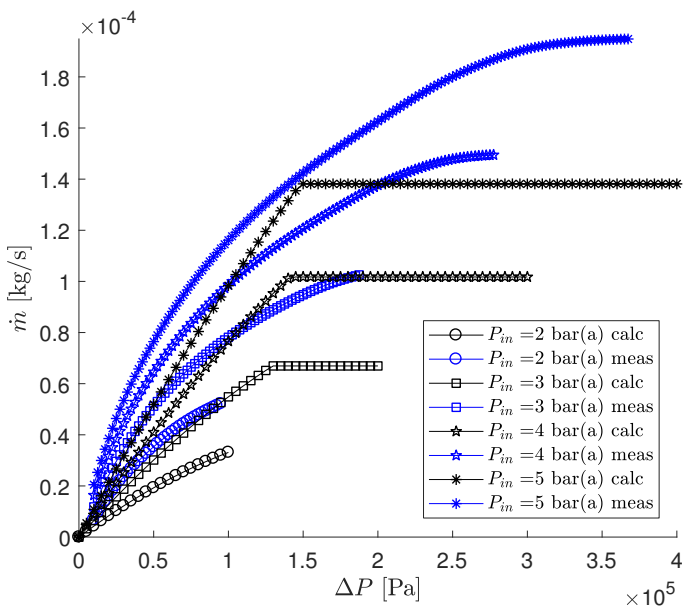Figure F.12: Model with $F_1 = \frac{12 \cdot 10^{-6}}{h}$ and $F_2 = \left(\frac{12 \cdot 10^{-6}}{h}\right)^{0.4}$ and data for helium with $h = 10\ \mu$m.
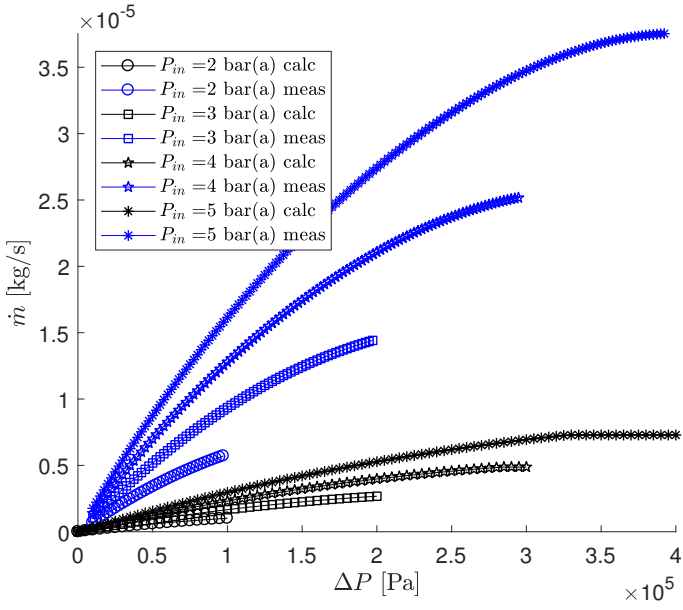
Figure F.13: Model with $F_1 = \frac{12 \cdot 10^{-6}}{h}$ and $F_2 = \left(\frac{12 \cdot 10^{-6}}{h}\right)^{0.4}$ and data for helium with $h = 20\ \mu$m.
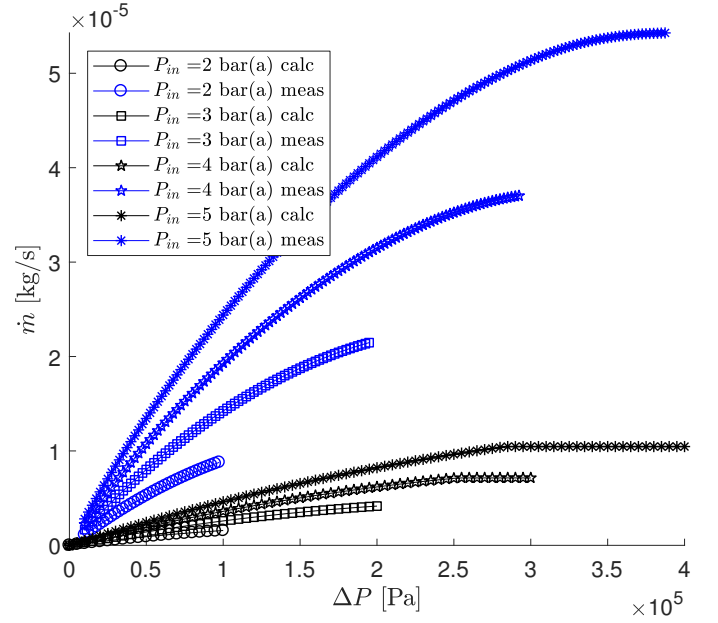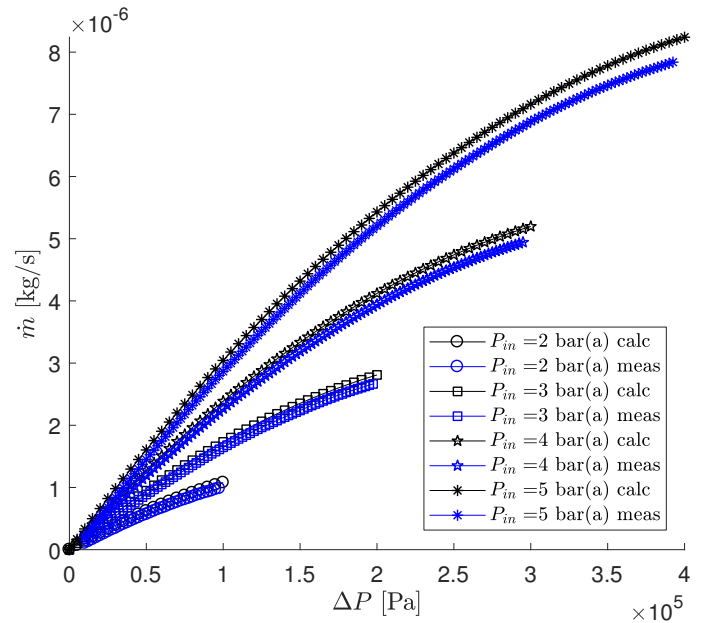

Figure F.14: Model with $F_1 = \frac{12 \cdot 10^{-6}}{h}$ and $F_2 = \left(\frac{12 \cdot 10^{-6}}{h}\right)^{0.4}$ and data for helium with $h = 25\ \mu$m.
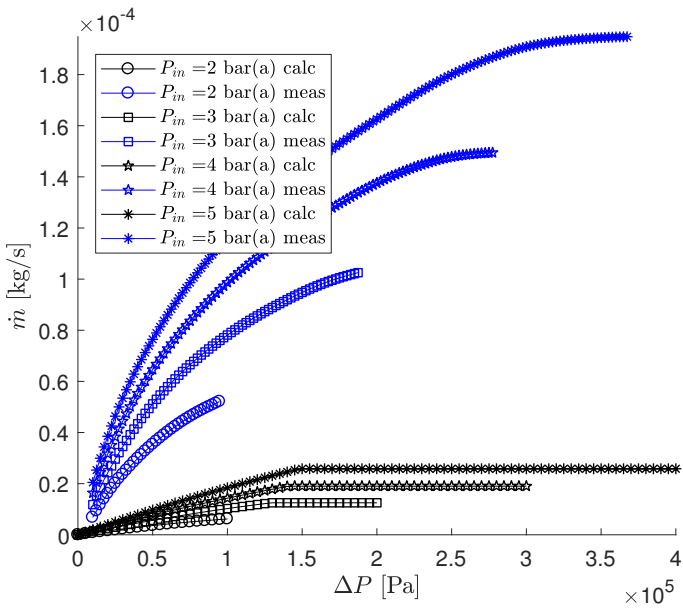
Figure F.15: Model with $F_1 = \frac{12 \cdot 10^{-6}}{h}$ and $F_2 = \left(\frac{12 \cdot 10^{-6}}{h}\right)^{0.4}$ and data for helium with $h = 50\ \mu$m.
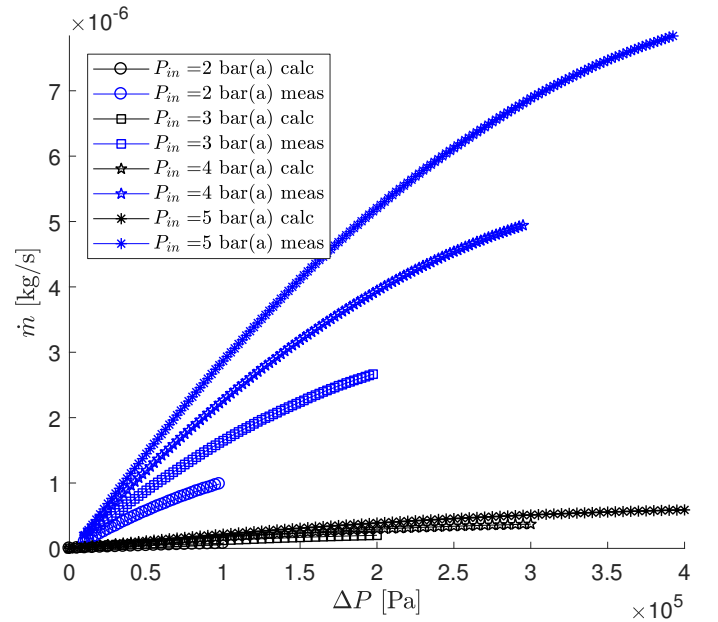
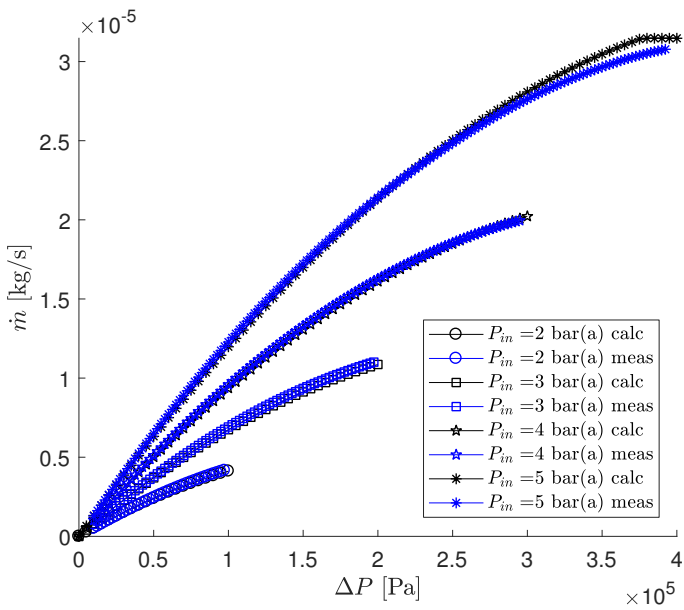Figure F.16: Model with $F_1 = \frac{12 \cdot 10^{-6}}{h}$ and $F_2 = \left(\frac{12 \cdot 10^{-6}}{h}\right)^{0.4}$ and data for hydrogen with $h = 5\ \mu$m.
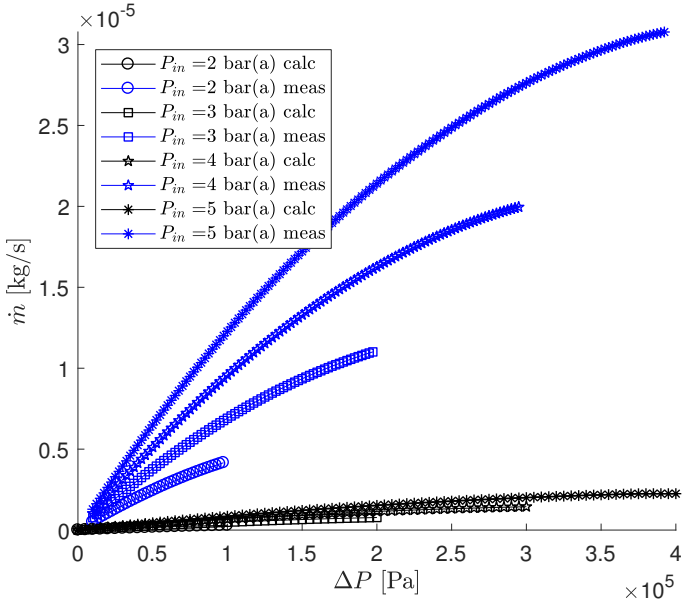
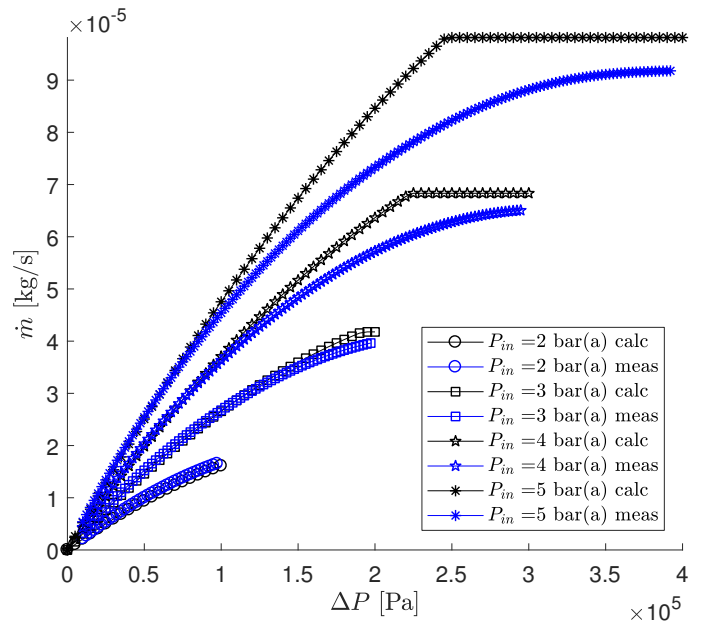Figure F.17: Model with $F_1 = \frac{12\cdot10^{-6}}{h}$ and $F_2 = \left(\frac{12\cdot10^{-6}}{h}\right)^{0.4}$ and data for hydrogen with $h = 10~\mu$m.
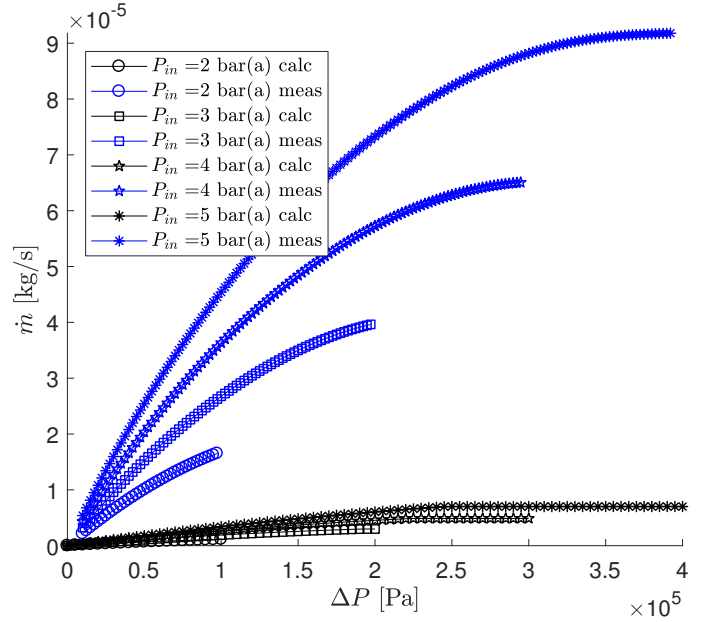
Figure F.18: Model with $F_1 = \frac{12\cdot10^{-6}}{h}$ and $F_2 = \left(\frac{12\cdot10^{-6}}{h}\right)^{0.4}$ and data for hydrogen with $h = 20~\mu$m.
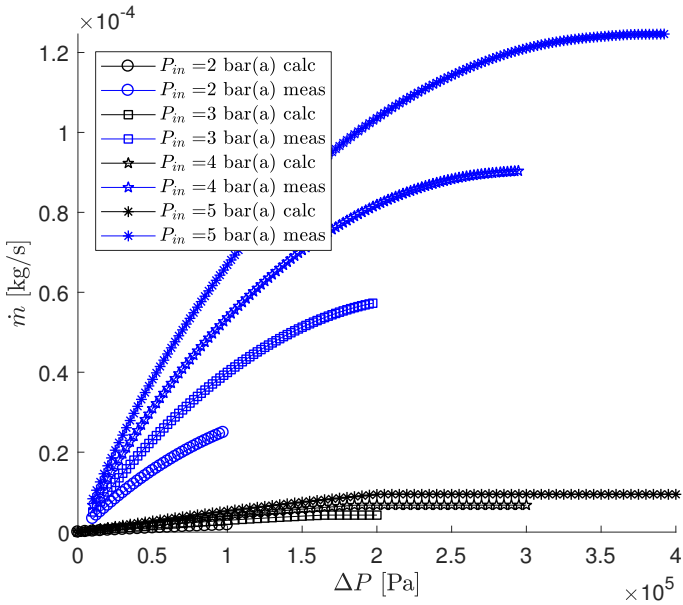
Figure F.19: Model with $F_1 = \frac{12\cdot10^{-6}}{h}$ and $F_2 = \left(\frac{12\cdot10^{-6}}{h}\right)^{0.4}$ and data for hydrogen with $h = 25~\mu$m.
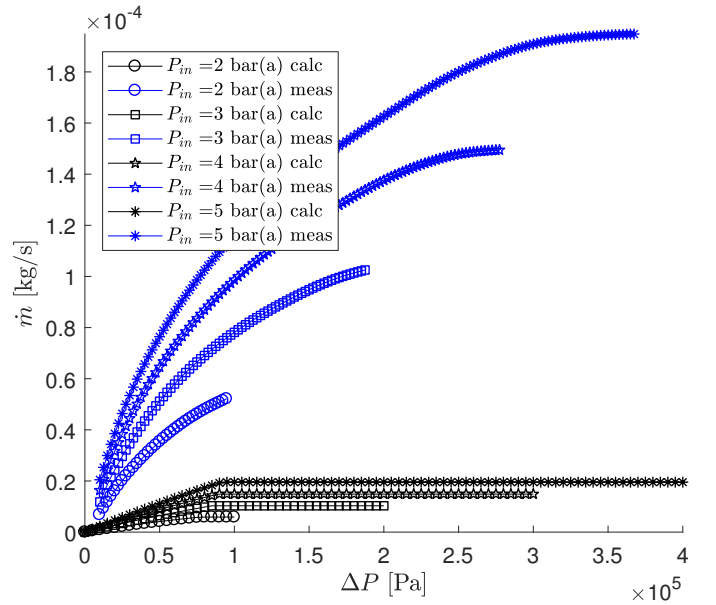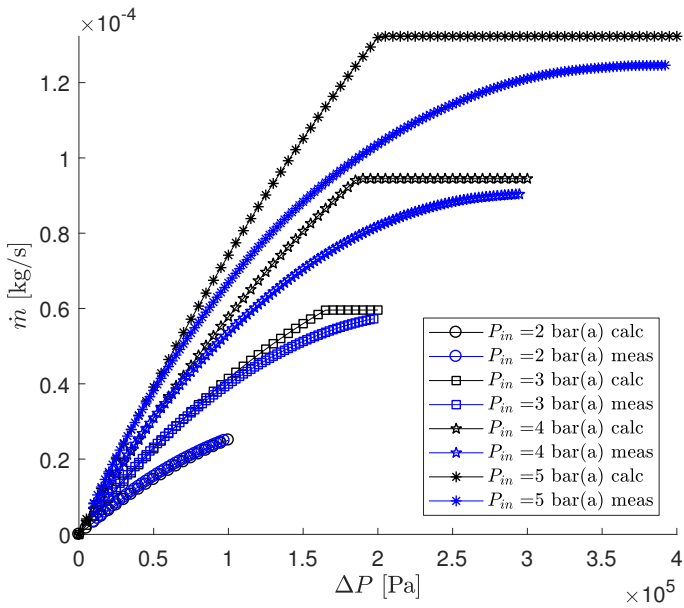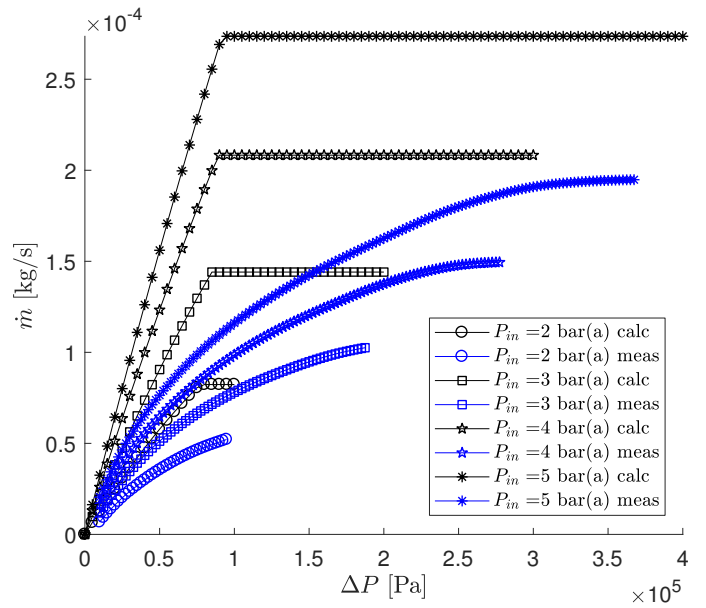

Figure F.20: Model with $F_1 = \frac{12\cdot10^{-6}}{h}$ and $F_2 = \left(\frac{12\cdot10^{-6}}{h}\right)^{0.4}$ and data for hydrogen with $h = 50~\mu$m.

G Measurement results with gas-specific corrections

In this appendix, the measurement results for four different inlet pressures are given for all tested shim heights (5, 10, 20, 25 and 50 μm), in combination with the gas-specific and height-based corrections (a gas-specific constant is multiplied with the height-based correction, which together forms the correcting fudge factor). The medium that is used is specified in the caption. In all cases, the temperature is approximately 293 K and the medium flows inward (the "normal" direction). It can be observed that the corrections give acceptable results, but not for the largest shim height ($h = 50$ μm). However, the asymptotic behaviour that is observed in the measurements is not included in the model.
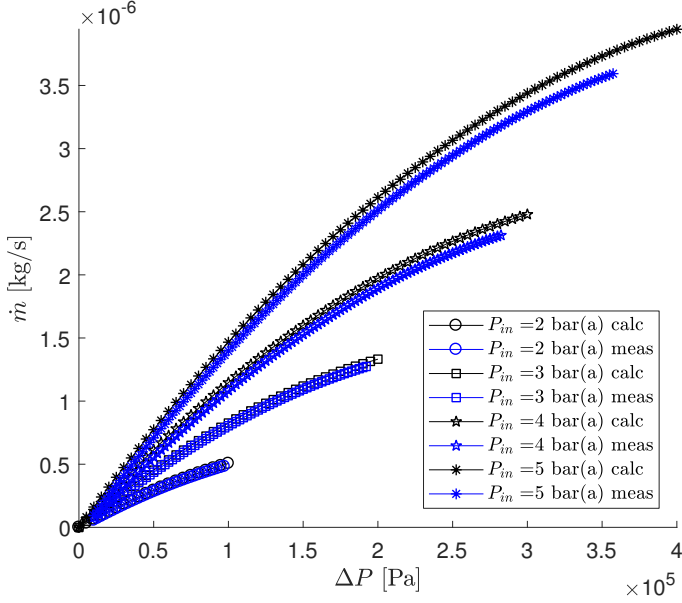
Figure G.1: Model with $F_1 = \frac{12 \cdot 10^{-6}}{h}$ and $F_2 = \left(\frac{12 \cdot 10^{-6}}{h}\right)^{0.4}$ and data for air with $h = 5$ μm.
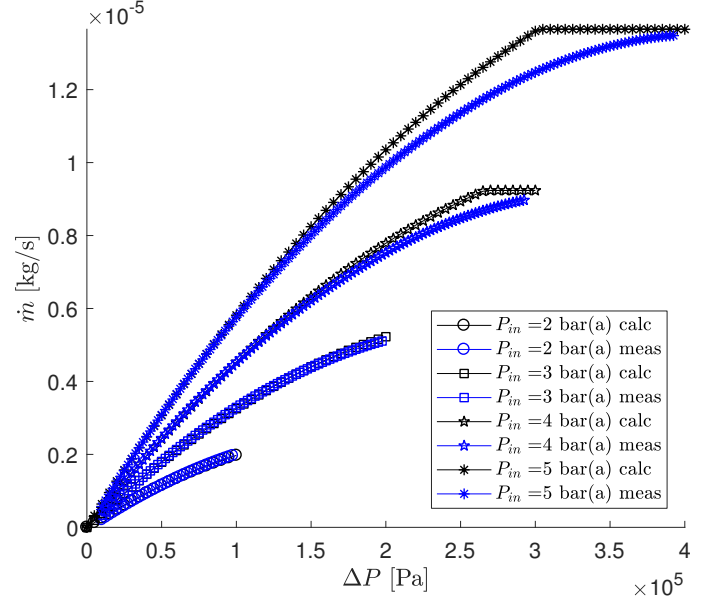
Figure G.2: Model with $F_1 = \frac{12 \cdot 10^{-6}}{h}$ and $F_2 = \left(\frac{12 \cdot 10^{-6}}{h}\right)^{0.4}$ and data for air with $h = 10$ μm.
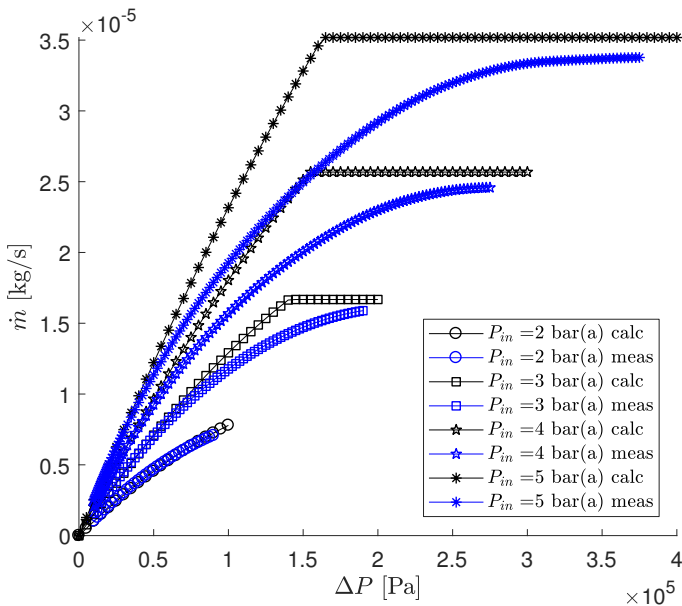
Figure G.3: Model with $F_1 = \frac{12 \cdot 10^{-6}}{h}$ and $F_2 = \left(\frac{12 \cdot 10^{-6}}{h}\right)^{0.4}$ and data for air with $h = 20$ μm.
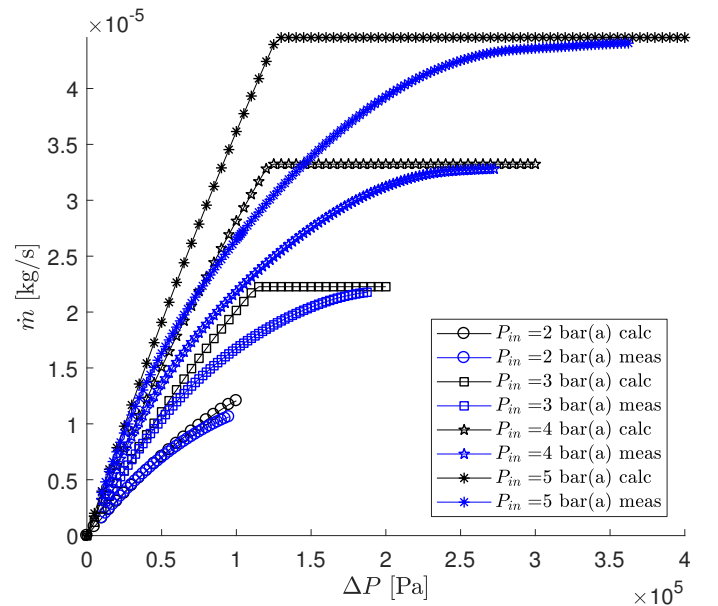
Figure G.4: Model with $F_1 = \frac{12 \cdot 10^{-6}}{h}$ and $F_2 = \left(\frac{12 \cdot 10^{-6}}{h}\right)^{0.4}$ and data for air with $h = 25$ μm.
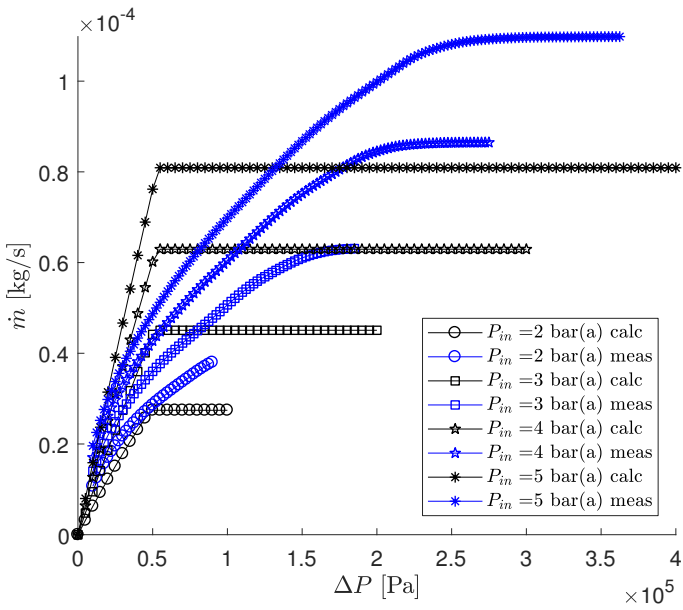
Figure G.5: Model with $F_1 = \frac{12 \cdot 10^{-6}}{h}$ and $F_2 = \left(\frac{12 \cdot 10^{-6}}{h}\right)^{0.4}$ and data for air with $h = 50\ \mu$m.
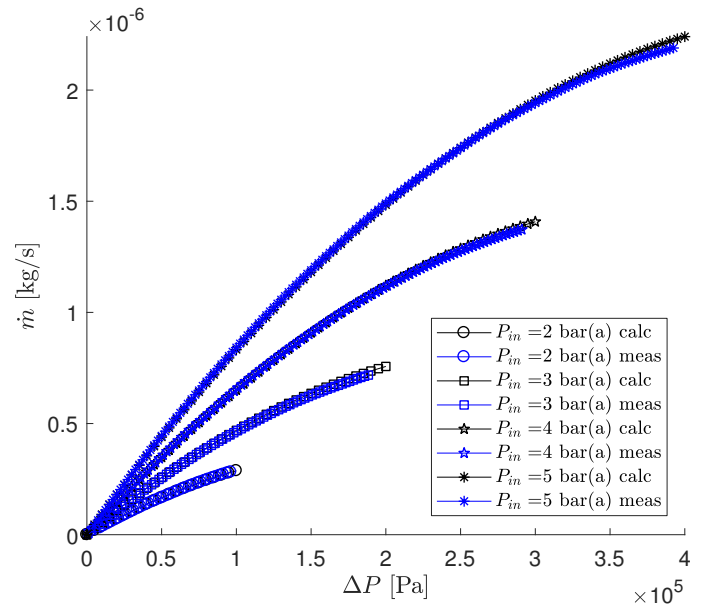
Figure G.6: Model with $F_1 = 0.5 \cdot \frac{12 \cdot 10^{-6}}{h}$ and $F_2 = 0.5 \cdot \left(\frac{12 \cdot 10^{-6}}{h}\right)^{0.4}$ and data for argon with $h = 5\ \mu$m.

Figure G.7: Model with $F_1 = 0.5 \cdot \frac{12 \cdot 10^{-6}}{h}$ and $F_2 = 0.5 \cdot \left(\frac{12 \cdot 10^{-6}}{h}\right)^{0.4}$ and data for argon with $h = 10\ \mu$m.

Figure G.8: Model with $F_1 = 0.5 \cdot \frac{12 \cdot 10^{-6}}{h}$ and $F_2 = 0.5 \cdot \left(\frac{12 \cdot 10^{-6}}{h}\right)^{0.4}$ and data for argon with $h = 20\ \mu$m.

Figure G.9: Model with $F_1 = 0.5 \cdot \frac{12 \cdot 10^{-6}}{h}$ and $F_2 = 0.5 \cdot \left(\frac{12 \cdot 10^{-6}}{h}\right)^{0.4}$ and data for argon with $h = 25\ \mu$m.

Figure G.10: Model with $F_1 = 0.5 \cdot \frac{12 \cdot 10^{-6}}{h}$ and $F_2 = 0.5 \cdot \left(\frac{12 \cdot 10^{-6}}{h}\right)^{0.4}$ and data for argon with $h = 50\ \mu$m.

Figure G.11: Model with $F_1 = 5.35 \cdot \frac{12 \cdot 10^{-6}}{h}$ and $F_2 = 5.35 \cdot \left(\frac{12 \cdot 10^{-6}}{h}\right)^{0.4}$ and data for helium with $h = 5\ \mu$m.

Figure G.12: Model with $F_1 = 5.35 \cdot \frac{12 \cdot 10^{-6}}{h}$ and $F_2 = 5.35 \cdot \left(\frac{12 \cdot 10^{-6}}{h}\right)^{0.4}$ and data for helium with $h = 10\ \mu$m.

Figure G.13: Model with $F_1 = 5.35 \cdot \frac{12 \cdot 10^{-6}}{h}$ and $F_2 = 5.35 \cdot \left(\frac{12 \cdot 10^{-6}}{h} \right)^{0.4}$ and data for helium with $h = 20 \ \mu$m.

Figure G.14: Model with $F_1 = 5.35 \cdot \frac{12 \cdot 10^{-6}}{h}$ and $F_2 = 5.35 \cdot \left(\frac{12 \cdot 10^{-6}}{h} \right)^{0.4}$ and data for helium with $h = 25 \ \mu$m.

Figure G.15: Model with $F_1 = 5.35 \cdot \frac{12 \cdot 10^{-6}}{h}$ and $F_2 = 5.35 \cdot \left(\frac{12 \cdot 10^{-6}}{h} \right)^{0.4}$ and data for helium with $h = 50 \ \mu$m.

Figure G.16: Model with $F_1 = 14 \cdot \frac{12 \cdot 10^{-6}}{h}$ and $F_2 = 14 \cdot \left(\frac{12 \cdot 10^{-6}}{h} \right)^{0.4}$ and data for hydrogen with $h = 5 \ \mu$m.

Figure G.17: Model with $F_1 = 14 \cdot \frac{12 \cdot 10^{-6}}{h}$ and $F_2 = 14 \cdot \left(\frac{12 \cdot 10^{-6}}{h} \right)^{0.4}$ and data for hydrogen with $h = 10 \ \mu$m.

Figure G.18: Model with $F_1 = 14 \cdot \frac{12 \cdot 10^{-6}}{h}$ and $F_2 = 14 \cdot \left(\frac{12 \cdot 10^{-6}}{h} \right)^{0.4}$ and data for hydrogen with $h = 20 \ \mu$m.

Figure G.19: Model with $F_1 = 14 \cdot \frac{12 \cdot 10^{-6}}{h}$ and $F_2 = 14 \cdot \left(\frac{12 \cdot 10^{-6}}{h} \right)^{0.4}$ and data for hydrogen with $h = 25 \ \mu$m.

Figure G.20: Model with $F_1 = 14 \cdot \frac{12 \cdot 10^{-6}}{h}$ and $F_2 = 14 \cdot \left(\frac{12 \cdot 10^{-6}}{h} \right)^{0.4}$ and data for hydrogen with $h = 50 \ \mu$m.

H Improving the model using effective heights

Instead of taking the height constant and using the fudge factor F_1 to correct the model, it is also possible to calculate the mass flow with a different height than the height of the shim. This height can be seen as the effective height of the channel, where the model is then assumed to be exact for this height. Since the height of the channel is not measured, and also the surface roughness of the membrane may influence this height, it is well possible that the real flowthrough height is indeed different from the shim height. Whether the real height is equal to the height that one will obtain from correcting the model (with $F_1 = 1$) towards the data using the height is however very debatable.

It was observed in the model that the mass flow, $\dot{m}$, is approximately proportional to the flowthrough height cubed, h^3. Deviations from this behaviour come from slip along the wall and are expected to be very small. Hence, a good start for approximating the effective height from the earlier determined fudge factor is by using the cubic relation to calculate it:

$$F_1 = \sqrt[3]{\frac{12 \cdot 10^{-6}}{h}} = \left(\frac{h_{eff}}{h}\right)^3 \Rightarrow h_{eff} = h\sqrt[3]{\frac{12 \cdot 10^{-6}}{h}} \tag{H.1}$$

The resulting model does indeed come close to the data, except for the flow in choked conditions. When applying a factor $F_2 = 0.93$ to the sound velocity, the results as shown in figures H.1 to H.4 are obtained. These results are quite comparable to the ones obtained using height-based corrections.
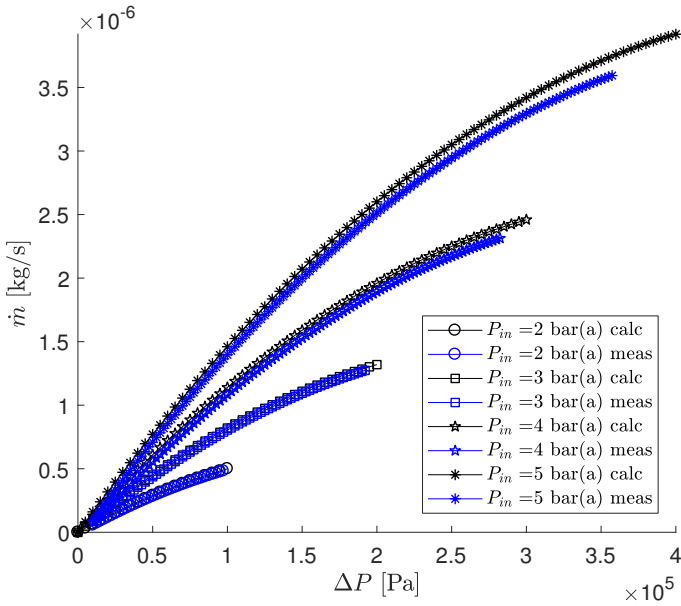
Figure H.1: Results for air; model with $F_1 = 1$, $F_2 = 0.93$ and $h = 6.6943$ μm and data with $h = 5$ μm.
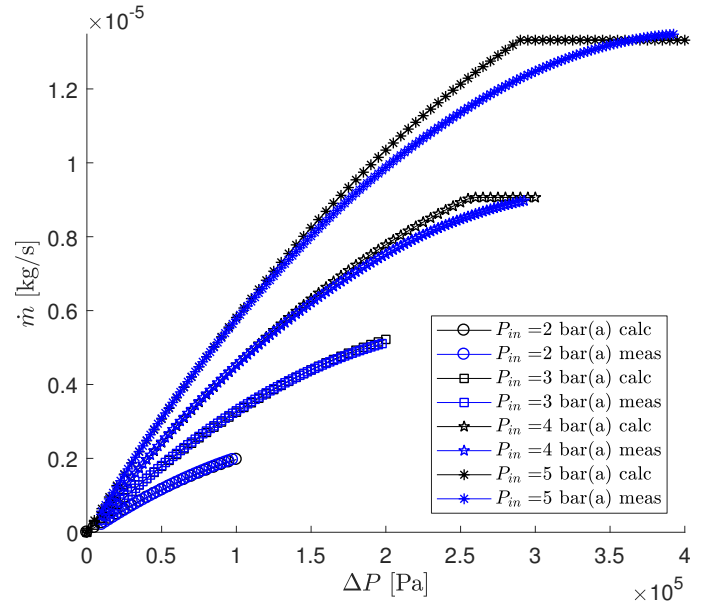
Figure H.2: Results for air; model with $F_1 = 1$, $F_2 = 0.93$ and $h = 10.6266$ μm and data with $h = 10$ μm.
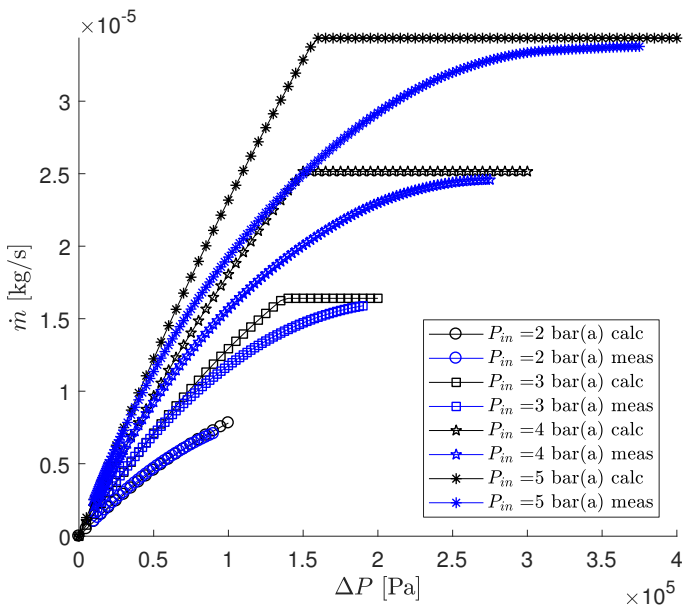
Figure H.3: Results for air; model with $F_1 = 1$, $F_2 = 0.93$ and $h = 16.8687$ μm and data with $h = 20$ μm.
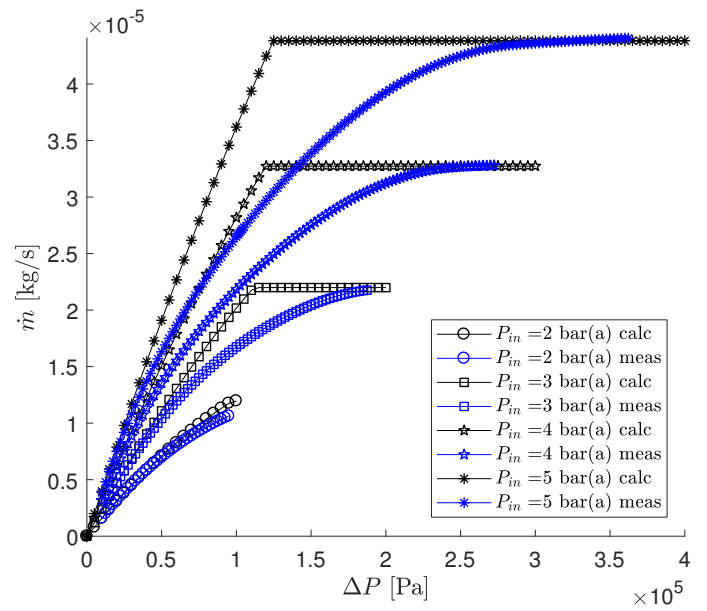
Figure H.4: Results for air; model with $F_1 = 1$, $F_2 = 0.93$ and $h = 19.5743$ μm and data with $h = 25$ μm.

I Estimation of Pressure Loss in Pipes

The pressure loss is not measured only over the channel, but also over the pipes to and from the channel. In this appendix, a rough estimate of the pressure loss in the pipes is made. In figure I.1, the basement of the Piezo valve is shown, with the relevant dimensions for the determination of the pressure loss. The circled red numbers are for later reference. It should be noted that this is only the basement, so the microchannel for which the model was developed is not shown in the figure.
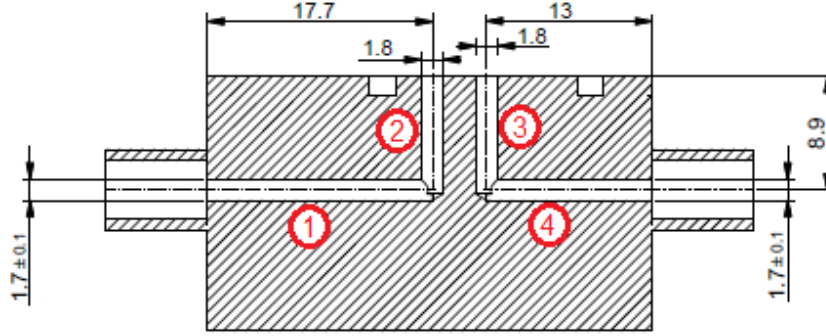
Figure I.1: Section view of the basement of the test Piezo valve, with some relevant dimensions (in mm).

The Darcy-Weisbach equation, given in (I.1), gives the pressure loss in a cylindrical pipe of uniform diameter D and length L, as a function of the mean flow velocity $\bar{u}$ and the fluid density ρ [29]. The coefficient f_D is the Darcy friction factor , which can be determined from the Moody diagram [29]. This diagram is shown in figure I.2. The Darcy-Weisbach equation is valid for incompressible fluids [29], but since the pressure drop is assumed to be relatively small (compared to the inlet pressure), the flow may be assumed incompressible [30].

$$\Delta P = f_D \frac{\rho}{2} \frac{L}{D} \bar{u}^2 \tag{I.1}$$

In order to estimate the pressure drop, additional information is needed. The geometrical properties, L and D, can be read from figure I.1. The velocity will be estimated from the normal volume flow, which is specified at the flow meter. The relation between velocity $\bar{u}$ and normal volume flow Q_n is given in (I.2), where ρ_n is the density at normal conditions ($P = 1$ bar, $T = 273$ K) and ρ is the actual density, which will be determined from the ideal gas law. Since the pressure drop is related to the velocity squared, a lower density will give a more critical situation. Therefore, the density will be determined at a pressure of 1 bar, even though this will be unrealistic for especially the pipes towards the microchannel (1 and 2). For the determination of the friction factor, the Reynolds number and the relative roughness are required. The Reynolds number is defined as $\mathrm{Re} = \frac{\rho \bar{u} D}{\mu}$, and all parameters are known (the viscosity is calculated using Sutherland's law, as explained in appendix B). The relative roughness is given as $\frac{\varepsilon'}{D}$, where ε' is the surface roughness. This is specified as 1.6 μm in the technical drawing of the basement.

$$\bar{u} = \frac{Q_n \rho_n}{A \rho} \tag{I.2}$$

A flow sensor with a normal volume flow capacity of 5 $\mathrm{L_n}$/min air was capable of measuring all flows, except those for hydrogen and helium with a shim height of 50 μm (especially at high inlet pressures and pressure drops). It is therefore chosen to use this for the estimation of the pressure drop. Since the normal volume is specified (and measured) for air, the density at normal conditions is 1.2934 kg/m^3. For air at $P = 1$ bar and $T = 293$ K, this leads to the velocities and Reynolds number as specified in table I.1. Using these numbers, and a relative roughness of about 0.001 (a bit higher than calculated), a conservative approximation (i.e. a bit too high) of the drag coefficient is made from the Moody diagram. These values, and the resulting pressure drops per pipe, are given in table I.1.

The bends in the pipes also cause a pressure drop, which can be calculated using (I.3) [32]. In this equation, R_b is the bend radius (in m), θ is the bend angle (in degree) and k_b is the bend loss coefficient. For this case, the bend radius is approximated to equal $R_b = 0.5D$ and the bend angle is 90°. The bend loss coefficient for a 90 degree bend is 0.85 when the centreline radius of the bend equals $0.5D$ [32], which is the worst case given in
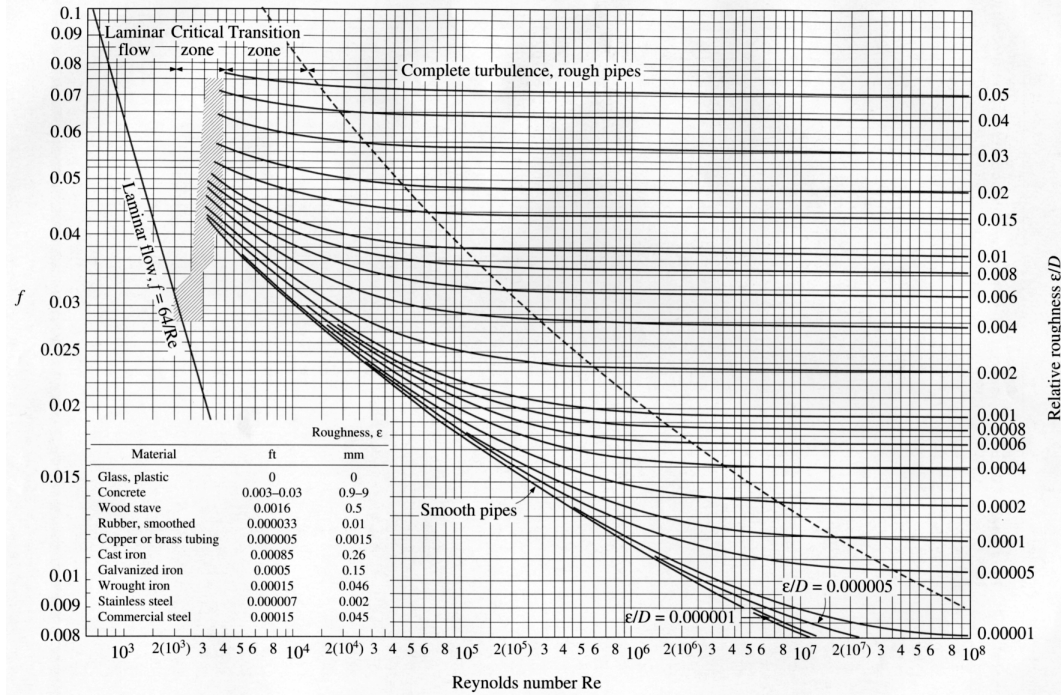
Figure I.2: Moody diagram (image from [31]).

Table I.1: Velocities, Reynolds numbers, estimated Darcy drag coefficients and pressure drops for air in the pipes of the basement block.

Pipe	$\bar{u}$ [m/s]	Re [-]	f_D [-]	ΔP [Pa]
1	39.92	$4.44 \cdot 10^3$	0.025	246.68
2	35.60	$4.19 \cdot 10^3$	0.025	93.20
3	35.60	$4.19 \cdot 10^3$	0.025	93.20
4	39.92	$4.44 \cdot 10^3$	0.025	181.17

the paper. For each bend, the maximum velocity and the minimum pipe diameter is used in the calculation, as this gives the worst case. Hence, both bends 1-2 and 3-4 give the same pressure drop: $\Delta P_{\text{bend}} = 825.33$ Pa.

$$\Delta P_{\text{bend}} = \frac{1}{2} f_D \rho \bar{u}^2 \frac{\pi R_b}{D} \frac{\theta}{180°} + \frac{1}{2} k_b \rho \bar{u}^2 \qquad (\text{I.3})$$

The total pressure drop is now calculated as the sum of the pressure drops in the pipes and the pressure drop in the two bends, which equals $\Delta P_{\text{tot}} = 2265$ Pa. Since the pressure drop that is required to reach a flow that comes close to 5 L_n/min air is in the order of bars ($\cdot 10^5$ Pa), it can be concluded that the pressure drop in the pipes is negligible to the pressure drop in the microchannel.

J Joule-Thomson Effect

In the derivation of the model, it was assumed that the temperature remained constant. However, for isenthalpic and adiabatic expansion, the temperature of real gases changes due to the Joule-Thomson effect. For an ideal gas, the Joule-Thomson coefficient is always zero [33]. In this appendix, the influence of this effect is estimated to verify the assumption of constant temperature. The Joule-Thomson effect is the rate of change of temperature T [K] with respect to pressure P [Pa] in an isenthalpic process, and is expressed as [33]:

$$\mu_{JT} = \left(\frac{\partial T}{\partial P}\right)_H = \frac{V}{C_P}(\alpha T - 1) \tag{J.1}$$

where V is the volume of the gas [m^3], C_P is the heat capacity at constant pressure [J/K] and α is the thermal expansion coefficient [1/K]. Hence the Joule-Thomson coefficient μ_{JT} is expressed in K/Pa. Since the volume of the gas is not constant, the equation is rewritten to the following form:

$$\mu_{JT} = \left(\frac{\partial T}{\partial P}\right)_H = \frac{1}{\rho c_P}(\alpha T - 1) \tag{J.2}$$

where ρ is the fluid's density [kg/m^3] and c_P is the specific heat capacity at constant pressure [J/(kgK)]. This form can be obtained by multiplying (J.1) by $\frac{\frac{1}{m}}{\frac{1}{m}}$. Substituting the ideal gas law yields (J.3), while integrating over the pressure gives the temperature change, as shown in (J.4).

$$\mu_{JT} = \left(\frac{\partial T}{\partial P}\right)_H = \frac{RT}{Pc_P}(\alpha T - 1) \tag{J.3}$$

$$\Delta T = \int_{P_1}^{P_2} \left(\frac{\partial T}{\partial P}\right)_H dP = \frac{RT(\alpha T - 1)}{c_P}\ln\left(\frac{P_2}{P_1}\right) \tag{J.4}$$

For air at $T = 293$ K, $c_P = 1005$ J/(kgK) and $\alpha = 3.43 \cdot 10^{-3}$ K^{-1} [34]. Using the maximum pressure drop ($P_2 = 1 \cdot 10^5$ Pa and $P_1 = 5 \cdot 10^5$ Pa) results in a temperature drop of 0.67 K. This value is relatively small and will not influence the mass flow too much.

For argon, helium and hydrogen, the thermal expansion coefficients were not found. However, the Joule-Thomson coefficients of these gases are shown graphically in [33], see figure J.1. It can be seen that at $T = 293$ K the Joule-Thomson coefficients of hydrogen and helium are negative, such that the gas warms during expansion. The effect is however small (less than 0.5 K) and therefore negligible. Argon will, like air, cool when it is expanded. The temperature drop is about 1.5 K, which is negligible as well. Hence, the Joule-Thomson effect is unlikely to largely influence the flow in the Piezo valve.
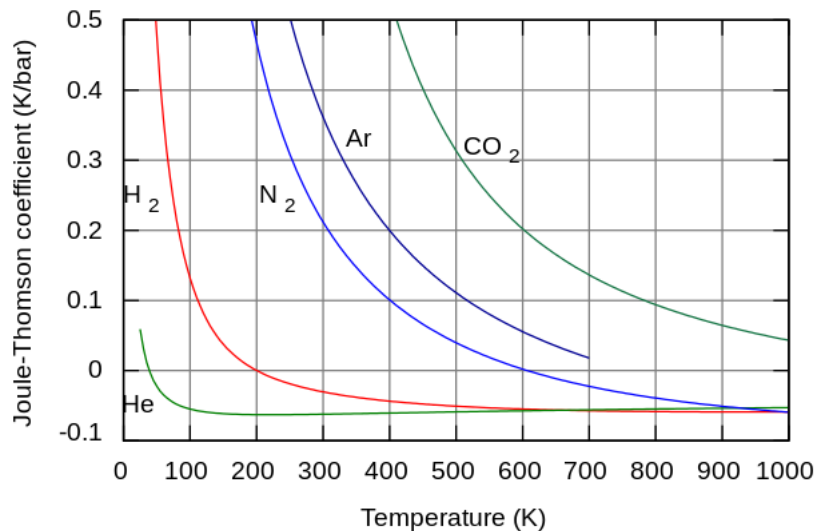
Figure J.1: Joule-Thomson coefficients of several gases as a function of the temperature (source: [33]).

K   Sensitivity of the Model

In this appendix, the sensitivity of the model to the temperature is shown. This is done by showing plots (figure K.1 to K.4) of the model calculated at different temperatures together with the measurement data. It can be seen that the model is not very sensitive to temperature in non-choked conditions, and that the sensitivity is a bit larger in choked flow. Only air and hydrogen are shown here, but the results are similar for the different gases.
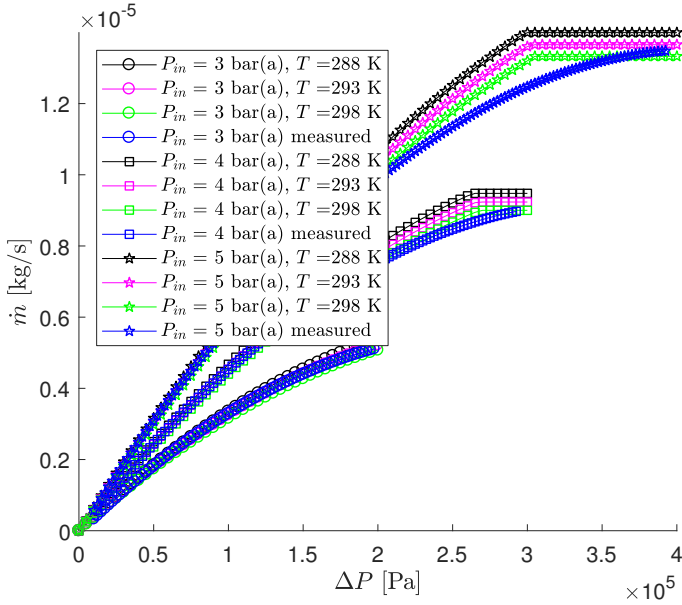
Figure K.1: Influence of temperature for air with a shim height of $h = 10$ μm.
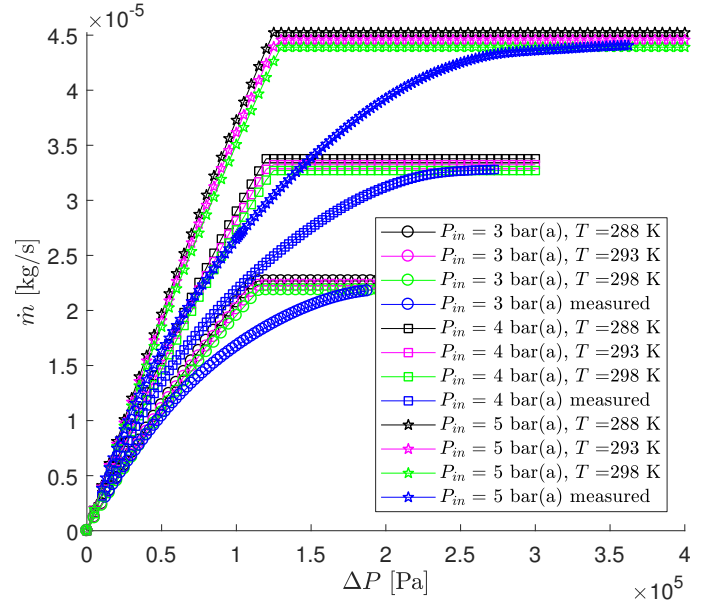
Figure K.2: Influence of temperature for air with a shim height of $h = 25$ μm.
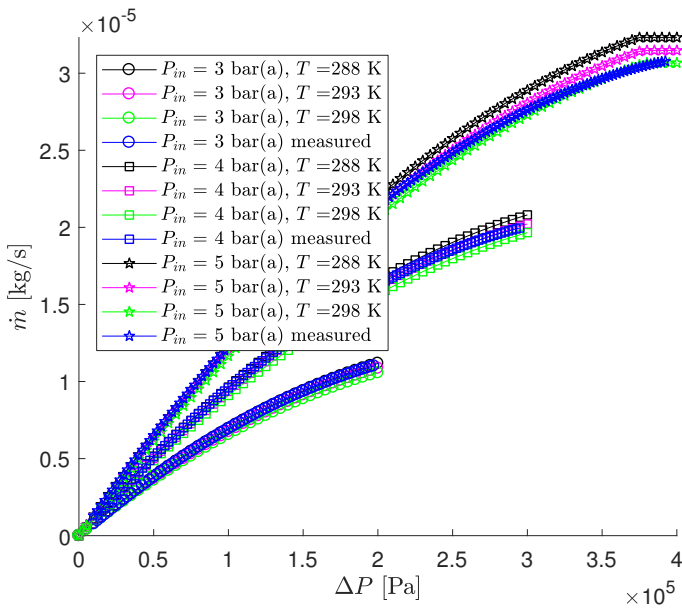
Figure K.3: Influence of temperature for hydrogen with a shim height of $h = 10$ μm.
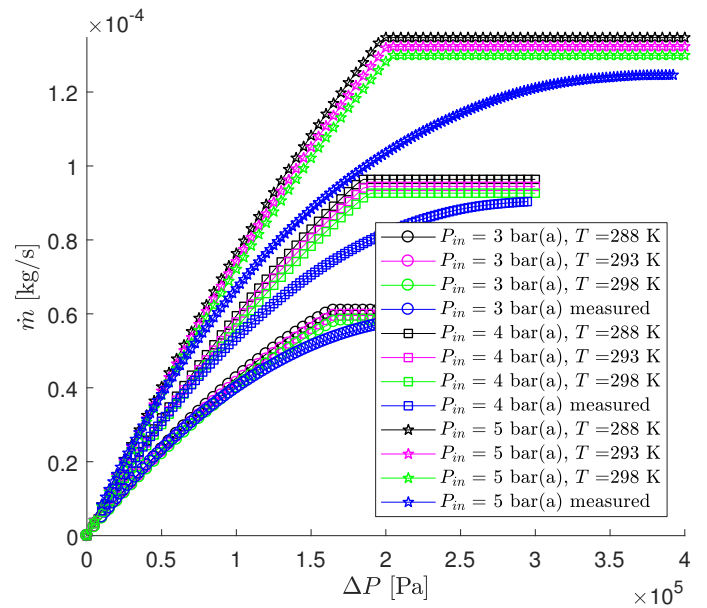
Figure K.4: Influence of temperature for hydrogen with a shim height of $h = 25$ μm.

In the same way, the sensitivity to the orifice diameter is shown. This can be seen in figure K.5 to K.8. It is observed that the influence is relatively small for non-choked conditions, but that it is very large for choked flow. This is caused by the relatively large change in control area that is used to determine whether there is choked flow or not. It is questionable that the influence is indeed this high, indicating the need for more research on choking.
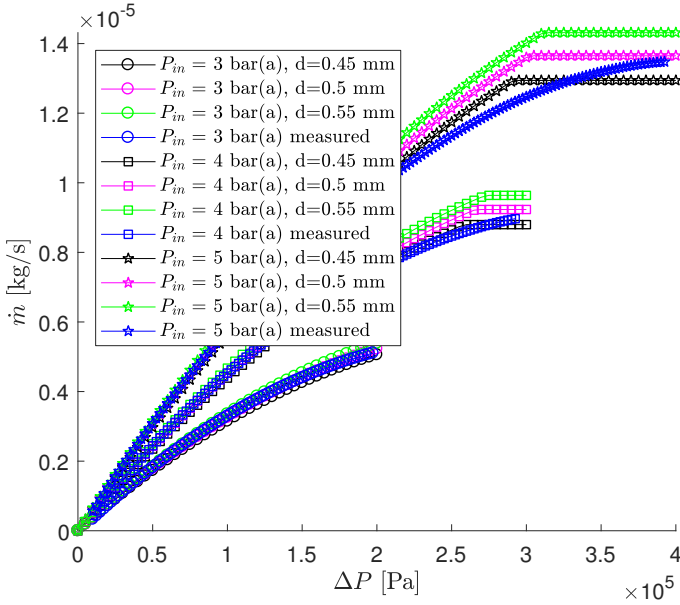
Figure K.5: Influence of orifice diameter for air with a shim height of $h = 10 \ \mu$m.
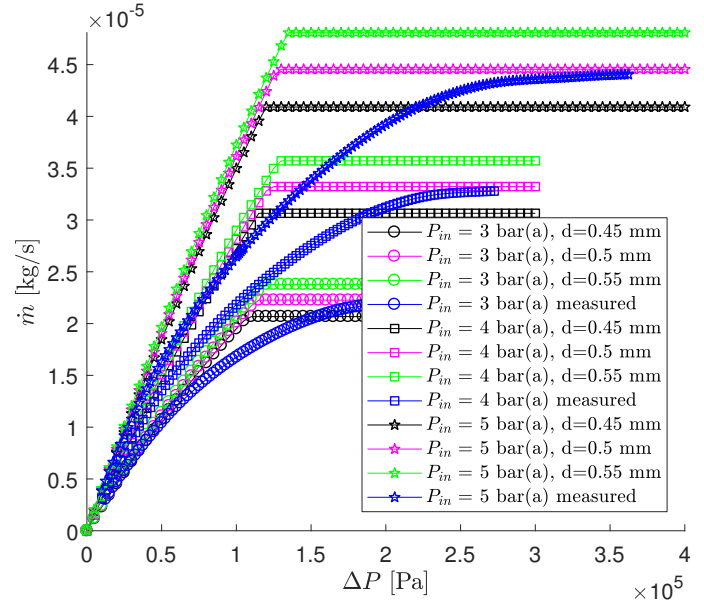
Figure K.6: Influence of orifice diameter for air with a shim height of $h = 25 \ \mu$m.
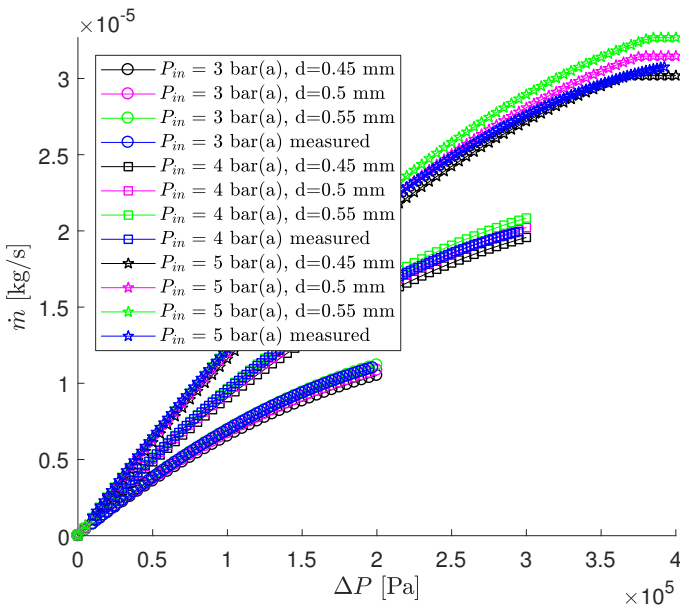
Figure K.7: Influence of orifice diameter for hydrogen with a shim height of $h = 10 \ \mu$m.
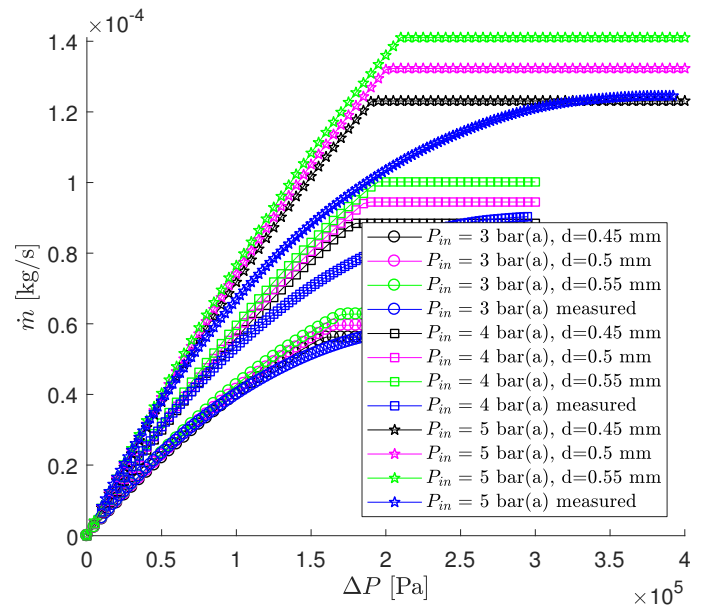
Figure K.8: Influence of orifice diameter for hydrogen with a shim height of $h = 25 \ \mu$m.

L   Flow Direction

In this appendix, all results for the comparison in flow direction are given.
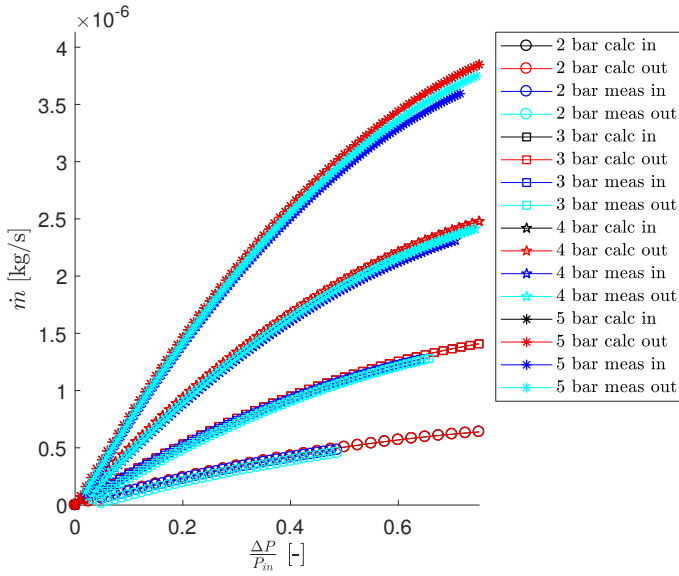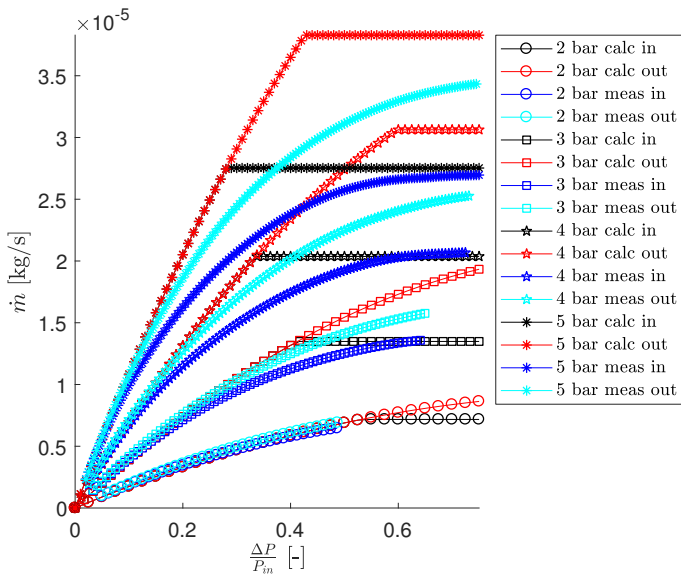

Figure L.1: Calculated and measured mass flows for inward (blue curves) and outward (cyan curves) flow for $h = 5$ μm. Air was used at various constant inlet pressures, and the corrected model was applied.
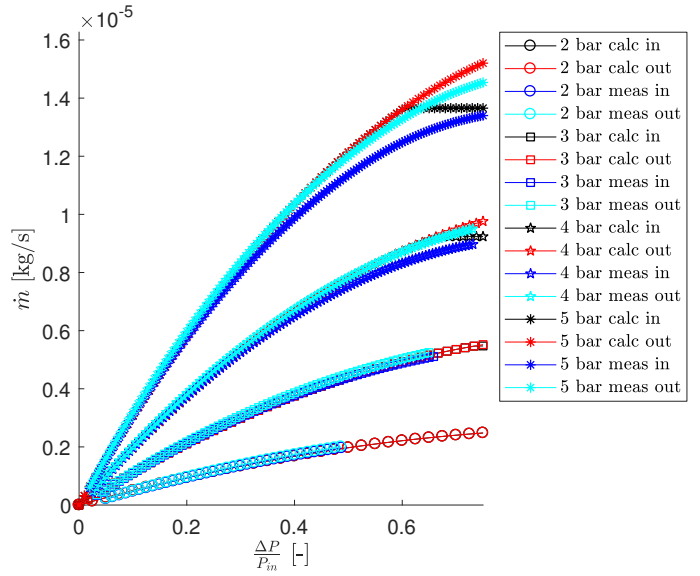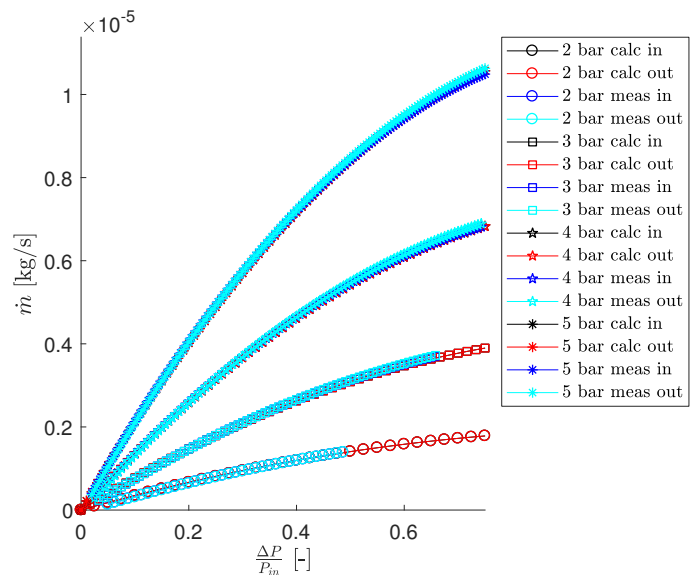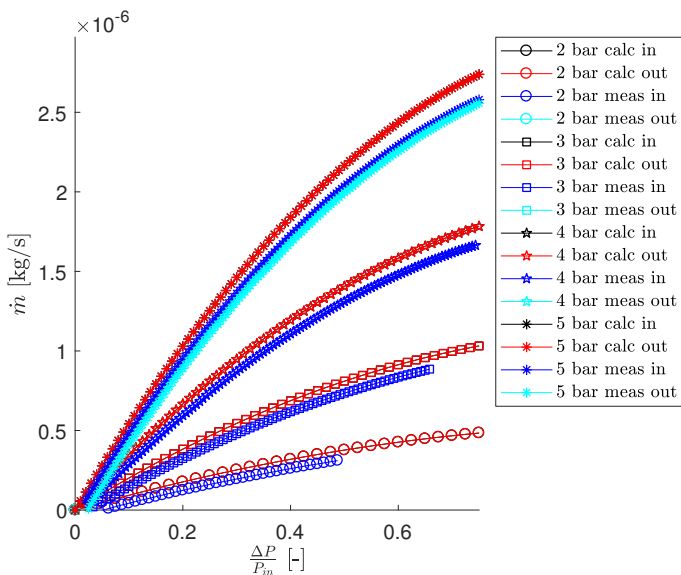

Figure L.2: Calculated and measured mass flows for inward (blue curves) and outward (cyan curves) flow for $h = 10$ μm. Air was used at various constant inlet pressures, and the corrected model was applied.
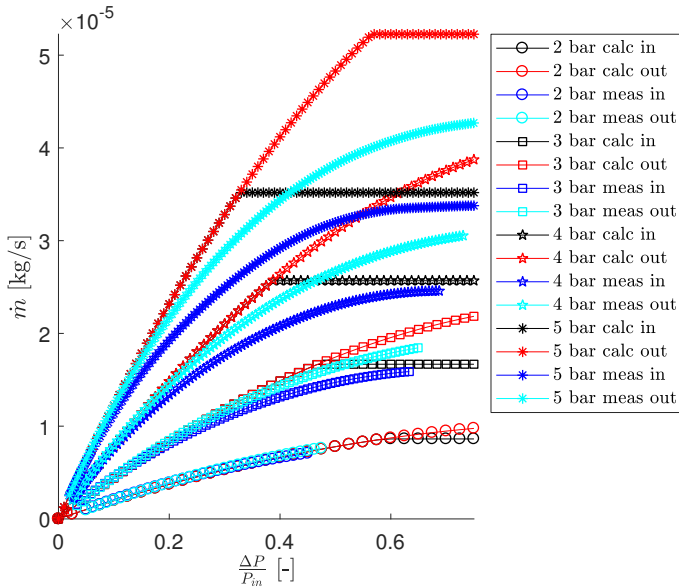
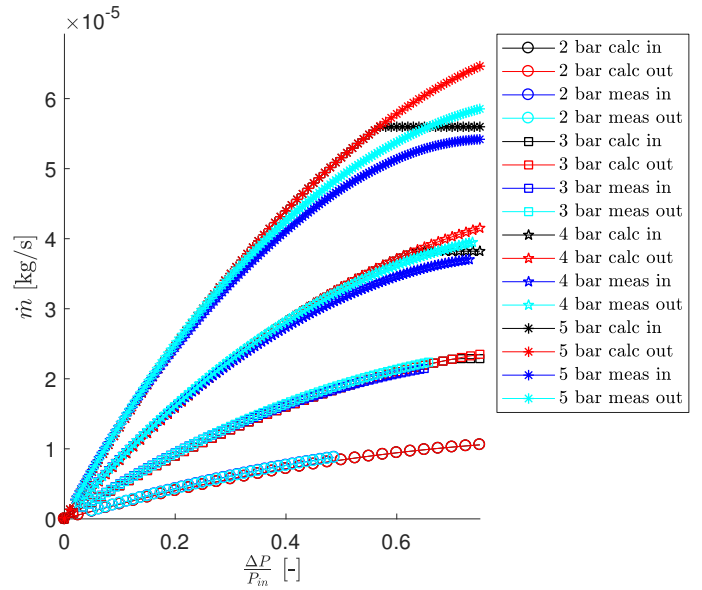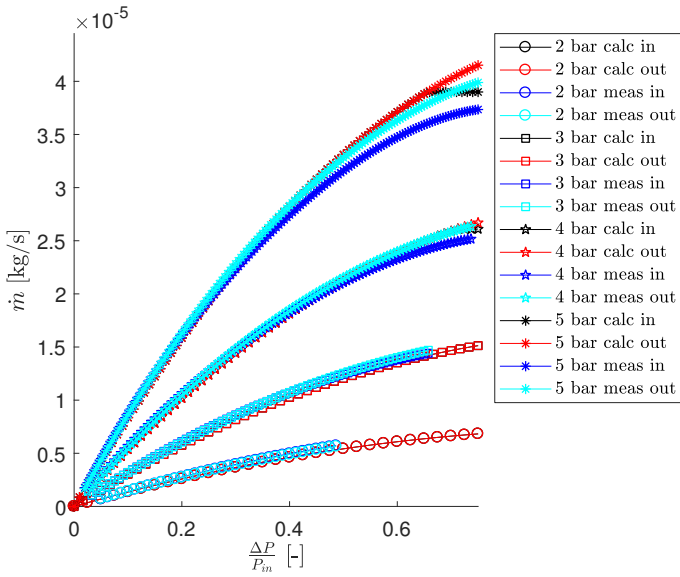Figure L.3: Calculated and measured mass flows for inward (blue curves) and outward (cyan curves) flow for $h = 20$ μm. Air was used at various constant inlet pressures, and the corrected model was applied.
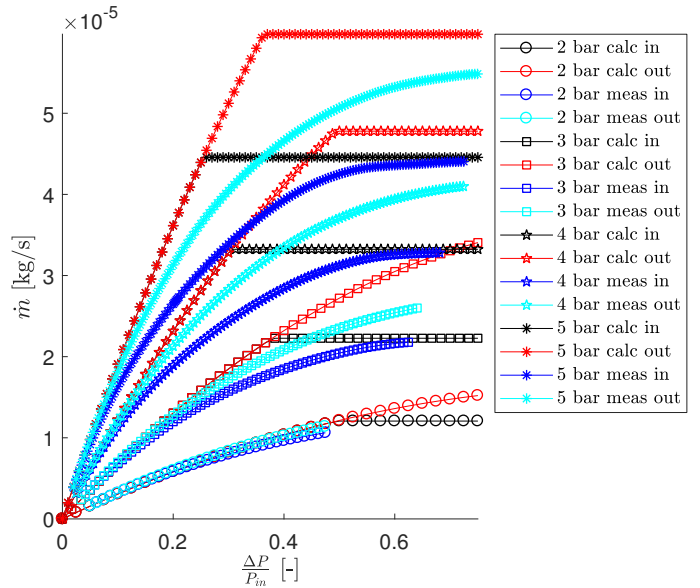
Figure L.4: Calculated and measured mass flows for inward (blue curves) and outward (cyan curves) flow for $h = 25$ μm. Air was used at various constant inlet pressures, and the corrected model was applied.
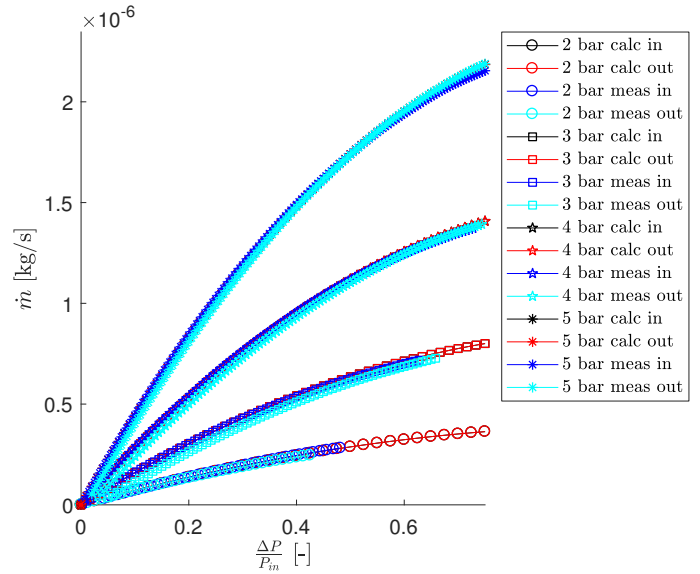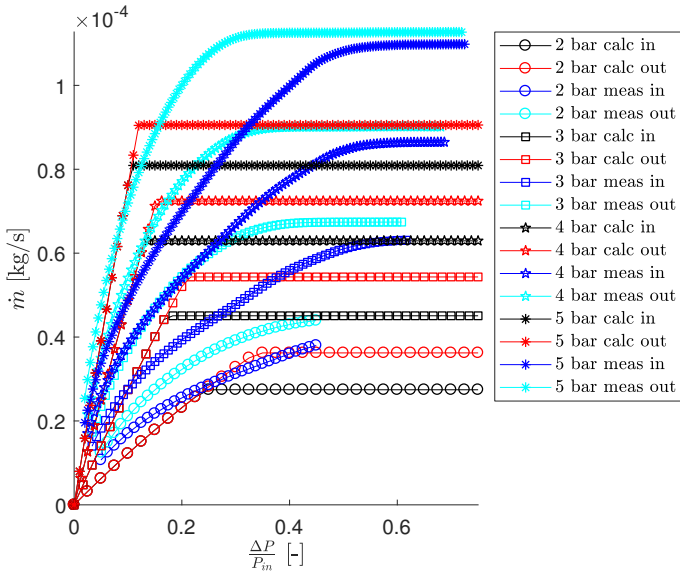
Figure L.5: Calculated and measured mass flows for inward (blue curves) and outward (cyan curves) flow for $h = 50$ μm. Air was used at various constant inlet pressures, and the corrected model was applied.

Figure L.6: Calculated and measured mass flows for inward (blue curves) and outward (cyan curves) flow for $h = 5$ μm. Argon was used at various constant inlet pressures, and the corrected model was applied.
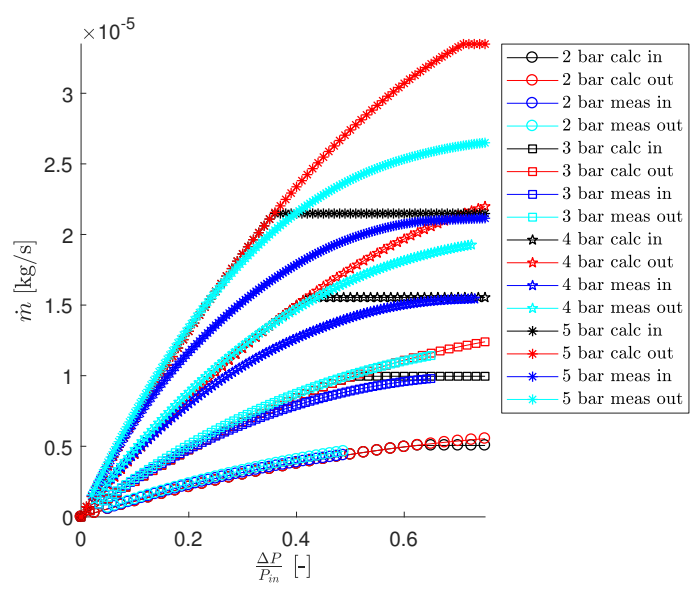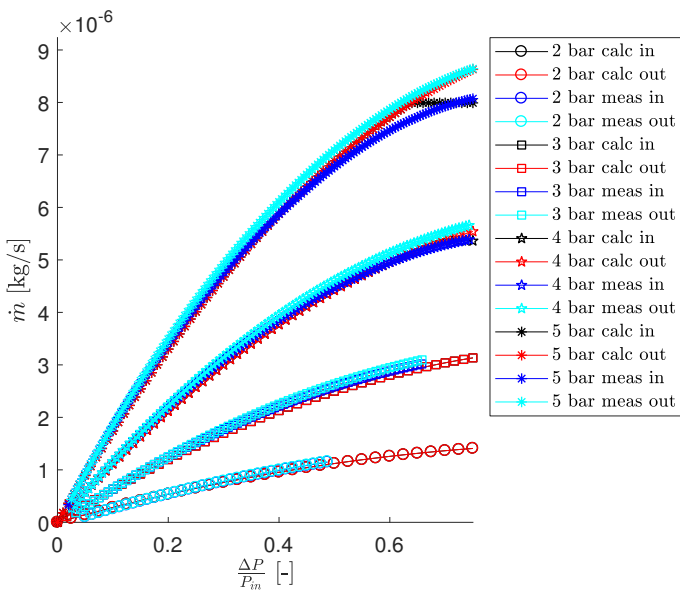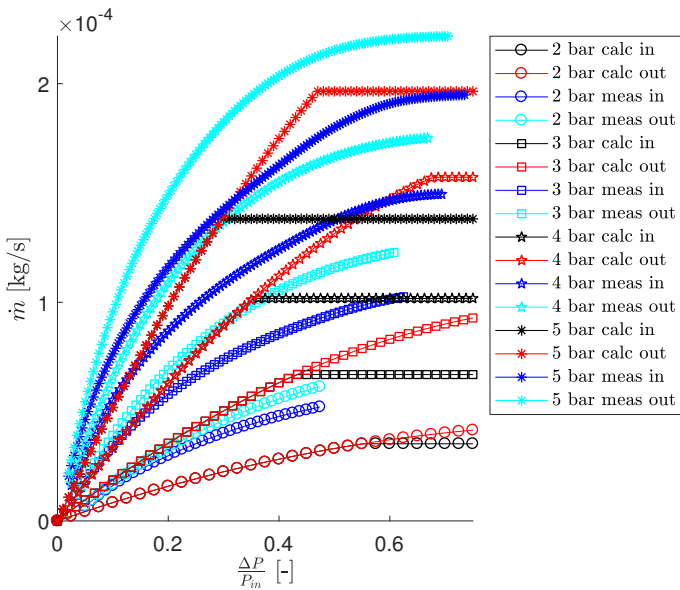

Figure L.7: Calculated and measured mass flows for inward (blue curves) and outward (cyan curves) flow for $h = 10$ μm. Argon was used at various constant inlet pressures, and the corrected model was applied.

Figure L.8: Calculated and measured mass flows for inward (blue curves) and outward (cyan curves) flow for $h = 20$ μm. Argon was used at various constant inlet pressures, and the corrected model was applied.
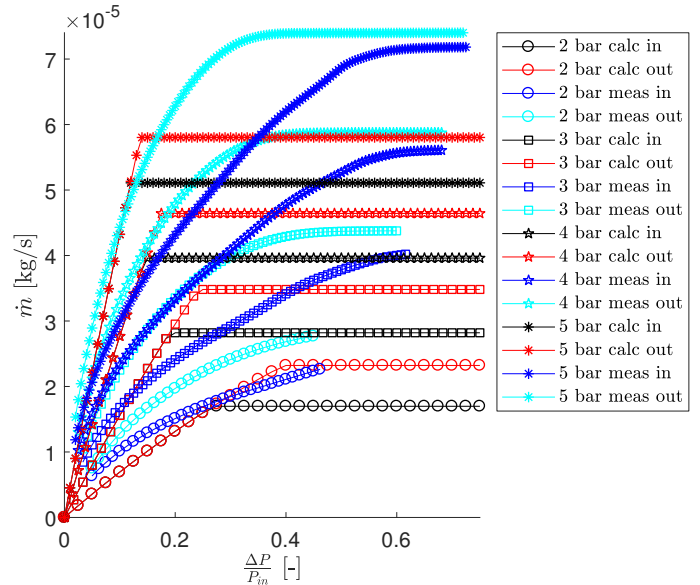
Figure L.9: Calculated and measured mass flows for inward (blue curves) and outward (cyan curves) flow for $h = 25$ μm. Argon was used at various constant inlet pressures, and the corrected model was applied.

Figure L.10: Calculated and measured mass flows for inward (blue curves) and outward (cyan curves) flow for $h = 50$ μm. Argon was used at various constant inlet pressures, and the corrected model was applied.

Figure L.11: Calculated and measured mass flows for inward (blue curves) and outward (cyan curves) flow for $h = 5$ μm. Helium was used at various constant inlet pressures, and the corrected model was applied.

Figure L.12: Calculated and measured mass flows for inward (blue curves) and outward (cyan curves) flow for $h = 10$ μm. Helium was used at various constant inlet pressures, and the corrected model was applied.

Figure L.13: Calculated and measured mass flows for inward (blue curves) and outward (cyan curves) flow for $h = 20$ μm. Helium was used at various constant inlet pressures, and the corrected model was applied.

Figure L.14: Calculated and measured mass flows for inward (blue curves) and outward (cyan curves) flow for $h = 25$ μm. Helium was used at various constant inlet pressures, and the corrected model was applied.

Figure L.15: Calculated and measured mass flows for inward (blue curves) and outward (cyan curves) flow for $h = 50$ μm. Helium was used at various constant inlet pressures, and the corrected model was applied.

M   Safety Margin

In this appendix, the results of the model with safety margin included are compared to the measurements data. It is observed that, as desired, the calculated flow is always below the measured flow, such that the desired flow can always be reached.
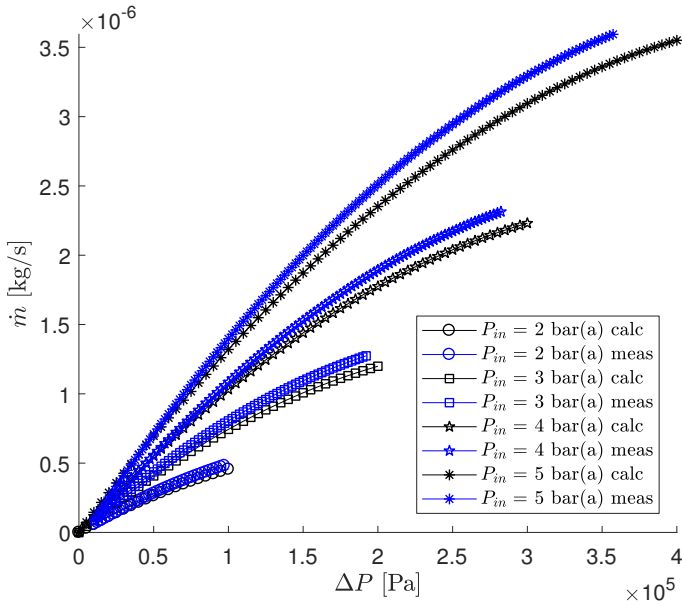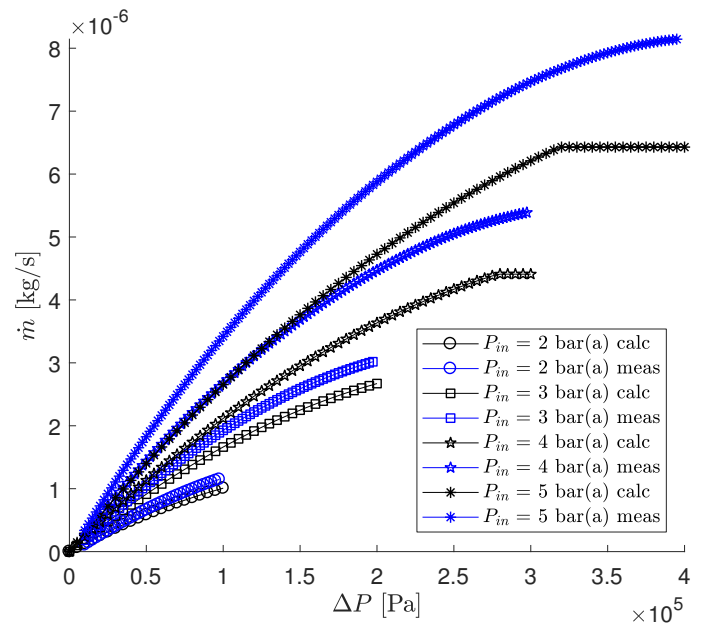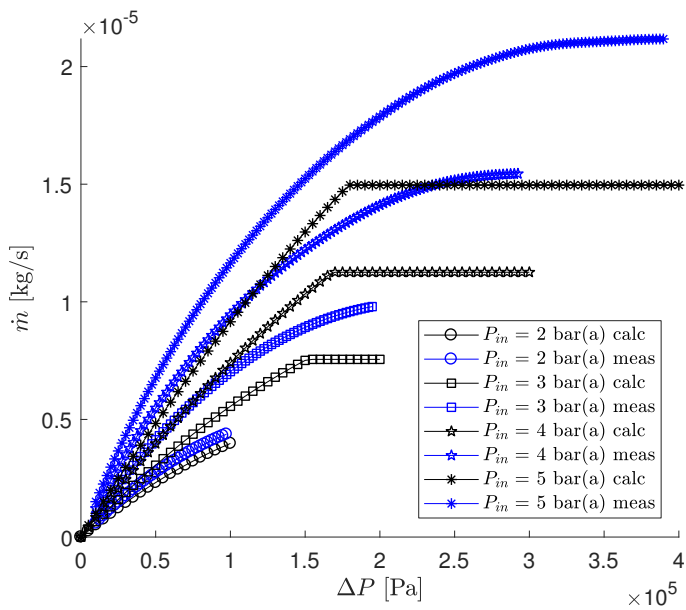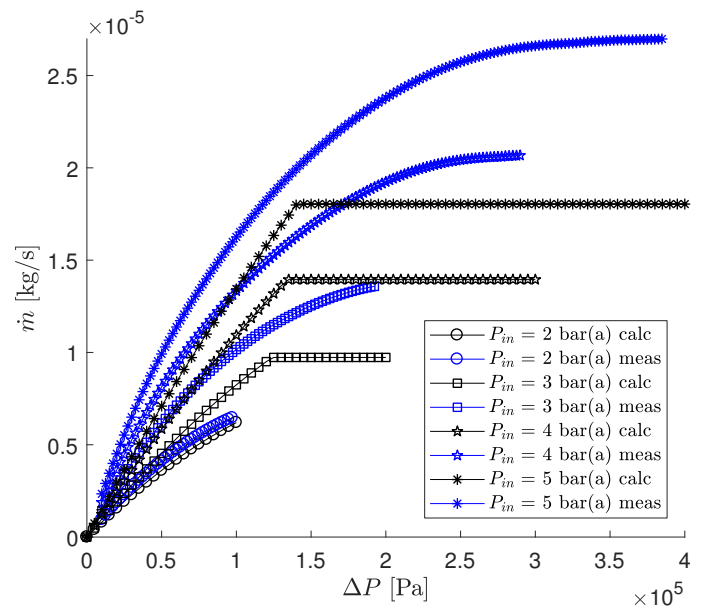

Figure M.1: Model with safety margin and data for air with $h = 5$ μm.
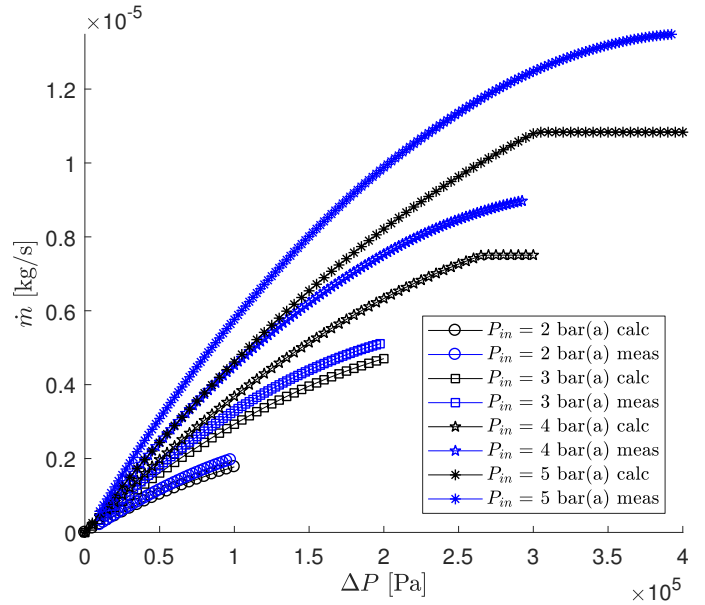
Figure M.2: Model with safety margin and data for air with $h = 10$ μm.
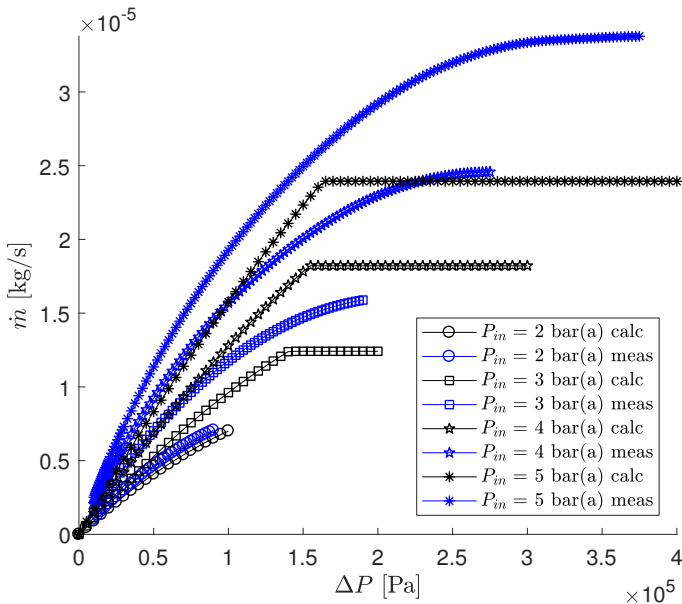
Figure M.3: Model with safety margin and data for air with $h = 20$ μm.
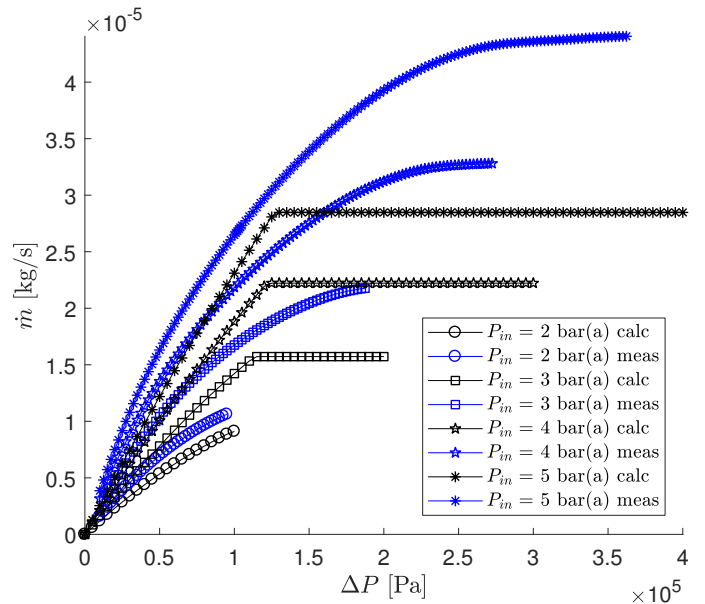
Figure M.4: Model with safety margin and data for air with $h = 25$ μm.
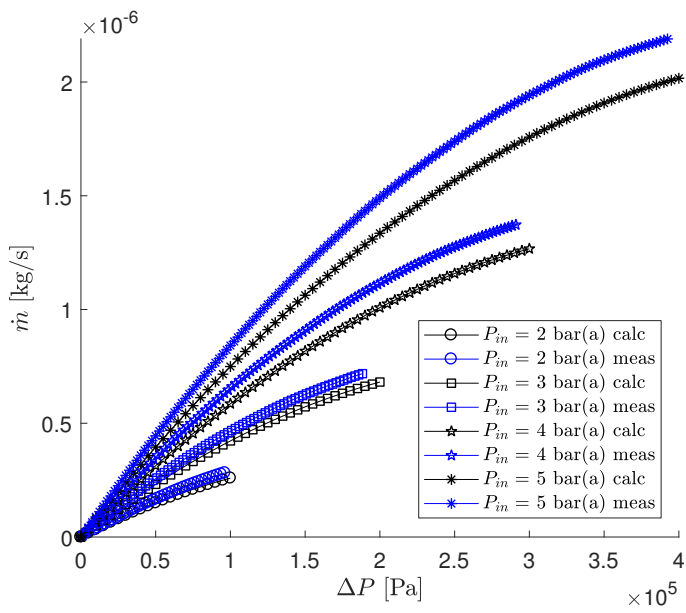
Figure M.5: Model with safety margin and data for argon with $h = 5$ μm.

Figure M.6: Model with safety margin and data for argon with $h = 10$ μm.

Figure M.7: Model with safety margin and data for argon with $h = 20$ μm.

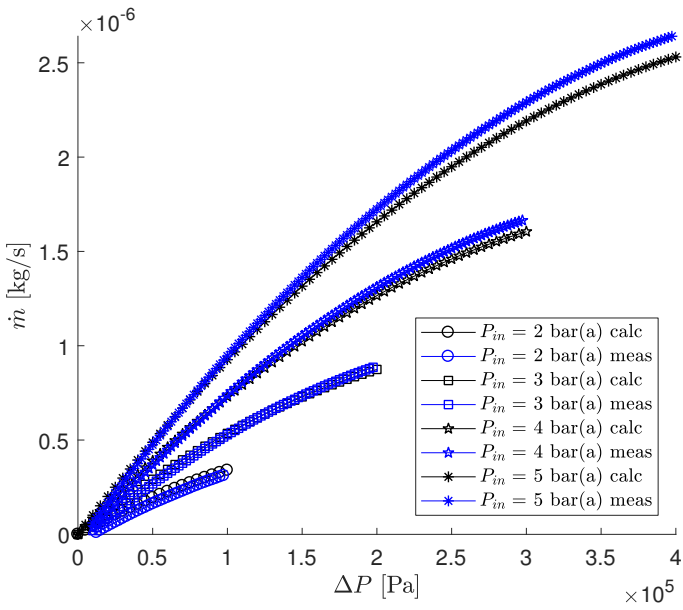Figure M.8: Model with safety margin and data for argon with $h = 25$ μm.

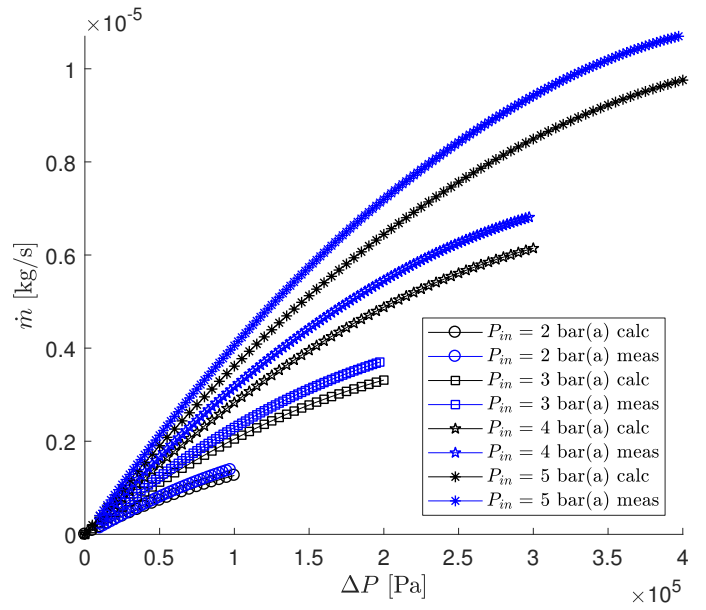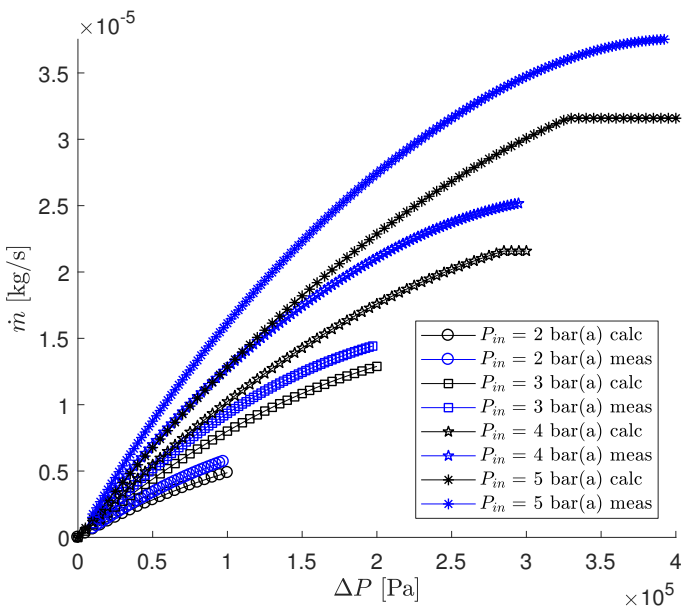Figure M.9: Model with safety margin and data for helium with $h = 5$ μm.

Figure M.10: Model with safety margin and data for helium with $h = 10$ μm.

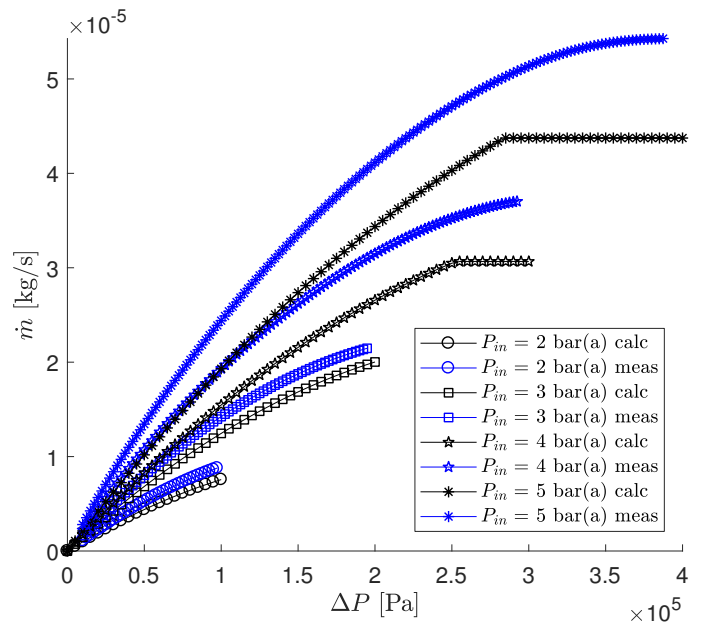Figure M.11: Model with safety margin and data for helium with $h = 20$ μm.

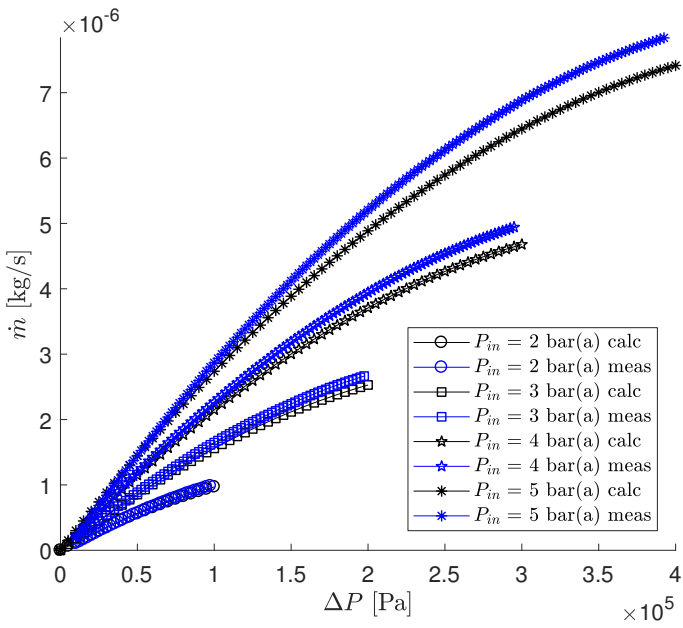Figure M.12: Model with safety margin and data for helium with $h = 25$ μm.

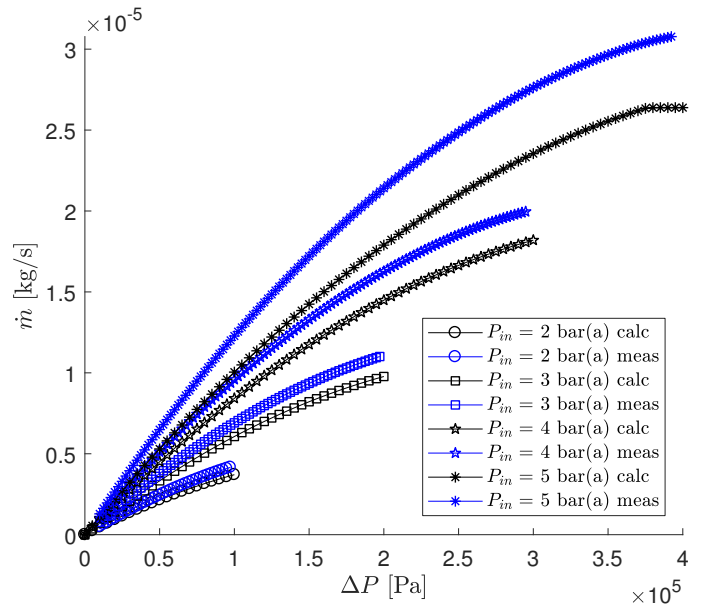Figure M.13: Model with safety margin and data for hydrogen with $h = 5$ μm.

Figure M.14: Model with safety margin and data for hydrogen with $h = 10$ μm.
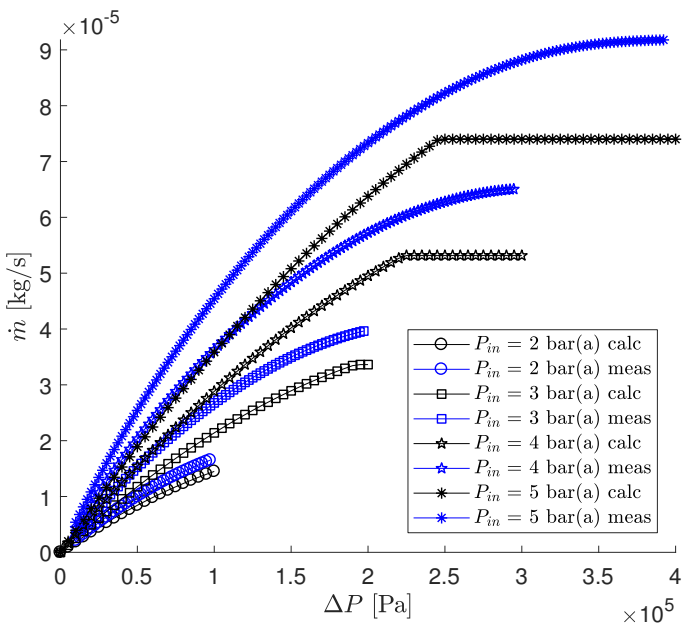

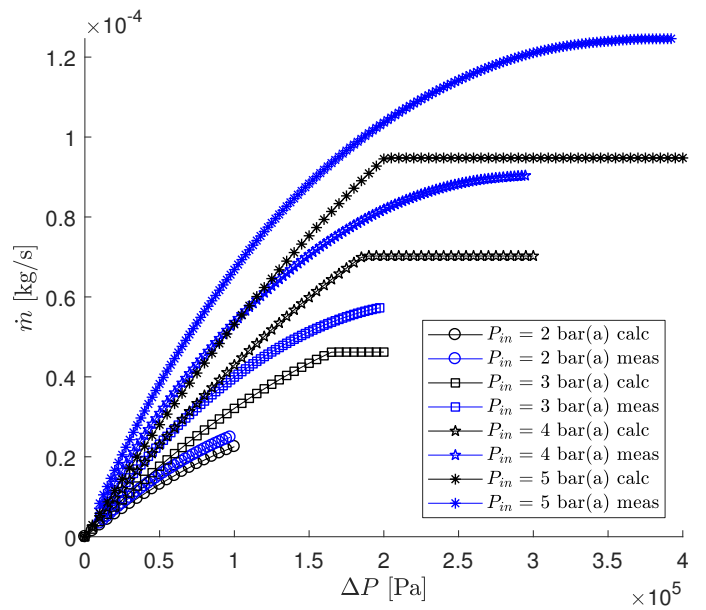Figure M.15: Model with safety margin and data for hydrogen with $h = 20$ μm.

Figure M.16: Model with safety margin and data for hydrogen with $h = 25$ μm.

N   About Bronkhorst High-Tech and Reflection

This appendix offers a short description of Bronkhorst High-Tech B.V., and a reflection on my own functioning within the organisation.

Bronkhorst High-Tech B.V. develops and assembles mass flow meters and controllers for low flows. The company was established in 1981. In 1987, they won the Koning Willem I Award for a young successful enterprise. The quality of the products is very important for Bronkhorst, and they were certified to several ISO norms. Over time, Bronkhorst has grown to a world-wide organisation with daughter companies in for example the USA, Japan and China. In addition, an extensive (complementary) network of distributors and service station has been built up. The headquarters in Ruurlo has about 425 employees, of which 70 are working on product improvement, expansion of the portfolio and basic R&D.

During my internship at BHT (at the headquarters in Ruurlo), I worked on the R&D department in the Mechanical Engineering group. Although working on my own assignment, I was treated as a full member of the group, meaning I belonged to for example the R&D meetings, monthly treats (for the entire company) and to a dinner with the group. As a result of being a full member of the group, I functioned as an "expert" on my assignment and was (relatively) free to do the study in the way that I found the correct one. During regular meetings with my supervisors we discussed the results up to then, and decided on the next steps. I think I functioned well in this organisation structure, as I was guided sufficiently, but I also got my responsibilities (as I will also get when I go to work). Regarding the assignment, I have to conclude that I did not achieve the results I wanted. I think that my results offer a good improvement, and can be used on relatively short terms, but they can, and need to, be improved in further studies.